POSTDOCTORAL REPORT

TITLE :

BAYESIAN INFERENCE AND/OR OPTIMIZATION STRATEGIES FOR SOME DETECTION, TRACKING AND DECONVOLUTION PROBLEMS IN MEDICAL IMAGES

AUTHOR :

MAX MIGNOTTE

Postoctoral research work achieved at DIRO of Montreal University (Canada),
financed by a INRIA postdoctoral grant, France,
and supervised by Professor Jean Meunier.

Final Report
Sept. 1999

Postoctoral research work achieved at DIRO (Département d'Informatique et de Recherche Opérationnelle) of Montreal University[1] *(Canada, Quebec) (at Vision and geometrical modeling laboratory), financed by a* **INRIA** *(Institut National de Recherche en Informatique et Automatique) postdoctoral grant, France and supervised by Professor Jean Meunier.*

[1]DIRO, Université de Montréal P.O. 6128, H3C 3J7 Succ. Centre-ville, Canada (Quebec).

ACKNOWLEDGMENTS

I thank **INRIA** (Institut National de la Recherche en Informatique et Automatique, France) for financial support of this work (postdoctoral grant). I am also grateful to Jean-Paul Soucy and Christian Janicki (CHUM, University of Montréal) for having provided the SPECT and echographic images. I would like also to acknowledge my supervisor Professor Jean Meunier for his help and his numerous suggestions.

TABLE OF CONTENTS

List of Tables **3**

List of Figures **5**

Chapter 1 : Introduction **9**

Chapter 2 : Shape-based Segmentation and tracking of anatomical structures using Deformable templates and a noise model estimation in an echographic sequence **11**

2.1 Abstract . . . 11
2.2 Introduction . . . 11
2.3 Deformable template representation . . . 13
2.4 Segmentation model . . . 16
2.5 Distribution mixture parameter estimation . . . 21
2.6 Optimization Problem . . . 24
2.7 Experimental results . . . 26
2.8 Conclusion . . . 29

Chapter 3 : An unsupervised multiscale approach for the dynamic contour-based boundary detection issue in ultrasound imagery **37**

3.1 Abstract . . . 37
3.2 Introduction . . . 37
3.3 The active contour model . . . 38
3.4 Multiscale minimization strategy . . . 41
3.5 Experimental results . . . 43
3.6 Conclusion . . . 44

Chapter 4 : A comparison of supervised and blind deconvolution techniques applied in SPECT imagery **47**

4.1 Abstract . . . 47
4.2 Introduction . . . 47
4.3 Deconvolution . . . 49
4.4 Distribution mixture parameter estimation . . . 54
4.5 Experimental results . . . 58
4.6 Conclusion . . . 61

Chapter 5 : Three-dimensional blind deconvolution of SPECT images **69**

5.1 Abstract . . . 69
5.2 Introduction . . . 69
5.3 3D Deconvolution Method . . . 70
5.4 Support determination method . . . 72
5.5 Experimental results . . . 76
5.6 Conclusion . . . 77

References **83**

Publications related to this work **87**

About the Author **89**

LIST OF TABLES

2.1 Estimated parameters for the picture reported in Figure 2.4.a. π stands for the proportion of the two classes within the ultrasound image. *min* and α are the Rayleigh law parameters. 24

2.2 Estimated parameters for the picture reported in Figure 2.12. π stands for the proportion of the two classes within the synthetic image. *min* and α are the Rayleigh law parameters. From top to bottom (**a**) Initialization of the ICE procedure. (**b**) Estimated parameters by the ICE procedure. (**c**) Real parameters. 29

3.1 Estimated parameters for the ultrasound image reported in Fig.3.5 π stands for the proportion of the two classes within the image. *min* and α are the shifted Rayleigh law parameters. 43

4.1 Estimated parameters for the picture reported in Figure 4.4b. π stands for the proportion of the three classes within the SPECT image. α are the exponential law parameter. μ and σ^2 are the Gaussian law parameters. 56

4.2 Iteration number for each supervised deconvolution method as chosen by the proposed stopping rule. Respectively ; the Van-Cittert (VC), the Landweber (LW), the Richardson-Lucy (RL), the Super Resolution (SR) and the Molina's (MO) algorithms. 62

4.3 Computational cost for each deconvolution method. Respectively ; the Van-Cittert (VC), the Landweber (LW), the Richardson-Lucy (RL), the Super Resolution (SR), the Molina (MO), the IBD, the Biggs-Lucy (BL), the NAS-RIF and finally, the You-Kaveh's (YK) algorithm. Results are obtained on a standard SunSparc 2 workstation and are expressed in seconds. 62

4.4 Contrast and Image mottle enhancement from the original input image and for each deconvolution method (enhancement expressed in percentage). Respectively ; the Van-Cittert (VC), the Landweber (LW), the Richardson-Lucy (RL), the Super Resolution (SR), the Molina (MO), the IBD, the Biggs-Lucy (BL), the NAS-RIF and finally, the You-Kaveh's (YK) algorithm. 62

LIST OF FIGURES

2.1 Local non-affine deformations of the initial prototype template. (**a**) Initial template (the grid is not part of the model itself). (**b**) Deformed template with local random perturbations for each control point. 14

2.2 Global non-affine deformations on the locally deformed template reported in Figure 2.1.b. This deformation uses the displacement functions defined in Equation (2.3) along with progressively higher order frequency components and higher values of deformation coefficients ξ_{mn}. (**a**) $M=N=1$ and $\xi^x_{11}=\xi^y_{11}=1$. (**b**) $M=N=1$ and $\xi^x_{mn}=\xi^y_{mn}=2 \ \ \forall m,n \in \{0,1\}^2$. (**c**) $M=N=2$ and $\xi^x_{mn}=\xi^y_{mn}=1 \ \ \forall m,n \in \{0,1,2\}^2$. (**d**) $M=N=2$ and $\xi^x_{mn}=\xi^y_{mn}=2 \ \ \forall m,n \in \{0,1,2\}^2$. 15

2.3 Considered affine transformations applied on the locally and globally deformed prototype template reported in Figure 2.2.d. (**a**) Scale transformation. (**b**) Stretch transformation. (**c**) Rotation transformation. 16

2.4 Spatial and temporal edge map derived from two successive frames of an echographic sequence. (**a**) Echogram (frame 1). (**b**) Echogram (frame 2). (**c**) Spatial gradient map. (**d**) Temporal gradient map. 17

2.5 The two different regions delimited by the template at a specific location and transformation. $\gamma^\bullet_\theta$ is the set of pixels inside the region delimited by the deformed prototype template γ_θ. γ°_θ is the set of pixels located on the contour of γ_θ with a slightly superior scale. 20

2.6 2^{nd} order neighborhood and associated two-site cliques. 23

2.7 Image histogram of the picture reported in Figure 2.4.a (solid curve) and estimated probability density mixture obtained with the ICE procedure (dotted and dashed curves). 24

2.8 An example of crossover with the partial exchange of information. 26

2.9 Smoothed probability map for the ultrasound image reported in Figure 2.4.a (**a**) Probability map associated to the *blood* class. (**b**) Probability map associated to the *muscle* class. 27

2.10 Successive generations of the genetic search on an ultrasound image showing the endocardium (first frame of the sequence). Best 5 % deformed templates before the gradient ascent procedure (on the left) and the best resulting template (on the right). Hybrid GA optimization after : (**a**) 2 generations ($\mathcal{F}(\epsilon(\theta,y))=0.091$). (**b**) 3 generations ($\mathcal{F}(\epsilon(\theta,y))=0.119$). (**c**) 4 generations ($\mathcal{F}(\epsilon(\theta,y))=0.173$). (**d**) 8 generations ($\mathcal{F}(\epsilon(\theta,y))=0.186$). An accurate and reliable detection of the endocardial border is obtained. 30

2.11 Successive generations of the genetic search on an ultrasound image showing the endocardium (frame 38). Best 5 % deformed templates before the gradient ascent procedure (on the left) and the best resulting template (on the right). Hybrid GA optimization after : (**a**) 0 generation (initial population of the GA) ($\mathcal{F}(\epsilon(\theta,y))=0.100$). (**b**) 2 generations ($\mathcal{F}(\epsilon(\theta,y))=0.123$). (**c**) 4 generations ($\mathcal{F}(\epsilon(\theta,y))=0.155$). (**d**) 8 generations ($\mathcal{F}(\epsilon(\theta,y))=0.157$). An accurate and reliable detection of the endocardial border is obtained. 31

2.12 Successive generations of the genetic search on an synthetic image with synthetic Rayleigh noise. Best 5 % deformed templates before the gradient ascent procedure (on the left) and the best resulting template (on the right). Hybrid GA optimization after : (**a**) 2 generations ($\mathcal{F}(\epsilon(\theta,y)) = 0.149$). (**b**) 4 generations ($\mathcal{F}(\epsilon(\theta,y)) = 0.166$). (**c**) 6 generations ($\mathcal{F}(\epsilon(\theta,y)) = 0.167$). (**d**) 10 generations ($\mathcal{F}(\epsilon(\theta,y)) = 0.174$). An accurate and reliable detection and segmentation is obtained and can be compared to the ground truth segmentation reported in Figure 2.14. 32
2.13 Successive generations of the genetic search on an synthetic image with synthetic Rayleigh noise. Best 5 % deformed templates before the gradient ascent (on the left) and the best resulting template (on the right). hybrid GA optimization after : (**a**) 2 generation ($\mathcal{F}(\epsilon(\theta,y)) = 0.116$). (**b**) 4 generations ($\mathcal{F}(\epsilon(\theta,y)) = 0.118$). (**c**) 10 generations ($\mathcal{F}(\epsilon(\theta,y)) = 0.119$). (**d**) 24 generations ($\mathcal{F}(\epsilon(\theta,y)) = 0.120$). An accurate and reliable detection and segmentation is obtained and can be compared to the ground truth segmentation reported in Figure 2.14. 33
2.14 Ground truth segmentation (on the left) and segmentation results obtained with our segmentation method (on the right). (**a**) Synthetic image presented in Figure 2.12. (**b**) Synthetic image presented in Figure 2.13. 34
2.15 Unsupervised Markovian segmentation of an ultrasound image using the single scale determinstc relaxation technique called ICM and based on the parameters estimated by the ICE procedure. (**a**) Real ultrasound image. (**b**) Two-class Markovian segmentation. The resulting semented map exhibits unproper *blood* or *muscle* areas due to the strong speckle noise present on this image. 34
2.16 Tracking of the endocardial contour in a medical echographic sequence at different time frames during the cardiac cycle. From top left to bottom right : frame 1, 4, 6, 9, 12, 13, 18, 20, 27, 34, 35, 40, 41, 44, 46, 48. 35
2.17 Detection/Segmentation obtained with our procedure on real ultrasound images. The best resulting template is drawn on a rectangular grid to visualize the global non-affine transformation estimated by the GA. (**a**) frame 33. (**b**) frame 45. 36
2.18 Set of deformed templates and mean shape. (**a**) Best resulting templates obtained on the 20 first frames of the image sequence reported in Figure 2.16. (**b**) Mean shape computed from this set of deformed templates. 36

3.1 Portion of a contour model showing five connected nodes and the set of points v_i^{in} and v_i^{out} used in the external energy term. $N_{\text{in}} = N_{\text{out}} = 2$ in this example. 40
3.2 Hierarchical structure ($L=1$ in this example) involved in the multiscale minimization strategy and block of pixels b_s^l associated to the node $v_{b_s^l}$. 41
3.3 "Coarse-to-fine" minimization strategy. 42
3.4 Image histogram of the ultrasound image reported in Fig. 3.5 (solid curve) and estimated PDF mixture obtained with the ICE procedure (dashed and dotted curves). . 44
3.5 (**a**) ML blocky segmentation at different resolution levels and estimated snakes at different resolution levels (**b**-**f**). 45
3.6 Detection of the endocardial contour at different time frames during the cardiac cycle. 46
3.7 Detection of the inner wall of an artery on echobrachial images. 46
3.8 Synthetic ultrasound image showing an object lying on a background with strong speckle noise and the resulting segmentation obtained by our method. 46

4.1 IBD algorithm. 52
4.2 NAS-RIF algorithm. 54

4.3 Image histogram of the picture reported in Figure 4.4b (solid curve) and estimated probability density mixture obtained with the ICE procedure (dotted and dashed curves). 57
4.4 Examples of support determination for some cross-sectional brain SPECT slices. . . 58
4.5 Original PSF defined as a two-dimensional Gaussian distribution with variance $\sigma^2 = 1.5$ in a 7×7 support. 63
4.6 Estimated PSF by the You-Kaveh's algorithm in a 7×7 support. 63
4.7 Examples of brain SPECT image deconvolutions. (**a**) Original image. (**b-g**) Supervised deconvolution methods, respectively ; (**b**) Van-Cittert, (**c**) Landweber, (**d**) RL, (**e**) Tichonov-Miller, (**f**) Super Resolution, (**g**) Molina's algorithm. (**h-k**) Blind deconvolution methods, respectively ; (**h**) IBD, (**i**) Biggs-Lucy, (**j**) You-Kaveh, (**k**) NAS-RIF algorithm. 64
4.8 Examples of human brain cross-sectional SPECT image deconvolutions given by the NAS-RIF algorithm. Top : five consecutive real cross-sectional SPECT slices. Bottom : deconvolution results. 65
4.9 Examples of phantom SPECT image deconvolutions. (**a**) Original image. (**b-g**) Supervised deconvolution methods, respectively ; (**b**) Van-Cittert, (**c**) Landweber, (**d**) RL, (**e**) Tichonov-Miller, (**f**) Super Resolution, (**g**) Molina's algorithm. (**h-k**) Blind deconvolution methods, respectively ; (**h**) IBD, (**i**) Biggs-Lucy, (**j**) You-Kaveh, (**k**) NAS-RIF algorithm. 66
4.10 Examples of some consecutive cross-sectional slices of the segmented phantom (ground truth). 67
4.11 Examples of phantom SPECT image deconvolutions. (**a**) Top : ground truth of the segmented synthetic slice. Bottom : synthetic SPECT slice. (**b-g**) Supervised deconvolution methods, respectively ; (**b**) Van-Cittert, (**c**) Landweber, (**d**) RL, (**e**) Tichonov-Miller, (**f**) Super Resolution, (**g**) Molina's algorithm. (**h-k**) Blind deconvolution methods, respectively ; (**h**) IBD, (**i**) Biggs-Lucy, (**j**) You-Kaveh, (**k**) NAS-RIF algorithm. 68

5.1 3D extension of the NAS-RIF deconvolution algorithm. 72
5.2 Image histogram of the picture reported in Figure 5.4 (solid curve) and estimated probability density mixture obtained with the ICE procedure (dotted and dashed curves). 74
5.3 Estimated parameters for the SPECT volume reported in Figure 5.4. π stands for the proportion of the three classes within the SPECT image. α are the exponential law parameter. μ and σ^2 are the Gaussian law parameters. 74
5.4 Example of an unsupervised three-dimensional Markovian segmentation of a brain SPECT volume using the ICM deterministic relaxation technique and based on the parameters estimated by the ICE procedure. Top : real brain SPECT volume (four central transversal slices). Bottom : three-class Markovian segmentations. 75
5.5 Examples of human brain SPECT volume deconvolution given by the 3D-extended version of the NAS-RIF algorithm combined with the Markovian segmentation-based support finding algorithm. Top : five consecutive real cross-sectional SPECT slices. Bottom : deconvolution results. 78
5.6 Examples of human brain SPECT volume deconvolution given by the 3D-extended version of the NAS-RIF algorithm combined with the Markovian segmentation-based support finding algorithm. Top : five consecutive real cross-sectional SPECT slices. Bottom : deconvolution results. 78

5.7 Examples of human brain SPECT cross-sectional image segmentation and deconvolutions. (**a**) : Original SPECT cross-sectional human brain image. (**b**) : Unsupervised three-dimensional Markovian segmentation. (**c**) : Deconvolution result given by the 3D-extended version of the NAS-RIF algorithm (inverse filter size is $3\times3\times3$). (**d**) : Deconvolution result given by its 2D version (inverse filter size is 5×5) (both deconvolution methods require the same computational load and are combined with the proposed Markovian segmentation-based support-finding algorithm (Figure b)). . . . 79
5.8 Examples of sagittal (**a**)(**c**) and coronal (**b**)(**d**) sections of the original (top) and deconvolved (bottom) human brain SPECT volumes whose cross-sectional slices have been presented in Figure 5.5 for (**a**)(**b**) and in Figure 5.6 for (**c**)(**d**). 80
5.9 Examples of deconvolution obtained by our 3D blind deconvolution approach on some cross-sectional slices of a SPECT phantom. Top : real cross-sectional SPECT phantom slices. Bottom : deconvolution results. 80
5.10 Examples of some consecutive cross-sectional slices of the segmented phantom (ground truth). 81
5.11 Example of deconvolution results on some cross-sectional slices of a synthetic SPECT volume. (**a**) Ground truth of the segmented synthetic slices. (**b**) synthetic SPECT slices. (**c**) Deconvolution results. 81

Chapter 1

INTRODUCTION

Restoration and segmentation remain necessary steps in medical imaging in order to obtain, respectively, qualitative measurements such as the location of objects of interest or the location of singularities associated with lesions or tumors, as well as for quantitative measurements such as area, volume or the analysis of dynamic behavior of anatomical structures over time and across patients.

In image analysis, most of restoration and segmentation methods have recently been expressed as a global optimization problem. The general issue is to find the global minimum of an objective function (also called energy function) describing interactions between the observed and hidden variables. This energy function involves generally two components. One energy term generally expresses the interaction between the solution to be estimated and the observations whereas the other allows to encode constraints on the desired solution. It is the case of Markov Random Field-based segmentation or restoration procedures as well as for deformable template and active contour model-based segmentation techniques. It is also true for recent deconvolution or restoration techniques based on optimization strategy encoding *a priori* known assumed constraints (such as finite-support constraints of the object to be restored, non negativity constraints of the true undistorted image to be recovered, etc.).

The use of such energy-functions falls generally into the Bayesian framework. This is now well established for Markov Random Field-based restoration or segmentation procedures and, although rarely mentioned, it remains true for deformable template or active contour model-based segmentation issues. Nevertheless, energy function-based models are usually easier to formalize than probabilities and this probably explained why these abovementioned problems are rather directly formalized as a cost function minimization problem. This report gives some examples of such energy function-based segmentation or restoration models and apply them in ultrasound or SPECT imagery context. We use Markov Random Field formalism in chapter 2, deformable template-based models in this same chapter, active-contour models in chapter 3, and finally several iterative restoration procedures including optimal recursive inverse filtering models in chapters 4 and 5.

Unfortunately, minimizing such a global energy function is often an intricate problem : the space of possible solutions is generally *very large* and the energy function may exhibit many local *minima*, especially when the image contains strong noise, which is frequently the case in medical imaging, especially in ultrasound and SPECT imagery. Depending on the type of *a priori* known constraints (local or global), on the number of hidden variables to be estimated, and on the nature of the observation field, considered energy landscapes may be very different. A global search is generally impossible due to the size of the configuration space. Nevertheless, several other minimization methods exist. Deterministic relaxation techniques can be efficiently used when a good initial guess of the solution is available, otherwise these methods converge to configurations corresponding to local *minima* of the global energy function. Stochastic methods have the capability of avoiding local *minima* and no initial guess is required to initialize the search procedure. However, one of their major drawbacks is their higher computational load. Finally, coarse-to-fine multi-resolution optimization methods can be used in order to yield fast convergence towards high quality estimates. In our applications, we will have to find the more appropriate (i.e., the faster and the more efficient) minimization technique for each of these different energy functions, related to each segmentation and restoration models, we shall introduce.

This report is organized as follows : chapter 2 presents a deformable template-based detection and tracking procedure of the endocardial contour in a echographic image sequence. In this model, the energy function is optimized *via* an hybrid genetic exploration stochastic procedure. Comparisons with an unsupervised Markov Random Field-based segmentation technique, using a classical local prior model and a deterministic relaxation technique, is also reported in this chapter. In chapter 3, we present an active contour-based model for the detection issue of anatomical structures in ultrasound images (echocardiographic and echobrachial images). In this model we efficiently exploit a multiscale minimization approach. In chapter 4, a comparison of supervised and 2D blind deconvolution/restoration techniques applied in SPECT imagery are reported. Finally, chapter 5 presents a finite-support constraints and optimization strategy-based three-dimensional blind deconvolution models of SPECT images. In this model, due to the convexity of the cost-function used in this procedure, a classical conjugate gradient descent-based minimization technique is efficiently exploited in order to cope this optimization problem.

Chapter 2

SHAPE-BASED SEGMENTATION AND TRACKING OF ANATOMICAL STRUCTURES USING DEFORMABLE TEMPLATES AND A NOISE MODEL ESTIMATION IN AN ECHOGRAPHIC SEQUENCE

This work has been accepted in the International Conference *IEEE Conputer Vision and Pattern Recognition* volume 1, pages 225-230, Fort Collins, Colorado, june 1999 [C1] in a very short version and submitted in this original version to the review *IEEE transaction on medical imaging* [R1].

2.1 Abstract

We present a new approach to shape-based segmentation and tracking of deformable anatomical structures in medical images and validate this approach by detecting and tracking the endocardial contour in an echocardiographic image sequence. To this end, a global prior shape knowledge of the endocardial boundary is captured by a prototype template with a set of predefined global and local deformations to take into account its inherent natural variability over time. In this deformable model-based Bayesian segmentation, the data likelihood model rely on an accurate statistical modeling of the grey level distribution of each class present in the ultrasound image. The parameters of this distribution mixture are given by a preliminary estimation step which takes into account the imaging process as well as the distribution shape of each class present in the image. Then the detection and the tracking problem is stated in a Bayesian framework where it ends up as a cost function minimization problem for each image of the sequence. In our application, this energy optimization problem is efficiently solved by a genetic algorithm combined with a steepest ascent procedure. This technique has been succesfully applied on synthetic images and on a real echocardiographic image sequence.

Key Words : *deformable templates, Markov Random Fields models, tracking, ultrasound image sequence.*

2.2 Introduction

The segmentation of images is of great importance in medical imaging and remains a necessary step to obtain qualitative measurements such as the visualization or the location of objects of interest, the detection of pathological deformations as well as for quantitative measurements such as area, volume or the analysis of dynamic behavior of anatomical structures over time.

Among these images, ultrasound images play a crucial role, because they can be produced at video-rate and therefore allow a dynamic analysis of moving structures. Moreover, the acquisition of these images is non-invasive, rather inexpensive and does not require radiations compared to other medical imaging techniques (as for example CT techniques). On the other hand, the automatic segmentation of anatomical structures in ultrasound images is a real challenge due to speckle noise

and artifacts which are inherent in these images. In addition to the poor image quality (i.e., low signal-to-noise ratio, low resolution and contrast), observed objects, like the heart, are constantly undergoing motion and non-rigid deformation due to their own deformations as well as the deformation of adjacent structures. Another common problem are artifacts caused by turbulent blood flow, air in the lungs, ribs etc. which lead to a loss of signal and temporary occlusion of object boundaries.

Most current automatic segmentation techniques used in medical applications have been developed for CT and MRI images [26] [52] [45] [13]. Among these segmentation schemes, two of the more reliable approaches use the Bayesian inference which allows to take into account the available local or global *a priori* knowledge. This available knowledge is then used to constraint the segmentation process. These methods are based on deformable templates or Markov Random Fields (MRF) models. Both have advantages and shortcomings. The increased popularity of deformable models and templates [26] [52] [45] [13] can be explained by their ability to express, *via* a global prior model, the geometric information and the shape variability of the object of interest to be detected over time and across individuals. The major difference between deformable models and templates lies in the degree of global *a priori* knowledge which is used for constraining the segmentation process. While the deformable model-based approach imposes only generic smoothness constraints on the extracted shape, the deformable template imposes more specific constraints *via* a predefined prior distribution. In MRF-based segmentation approaches, the proper use of available prior information is expressed by a local prior model. This one, described by a Gibbs distribution, expresses the fact that nearby pixels are fairly likely to belong to the same class. This contextual knowledge is captured through the specification of spatially local interactions (called clique potentials) that constraint the segmentation process [4].

The main problem with deformable models is that the likelihood energy are experimentally and heuristically designed and do not statistically segment the image. As for MRF models, they cannot incorporate any global shape constraints in the segmentation process. Nevertheless, contrary to deformable model-based approaches, the likelihood model of an MRF model-based unsupervised segmentation exploits an accurate statistical modeling of the grey level distribution of each class present in the input image [35]. Since it seems that deformable templates provide an interesting framework for structurally analyzing an image and MRFs models provide a good mathematical setting for statistically analyzing an image, it makes sense to capitalize on the benefits of both methods.

To this end, we propose in this paper a deformable template-based approach for the segmentation and the tracking of anatomical deformable structures in medical images. We validate this approach by detecting and tracking the endocardial contour in an echographic image sequence. In that prospect, we first define a prototype template along with a predefined set of admissible transformations in order to capture efficiently the available global *a priori* shape knowledge of the endocardial boundary with its inherent natural variability over time. In this Bayesian segmentation, the likelihood model rely on an accurate Markovian statistical modeling of the grey level distribution of each class present in the image. This likelihood is defined as maximal when the deformed template delineates two regions distributed according the aforementioned distributions. The parameters of this distribution mixture are given by a preliminary statistical estimation method called Iterative Conditional Estimation (ICE) [7]. This estimation scheme rely on a local *a priori* model and takes into account the distribution shape of each class present in the ultrasound image. Then, the detection and the tracking problem of the object of interest is stated in a Bayesian framework as the estimation of the deformation parameters of the template that maximize the posterior Probability Density Function (PDF). In order to efficiently maximize this function, and contrary to many other approaches which use gradient-based optimization methods ([26] [52] [22]) and rely on a proper initialization of the template for each image of the sequence, we will show that an alternative approach consists in

using a genetic exploration of the parameter space combined with a steepest ascent procedure. The optimization method we propose is fast, has the capability of avoiding local minima and no human interactions has to be used to initialize the prototype template on the first frame of the echographic image sequence.

This paper is organized as follows : Sections 2.3 and 2.4 present the deformable template modeling and the proposed Bayesian segmentation approach. In Section 2.5, we detail the distribution mixture parameters estimation step used in the data likelihood model. The stochastic search method using a Genetic Algorithm (GA) combined with a steepest ascent procedure is described in Section 2.6. In Section 2.7, we report some experimental results obtained on synthetic images and on a real ultrasound image sequence. Section 2.8 contains concluding remarks.

2.3 Deformable template representation

In order to model the global shape knowledge of the endocardial contour, we first roughly define it by a set of n labeled points, equally sampled, which approximate the outline of a circle (see Figure 2.1.a) :

$$\gamma_0 = (x_1, y_1 \ , \ x_2, y_2 \ , \ \dots \ , \ x_n, y_n)^T$$

A cubic B-spline shape representation involving these n control points corresponding to "landmarks" is then defined.

This way of modeling objects has been widely considered in the object recognition literature, and particularly in the active contour approach [42]. Such a scheme captures the global structure of a shape without specifying a parametric form for each class of shapes. Let us note that this original prototype template can also be obtained from a learning population and an *off-line* training procedure. This can be done by extracting manually the endocardial outline on different images from an echocardiographic sequence. The extracted shapes have to be normalized in scale and aligned with respect to a common reference frame. A mean shape $\overline{\gamma_0}$ can then be easily computed from this learning population [9]. Nevertheless, the circular crude representation of the endocardial boundary remains close to the one given by this type of training procedure (cf. Figure 2.18.b).

The prototype template γ_0 does not describe the possible instances of the object shape to be detected. In order to take into account the natural variability of the considered object, we introduce a set of admissible affine transformations, ensuring a first crude registration of the shape, and a set of non-affine local and global transformations.

Description of local non-affine transformations

First, a local deformation process δ applied to the n control points is introduced. These local deformations applied to the original shape γ_0 allow to model local random perturbations that can occur for each control point of the template outline. Mathematically, these local deformations are represented by local random translations δ for each control point of the initial shape template γ_0 (cf. Figure 2.1).

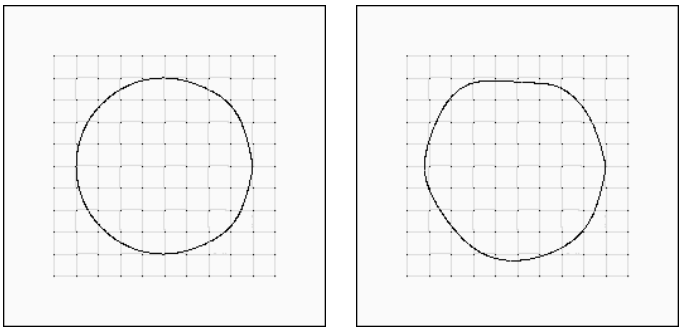

(a) (c)

FIG. **2.1. Local non-affine deformations of the initial prototype template. (a) Initial template (the grid is not part of the model itself). (b) Deformed template with local random perturbations for each control point.**

Description of global non-affine transformations

In order to refine the shape representation, we introduce a global non-affine deformation. The one used in this paper was first proposed by Jain *et al.* and is described in detail in [22]. In this approach, the image is considered to be mapped to the unit square $S = [0,1]^2$. The deformation is then represented by a displacement function denoted $\mathcal{D}(x,y)$. These displacement functions are continuous and equal to zero on the edges of the unit square. The mapping $(x,y) \mapsto (x,y) + \mathcal{D}(x,y)$ is thus a deformation of S, a smooth mapping of the unit square onto itself, that allows to preserve the connectedness of the initial prototype template. The space of such displacement functions is spanned by the following orthogonal bases :

$$e^x_{mn}(x,y) = \Big(2\sin(\pi n x)\cos(\pi m y), 0\Big) \tag{2.1}$$

$$e^y_{mn}(x,y) = \Big(0, 2\cos(\pi n x)\sin(\pi m y)\Big) \tag{2.2}$$

for $m,n = 1,2,\ldots$ Low values of m and/or n correspond to lower frequency components of the deformation in the x and y directions, respectively. The displacement function is then chosen as follows :

$$\mathcal{D}_\xi(x,y) = \sum_{m=1}^{M}\sum_{n=1}^{N} \frac{\xi^x_{mn} e^x_{mn}(x,y) + \xi^y_{mn} e^y_{mn}(x,y)}{\lambda_{mn}} \tag{2.3}$$

where $\lambda_{mn} = \pi^2(n^2+m^2)$ are the normalizing constants. The parameter vectors ξ are the projections of the displacement function on the orthogonal basis defined in Equations (2.1) and (2.2). In order to allow a sufficiently wide range of possible deformations, while keeping the number of parameters reasonable, we use $M = N = 2$.

Figure 2.2 illustrates the series of deformations of the initial template using higher order terms and different values of M and N. This template is drawn on a rectangular grid to visualize the deformations of the original model but this grid is not part of the model itself. We can see that large value of the deformation coefficients ξ result in large deformation of the template. We can also notice that the deformation becomes more complex as higher frequency components are added to the displacement function $\mathcal{D}$.

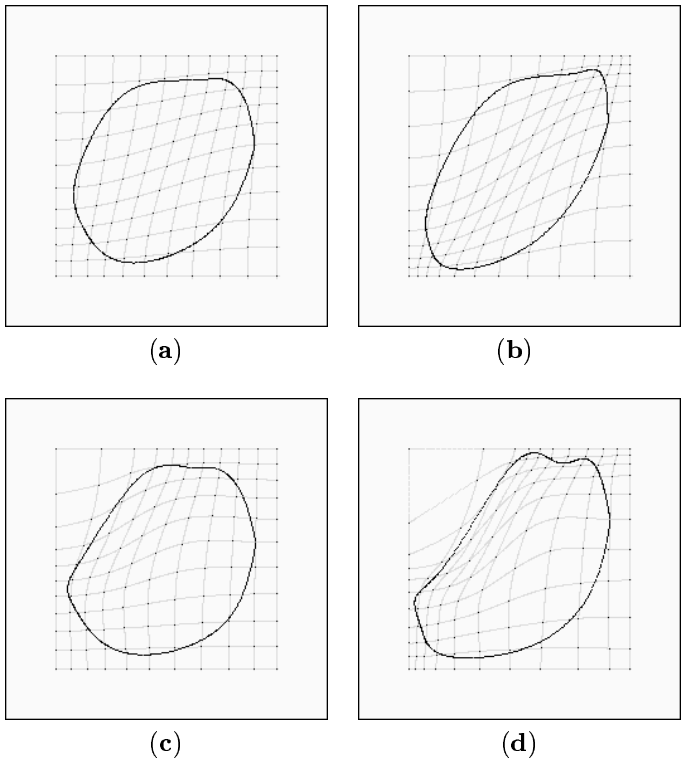

FIG. **2.2. Global non-affine deformations on the locally deformed template reported in Figure 2.1.b. This deformation uses the displacement functions defined in Equation (2.3) along with progressively higher order frequency components and higher values of deformation coefficients** ξ_{mn}. **(a)** $M=N=1$ **and** $\xi^x_{11}=\xi^y_{11}=1$. **(b)** $M=N=1$ **and** $\xi^x_{mn}=\xi^y_{mn}=2 \quad \forall m,n \in \{0,1\}^2$. **(c)** $M=N=2$ **and** $\xi^x_{mn}=\xi^y_{mn}=1$ $\forall m,n \in \{0,1,2\}^2$. **(d)** $M=N=2$ **and** $\xi^x_{mn}=\xi^y_{mn}=2 \quad \forall m,n \in \{0,1,2\}^2$.

Description of affine transformations

Finally, we introduce a set of admissible linear transformations on γ. These deformations involve translation, scaling, rotation, and stretching of the template as shown in Figure 2.3. Corresponding transformations are given by :

$$A_s = \begin{pmatrix} s & 0 \\ 0 & s \end{pmatrix} \qquad A_\alpha = \begin{pmatrix} cos\alpha & -sin\alpha \\ sin\alpha & cos\alpha \end{pmatrix} \qquad A_t = \begin{pmatrix} 1 & 0 \\ 0 & t \end{pmatrix}$$

with s, t and α being respectively the scale, stretch parameters and the angle of rotation.

Let now γ_θ be a deformed version of the original prototype γ_0 according to the aforementioned transformations with parameter vector θ. The globally deformed template is then defined by :

$$\gamma_\theta = A_s A_t A_\alpha \Big(\gamma_0 + \delta + \mathcal{D}(\gamma_0 + \delta)\Big) + \mathbf{t}$$

where $\mathbf{t} = (t_x, t_y)$ and $A_s A_t A_\alpha$ account for rigid affine transformations of the template ($\mathbf{t}$ is a global translation vector). $\delta = (\delta_1, \delta_2, \ldots, \delta_{n-2})$ with $\delta_i = (\delta_{x_i}, \delta_{y_i})^T$ is the local translation vector associated to the $(n-2)$ translation vectors of the non-affine local deformations and $\mathcal{D}$, the displacement functions of the global non-affine deformations. $(n-2)$ translation vectors, associated to the n control points, except the first and last one, are considered in order to ensure the connectedness of the prototype template [1].

A global configuration of the deformable template is thus described by five parameters corresponding to affine transformations, four pairs of global non affine deformation parameters (ξ^x_{mn}, ξ^y_{mn}), and $(n-2)$ pairs of translation vector $(\delta_{x_i}, \delta_{y_i})$ respectively. The circular prototype template along with the set of aforementioned transformations constitutes our global prior model describing the different possible configurations of the shape of interest. This three-level description of deformations has shown itself to be very flexible for representing accurately the inherent natural variability of the endocardial contour during the cardiac cycle (see Section 2.7 in which a selection of shape models is presented in Figure 2.16). Now we have defined our global prior model, we can turn our attention to the likelihood model. We consider this in the next section.

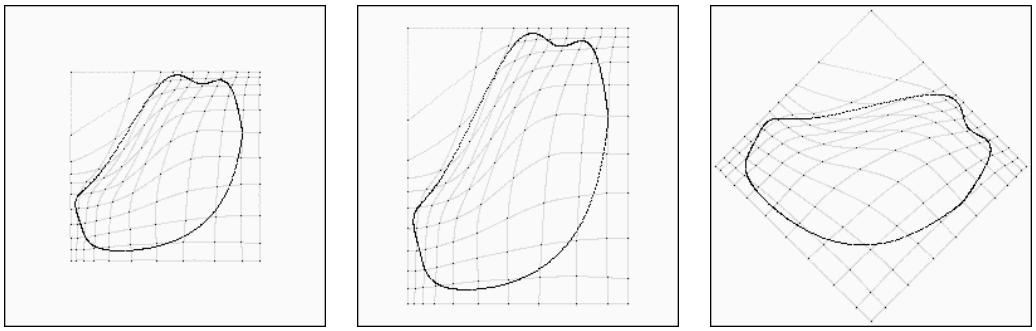

(a) (b) (c)

FIG. **2.3. Considered affine transformations applied on the locally and globally deformed prototype template reported in Figure 2.2.d. (a) Scale transformation. (b) Stretch transformation. (c) Rotation transformation.**

2.4 Segmentation model

2.4.1 Introduction

As mentioned in the introduction, the automatic segmentation of anatomical structures in ultrasound images is especially challenging due to artifacts caused by the speckle noise effect. This partially correlated noise, inherent to the imaging process, lead to a poor image quality (with low resolution, contrast and signal-to-noise ratio) on which the sharpness of anatomical structure contours is noticeably reduced (cf. Figures 2.4.a and 2.4.b).

[1] The first and last point are the same and their associated local non-affine deformation is incorporated in the global translation vector $\mathbf{t}$.

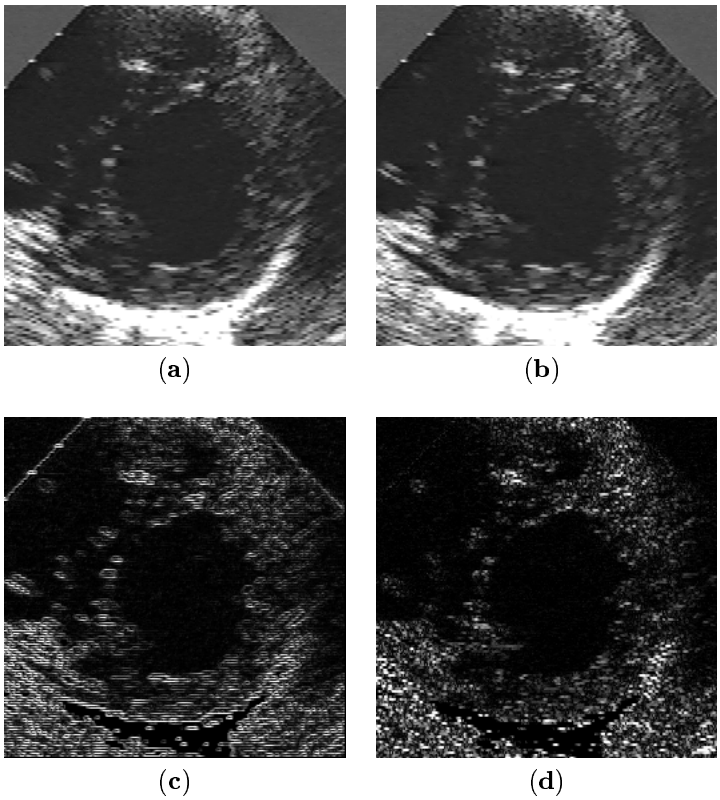

FIG. 2.4. **Spatial and temporal edge map derived from two successive frames of an echographic sequence. (a) Echogram (frame 1). (b) Echogram (frame 2). (c) Spatial gradient map. (d) Temporal gradient map.**

In a commonly used deformable model-based Bayesian segmentation approach, these contours (or some spatial and/or temporal gradient measures derived from the input image) are generally exploited in the data likelihood model. In a Bayesian approach, this likelihood model aims at expressing a measure of similarity between the deformed template and the object(s) present in the image and constrains the deformable template to be attracted and aligned, *via* an appropriate likelihood energy term, to the salient edges of the object to be detected [26] [22] [29] [23] [27].

Due to the speckle noise, our likelihood model cannot rely efficiently on this type of gradient measures. Figure 2.4 illustrates the temporal and spatial edge map derived from two ultrasound images. We can see that speckle noise effect induces wrong spatial and temporal edge detection that cannot be exploited in a reliable likelihood model ensuring a robust contour tracking procedure. Instead, we propose here a region oriented statistical approach. More precisely, we propose to model and use the grey level statistical distribution of each homogeneous region existing in an echogram and to exploit an *a priori* information about the location of the endocardium with respect to each other anatomical structures present in the ultrasound image. This *a priori* anatomical information expresses the fact that the endocardial contour delineates two homogeneous regions $\{\mathcal{R}_0, \mathcal{R}_1\}$. The first one, called the *blood* zone ($\mathcal{R}_0$), arises from the low acoustic wave reverberation in the ventricular cavity (filled with blood). The second one, called the *muscle* region ($\mathcal{R}_1$), is due to the acoustic signal reverberation on the cardiac muscles. Each aforementioned region has completely different grey level intensity distribution and each pixel of the input image has a membership likelihood to each class $\{e_0 = blood, e_1 = muscle\}$ that we can defined by the following Probability Density Functions (PDFs) :

$$P_{Y_s/X_s}(y_s/x_s = e_i) \qquad i \in \{0,1\}$$

where y_s designates the grey level of the pixel at site s and x_s is its associated class label. Y_s and X_s represent the random variables associated to the realizations x_s and y_s respectively. Assuming that N distinct homogeneous regions are present in the input image ($N = 2$ in our application), the maximization over θ of the following expression :

$$P_{Y/\Theta}(y/\theta) = \prod_{j=0}^{N-1} \prod_{s:x_s=e_j} P_{Y_s/X_s}(y_s/x_s) \tag{2.4}$$

allows to find the optimal template (or the optimal deformation parameter vector θ of the original prototype template γ_0) which best matches the image. Equivalently, we can minimize $-\ln P_{Y/\Theta}(y/\theta)$ and use this previous expression as our energy function. This energy function is not heuristic and statistically segments the image in a Maximum Likelihood sense. Let us note also that this term defined the likelihood distribution used in a classical Markovian segmentation (see Section 2.7 and Figure 2.15).

2.4.2 Joint model

In that prospect, we let the template define two regions (cf. Figure 2.5) : the first one is the set of pixels *inside* the region delimited by the prototype template γ_θ, and is denoted $\gamma_\theta^\bullet$. The second one is the outside region, defined by the set of pixels located *on* the contour of the deformed template with a slightly superior scale. This last one is denoted γ_θ° (with $\gamma_\theta^\circ = \gamma_{(\ldots,s+\delta s,\ldots)}$, and we recall that s is the scale parameter of the considered affine transformations). From this, we propose the following joint model through the Gibbs distribution :

$$P_{\Theta,Y}(\theta, y) = \frac{1}{Z} \exp\Big\{-\epsilon(\theta, y)\Big\}$$

where Z is a normalizing constant and ϵ is an objective function measuring how well a given instance of deformed template γ_θ fits the content of the input image y. The energy function $\epsilon(\theta, y)$ is composed of two terms as explained below :

• **Likelihood energy term :** this first energy term measures the likelihood of the image and is "related" to the log-likelihood distribution defined in Equation (2.4).

$$\epsilon_l(\theta, y) = -\frac{1}{N_{\gamma_\theta^\bullet}} \sum_{s \in \gamma_\theta^\bullet} \ln P_{Y_s/X_s}(y_s/e_0) - \frac{1}{N_{\gamma_\theta^\circ}} \sum_{s \in \gamma_\theta^\circ} \ln P_{Y_s/X_s}(y_s/e_1)$$

where the summation of the first and second term of $\epsilon_l(\theta, y)$ is over all the $N_{\gamma_\theta^\bullet}$ pixels inside the region defined by the deformed template γ_θ and over all the $N_{\gamma_\theta^\circ}$ pixels delimited by γ_θ° respectively. Note that the two weighting factors are necessary in order to get a scale-invariant likelihood measure. This function attains its minimum value when the deformed template delimits exactly two homogeneous regions with grey level distribution corresponding to *blood* and *muscle* class for the region $\gamma_\theta^\bullet$ and γ_θ° respectively.

• **Prior energy term :** the second term penalizes the deviation of the deformed template γ_θ from the original prototype γ_0. This function does not penalize affine transformations and is close to the one proposed by Jain *et al.* [22], except for the second term.

$$\epsilon_p(\theta, y) = \Big(\sum_{\xi_i \in \xi} \big[(\xi_i^x)^2 + (\xi_i^y)^2 \big] + \sum_{\delta_i \in \delta} (\delta_i)^2 \Big)$$

where (ξ_i^x, ξ_i^y) and δ_i correspond to displacement function parameters of the global non-affine deformation and the translation parameter vector of the non-affine local deformations respectively (see Section 2.3).

2.4.3 MAP detection

Using these two energy terms, the joint distribution $P_{\Theta,Y}(\theta, y)$ can be written as :

$$P_{\Theta,Y}(\theta, y) = \frac{1}{Z} \exp - \Big\{ \underbrace{\epsilon_l(\theta, y) + \rho\, \epsilon_p(\theta, y)}_{\epsilon(\theta, y)} \Big\}$$

where the factor ρ provides a relative weighting between the two penalty terms and allows to control the "rigidity" of the template. The posterior distribution deduced from Equation (2.5) is given by :

$$P_{\Theta/Y}(\theta/y) = \frac{1}{Z_y} \exp \Big\{ -\epsilon(\theta, y) \Big\}$$

where Z_y is a normalizing constant depending on y only. We formulate now the detection problem as the search of the *Maximum A Posteriori* (MAP) estimation of θ :

$$\hat{\theta}_{MAP} \in \arg\max_\theta \Big\{ P_{\Theta/Y}(\theta/y) \Big\} \tag{2.5}$$

$$\in \arg\min_\theta \epsilon(\theta, y) \tag{2.6}$$

The search of $\hat{\theta}_{MAP}$ is therefore equivalent to the minimization of the non concave following objective function :

$$\epsilon(\theta, y) = -\frac{1}{N_{\gamma_\theta^\bullet}} \sum_{s \in \gamma_\theta^\bullet} \ln P_{Y_s/X_s}(y_s/e_0) \quad - \quad \frac{1}{N_{\gamma_\theta^\circ}} \sum_{s \in \gamma_\theta^\circ} \ln P_{Y_s/X_s}(y_s/e_1)$$
$$+ \quad \rho \left(\sum_{\xi_i \in \xi} \left[(\xi_i^x)^2 + (\xi_i^y)^2 \right] + \sum_{\delta_i \in \delta} (\delta_i)^2 \right)$$

This function is minimal when the deformed template delineates two homogeneous regions (*blood* and *muscle* for our application) distributed according to the grey-level distribution corresponding to each region and when the deformed template is not too different from the original prototype (in the non-affine deformations sense).

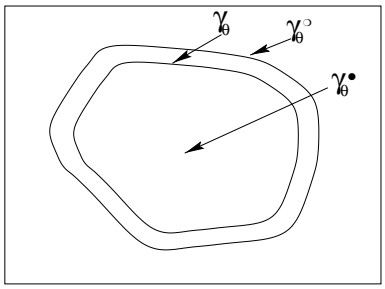

FIG. **2.5. The two different regions delimited by the template at a specific location and transformation. $\gamma_\theta^\bullet$ is the set of pixels inside the region delimited by the deformed prototype template γ_θ. γ_θ° is the set of pixels located on the contour of γ_θ with a slightly superior scale.**

In order to get an unsupervised deformable-based segmentation scheme, we have now to estimate the distribution mixture parameters, i.e., the distribution parameters associated to each region, *blood* and *muscle* of the ultrasound image. This estimation will allow us to compute the probability map for each class. The main difficulty is that the distribution mixture parameter estimation is required for the deformable model-based segmentation process, while the segmentation result is needed for mixture parameter estimation. To circumvent this problem, a solution consists in implementing the estimation and the segmentation procedure alternatively. In that prospect, we can start with an initial configuration of the template and use the resulting partitioned data in order to estimate the grey level distribution parameters associated to each region. This procedure can then be repeated until convergence. Nevertheless, it is clear that this process is sensitive to the initial placement of the template. The alternative approach we choose to solve this unsupervised segmentation problem consists in having a two-step process. First, a parameter estimation step in which we have to estimate the distribution mixture parameter also called the noise model parameters. We consider this estimation step in the next section. Then, a second step (segmentation step) in which we apply the deformable model-based segmentation algorithm with the estimated values of mixture parameters.

2.5 Distribution mixture parameter estimation

2.5.1 Complete and incomplete data

Consider a couple of random fields $Z = (X, Y)$, where $Y = \{Y_s, s \in S\}$ represents the field of observations located on a lattice S of N sites s (associated to the N pixels of the input image), and $X = \{X_s, s \in S\}$ the label field (related to N *blood* or *muscle* class labels of the segmented image). Each Y_s takes its value in $\{0, \ldots, 255\}$, and each X_s in $\{e_0 = \textit{blood},\ e_1 = \textit{muscle}\}$. The distribution of (X, Y) is defined, firstly, by prior distribution $P_X(x)$, supposed to be stationary and Markovian in this distribution mixture parameter estimation step, and secondly, by site-wise likelihoods $P_{Y_s/X_s}(y_s/x_s)$, depending on class label x_s. Assuming independence between each random variable Y_s given X_s, the joint distribution $P_{X,Y}(x, y)$ can be written as :

$$P_{X,Y}(x, y) = P_X(x) \underbrace{\prod_s P_{Y_s/X_s}(y_s/x_s)}_{P_{Y/X}(y/x)} \tag{2.7}$$

The observable Y is called the "incomplete data", and Z the "complete data".

2.5.2 Estimation of the mixture parameters for the complete data

Assuming the segmentation result x is known or observable (i.e., we know the "complete data"), the parameters of the distribution mixture can then be easily computed. To this end, and in order to take into account the speckle noise phenomenon [18] in the reverberation areas, we model the conditional density function for the *blood* and *muscle* class by a Rayleigh law [47]. It turns out that, for our application, we have to introduce another parameter to shift this distribution, to take the different processes forming the final ultrasound image into account (e.g., automatic control of gain, coding, reduction of the dynamic, offset, ...). We propose to consider the following expression :

$$\mathcal{R}_Y(y; min, \alpha) = \frac{y_s - min}{\alpha^2} \exp\left(-\frac{(y_s - min)^2}{2\alpha^2}\right)$$

with $y > min$ and $\alpha > 0$. α is the scale parameter. Let now $Y = (Y_1, Y_2, \ldots, Y_M)$ be M random variables, independent and identically distributed according to a *single* Rayleigh law $\mathcal{R}_Y(y; \Phi_y)$, and $y = (y_1, y_2, \ldots, y_M)$ a realization of Y. The Maximum Likelihood estimate of $\Phi_y = (min, \alpha)$ consists in finding $\hat{\Phi}_y$, such that :

$$\hat{\Phi}_y = \arg\max_{\Phi_y} \ln P_{Y/\Phi_y}(y/\Phi_y)$$

where $\ln P_{Y/\Phi_y}(y/\Phi_y)$ is the log-likelihood function. Assuming independence between each random variable, we obtain the following ML estimators of the "complete data" for the sample y [47] :

$$\begin{aligned} \widehat{min}_{ML} &\approx \hat{y}_{min} - 1 \\ \hat{\alpha}^2_{ML} &= \frac{1}{2M} \sum_{i=1}^{M} (y_i - \widehat{min}_{ML})^2 \end{aligned}$$

where $\hat{y}_{min} = \min_i(y_i)$, is the minimum grey level of the sample y.

2.5.3 *Ice procedure*

When the segmentation result is unknown (or unobservable), the considered problem is more complex. In this case, the conditional likelihood $P_{Y/X}(y/x)$ depends on parameter vector Φ_y, which is the distribution mixture parameter vector to be estimated. In order to obtain a reliable estimation of this parameter, we resort to the ICE algorithm. This procedure, described in detail in [46] [43], is briefly recalled here. This method relies on an estimator $\hat{\Phi}_y(X,Y)$ with good asymptotic properties (consistency properties) for completely observed data case. When X is unobservable, this procedure starts from an initial parameter vector $\Phi_y^{[0]}$ (not too far from the optimal one) and generates a sequence of parameter vectors $\Phi_y^{[1]}, \Phi_y^{[2]}, \ldots, \Phi_y^{[k]}$ hopefully leading to the optimal parameters ($\lim_{k\to\infty} \Phi_y^{[k]} = \Phi_{y\ \text{optimal}}$). To this end, $\Phi_y^{[k+1]}$ at step $(k+1)$ is chosen as the conditional expectation of $\hat{\Phi}_y$ given $Y = y$, computed according to the current value $\Phi_y^{[k]}$. It is the best approximation of Φ_y in terms of the mean squares error [46] [43]. By denoting E_k, the expectation relative to parameter vector $\Phi_y^{[k]}$, this iterative procedure is defined as follows :

- Consider an initial parameter vector $\Phi_y^{[0]}$.
- $\Phi_y^{[k+1]}$ is computed from $\Phi_y^{[k]}$ and $Y = y$ by :

$$\Phi_y^{[k+1]} \quad = \quad E_k\left[\hat{\Phi}_y(X,Y)|Y=y\right] \tag{2.8}$$

The computation of this expectation is impossible in practice, but we can approach Equation (2.8) thanks to the law of large numbers by :

$$\Phi_y^{[k+1]} \quad = \quad \frac{1}{n}\left[\hat{\Phi}_y(x_{(1)},y) + \cdots + \hat{\Phi}_y(x_{(n)},y)\right]$$

$x_{(i)},\ i = 1,\ldots,n$ are realizations of X drawn according to the posterior distribution $P(x/y,\Phi_y^{[k]})$. As explained in subsection 2.5.2, for complete data-based estimator $\hat{\Phi}_y(X,Y)$, we can use a Maximum Likelihood (ML) estimator for the noise model parameter. Finally, in order to simulate realizations of X according to the posterior distribution $P_{X/Y,\Phi_y}(x/y,\Phi_y)$, we can use the Gibbs sampler algorithm [16].

Contrary to classical EM (Expectation Maximization) [12] or SEM (Stochastic Expectation Maximization) [33] algorithms, the ICE procedure is quite general and can be adapted to different kinds of conditional distributions involved in the mixture to be estimated. As shown in the following, this algorithm can be used to estimate a non-Gaussian law distribution mixture [35]. Besides, this estimation scheme allows to express constraints in the Gibbs sampler simulation process *via* its local prior model. In order to decrease the computational load, we can take $n = 1$ (i.e., simulate only a single MRF realization) to estimate Φ_y, without altering the quality of the estimation [7].

2.5.4 *Estimation of the mixture parameters for the incomplete data*

Let us recall that this parameter estimation procedure assumes that the luminance distribution within *blood* and *muscle* regions follows two different Rayleigh PDFs. We aim at estimating the parameters of these two PDFs. For the local *a priori* model of the Gibbs sampler used to simulate realizations of the posterior distribution, we adopt a standard isotropic Potts model with the 8-connexity spatial neighborhood [4]. In this model, there are four parameters, called "the clique parameters" denoted $\beta_1, \beta_2, \beta_3, \beta_4$ and associated to the horizontal, vertical, right and left diagonal binary cliques respectively (see Figure 2.6). Given this *a priori* model, the prior distribution $P_X(x)$ can be written as :

$$P_X(x) = \exp\Big\{ - \sum_{<s,t>} \beta_{st}\big(1 - \delta(x_s, x_t)\big)\Big\}$$

where summation is taken over all pairs of neighboring sites and $\delta(.)$ is the Kronecker delta function. In order to favor homogeneous regions with no privileged orientation in the Gibbs sampler simulation process, we choose $\beta_{st} = \beta_1 = \beta_2 = \beta_3 = \beta_4 = 1$. The parameter estimation procedure for the incomplete data using the ICE procedure is outlined below :

Parameter initialization : The initial parameter values have a significant impact on the convergence of the ICE procedure and on the quality of the final estimates. We can use the initialization method described in [36] or give a parameter vector not "too far" from the optimal one.

ICE procedure : $\Phi_y^{[k+1]}$ is computed from $\Phi_y^{[k]}$ in the following way :

1. Using the Gibbs sampler, one realization x is simulated according to the posterior distribution $P_{X/Y,\Phi_y}(x/y, \Phi_y^{[k]})$, with parameter vector $\Phi_y^{[k]}$.

2. The parameter vector $\Phi_y^{[k+1]}$ is estimated with the ML estimator of the "complete data" $\hat{\Phi}_y(x, y)$ described in subsection 2.5.2.

3. If the sequence Φ_y becomes steady (i.e, if the variance of the N last estimations is below a given threshold), the ICE procedure is ended, else we return to step 1.

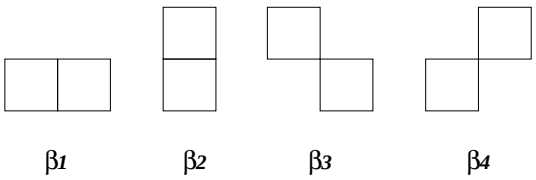

FIG. **2.6**. 2^{nd} **order neighborhood and associated two-site cliques.**

Figure 2.7 represents the estimated distribution mixture on the echogram shown in Figure 2.4.a and the histogram of this ultrasound image : the two site-wise likelihoods $P_{Y_s/X_s,\Phi_y}(y_s/e_i, \Phi_y)$, $i = 0, 1$, (weighted by the estimated proportion π_i of each class e_i) are superimposed to the image histogram. Corresponding estimates obtained by the ICE procedure, requiring about twelve iterations, are given in Table 2.1. The quality of the estimations is difficult to appreciate in absence of ground truth values. We can roughly perform such an evaluation by comparing the image histogram (solid curve) with the probability density mixture corresponding parameters (dotted and dashed curves). Estimation results on synthetic images with ground truth values will be given in Section 2.7 in order to appreciate the robustness of this procedure and the quality of the estimations. Experiments have shown that the distribution mixture parameters keep constant for all the images extracted of the same echographic sequence. For this reason, and in order to decrease the computational load, the mixture parameters are computed once and for all on the first frame of the echographic sequence. Now that we are able to estimate the parameters of the mixture-based data model, we can turn our attention to the optimization problem of $\epsilon(\theta, y)$.

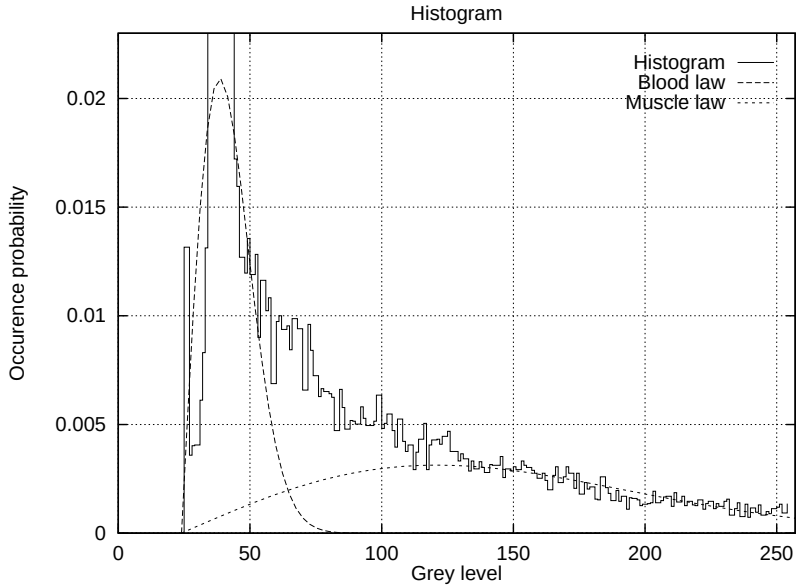

FIG. **2.7. Image histogram of the picture reported in Figure 2.4.a (solid curve) and estimated probability density mixture obtained with the ICE procedure (dotted and dashed curves).**

	ECI Procedure		
$\Phi^{\text{final}}_{y_{(blood)}}$	$0.48_{(\pi)}$	$24_{(min)}$	$207_{(\alpha^2)}$
$\Phi^{\text{final}}_{y_{(muscle)}}$	$0.52_{(\pi)}$	$24_{(min)}$	$9436_{(\alpha^2)}$

TAB. **2.1. Estimated parameters for the picture reported in Figure 2.4.a. π stands for the proportion of the two classes within the ultrasound image. min and α are the Rayleigh law parameters.**

2.6 Optimization Problem

The objective function to be minimized in Equation (2.6) is a complex function with several local extrema over the deformation parameter space. A global search is usually impossible due to the size of the configuration space. Instead, we have implemented a Genetic Algorithm-based optimization technique.

Genetic Algorithms (GA) are a class of robust stochastic search and global optimization procedures which mimic the evolution of natural systems [17]. The algorithm acts in an iterative way by allowing parallel evolution in a population of N individuals. Each individual represents a point of the search space and is a candidate solution to the optimization problem. It is represented by a string or "chromosome", which is composed of a list of L features (corresponding to the L searched parameters). The parameters have to be encoded in an appropriate manner. The most common approach is to quantize the parameter values and to binary code them. The fitness of the various individuals (the tentative "solution") to the environment is expressed by a fitness function, which, after the characteristics contained in a chromosome have been decoded, gives a "performance" value

to the string. Genetic search is carried out in a sequence of "generations". In each generation, a new population of N chromosomes is created with genetic operators. These operators mimic the biological phenomena of *selection*, *crossover* and *mutation*. The choice of the solution upon which they are used is dictated by the evolutionary principle of the "survival of the fittest". The algorithm begins with an initial population of N chromosomes randomly chosen and terminates when either a specified number of iterations has been performed or a maximally fitted individual has emerged.

In our application, let us recall that we have to optimize a L dimensional function. Each of the L parameters θ_l is quantified on q bits in order to take any value within the predefined range $[\theta_{L\min}, \theta_{L\max}]$. Therefore, the i^{th} chromosome, denoted $[\theta]_i$, is a string of qL bits length :

$$[\theta]_i = (\underbrace{c^i_{11}, c^i_{12}, \ldots, c^i_{1q}}_{\theta_1} ; \underbrace{c^i_{21}, c^i_{22}, \ldots, c^i_{2q}}_{\theta_2} ; \ \cdots \ ; \underbrace{c^i_{L1}, c^i_{L2}, \ldots, c^i_{Lq}}_{\theta_L})$$

where c^i_{kl} designates the l^{th} bits associated to the k^{th} parameter and θ is the parameter vector associated to the chromosome $[\theta]_i$ after decoding.

Fitness Measure :

We can easily derive a fitness measure $\mathcal{F}$ (to be maximized) directly from equation (2.6) (the energy function ϵ to be minimized). To turn $\epsilon(\theta, y)$ into a fitness measure for use in genetic algorithm, we can choose :

$$\mathcal{F}([\theta]_i) = \exp\Big\{ -\epsilon(\theta, y)\Big\}$$

The following is the detail of the *selection*, *crossover*, and *mutation* operators. The associated parameters used in our application will be given in Section 2.7.

Selection :

Individuals with higher fitness survive and individuals with lower fitness die. Let us assume that at iteration k, the population of the GA is the set of N chromosomes :

$$\text{POP}^k = \Big\{ [\theta]^k_1 \ , \ \cdots \ , \ [\theta]^k_N \Big\}$$

Generation of the next population is based on the evaluation of $\mathcal{F}$ for all individuals of POP^k. More precisely, we probabilistically select each chromosome for "reproducing" in the next generation, using their relative fitness :

$$p([\theta]^k_i) = \frac{\mathcal{F}([\theta]^k_i)}{\sum_{j=1}^{N} \mathcal{F}([\theta]^k_j)}$$

Crossover :

A pair of chromosomes is picked up at random and the single-point crossover operator is applied according to a fixed crossover probability. For this operation, a random number in the range of 0 to the length Lq of the string is generated. This is called the crossover point. The portions of two strings lying to the right of the crossover point are interchanged to yield two new strings as shown in Figure 2.8.

Mutation :

Mutation consists in considering in turn each bit of a given chromosome and changing its value with a predefined low probability called the mutation rate.

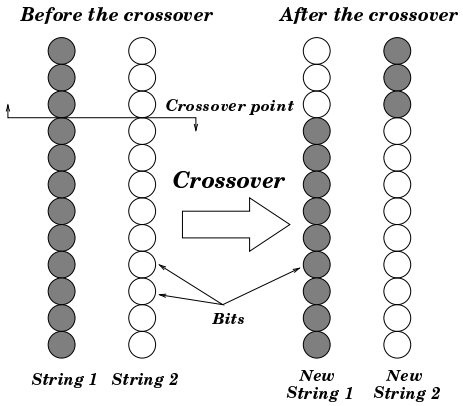

FIG. **2.8. An example of crossover with the partial exchange of information.**

In order to speed up the convergence rate, we have developed two strategies and we have combined them :

1.– The first one is an elite-preservation strategy [17] : the individual with the highest fitness survives to be an individual of the next generation.

2.– The second strategy (called hybrid GA [17]) consists in associating the genetic search with a local optimization technique. In each generation, a percentage of the best individuals are used to initialize a gradient ascent technique. Therefore, these best individuals explore local neighborhoods in the parameter space to find a point of higher fitness.

In our application, these two strategies are used together in an efficient way to create a global optimization technique called "hybrid genetic algorithm with an elitist strategy".

2.7 Experimental results

2.7.1 Distribution mixture estimation step

Based on the distribution mixture parameters given by the ICE procedure (see Table 2.1), we can compute the probability map for the *blood* and *muscle* classes. This map exhibits sharp boundaries between high and low probability regions for each class. As a result, the probability maps have a high gradient at the boundary of the different regions and low gradient everywhere else. In order to constrain the deformable model to be efficiently attracted to the boundaries of two homogeneous regions by the gradient-based local optimization procedure, we need to spread their region of influence to a larger area. To do this, we convolve 5 times each probability maps with the following 3×3 2D Gaussian mask : $[1, 2, 1\,;\, 2, 4, 2\,;\, 1, 2, 1]$. Besides, due to the speckle noise effect, the probability maps, associated to each class are very noisy. The smoothing process counteracts this problem as well. Figure 2.9 shows the smoothed probability map for the ultrasound image reported in Figure 2.4.a.

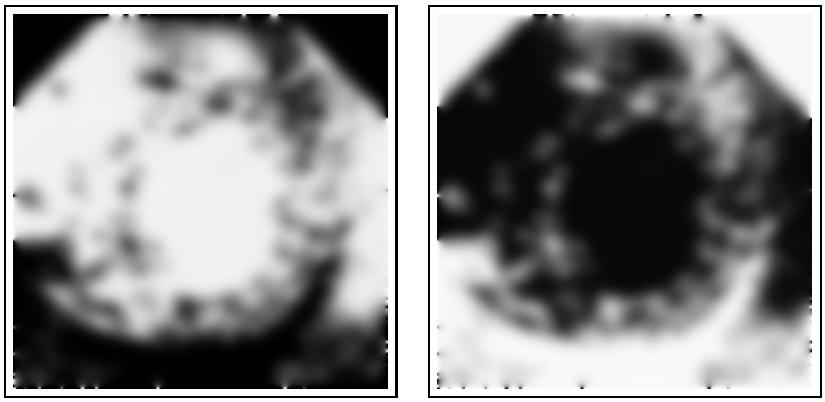

(a) (b)

FIG. **2.9. Smoothed probability map for the ultrasound image reported in Figure 2.4.a (a) Probability map associated to the *blood* class. (b) Probability map associated to the *muscle* class.**

2.7.2 Detection step

This detection step has been carried out with the hybrid genetic algorithm using the elitist strategy described in Section 2.6 and after the distribution mixture estimation step proposed in Section 2.5. In order to reduce the size of the parameter search space, the stochastic exploration based on the GA is used to only estimate the affine transformation parameters (five parameters to be estimated). This affine deformation parameter estimation ensures a first crude registration of the shape to be detected. The local exploration technique of the best individuals selected by the GA, which is based on the steepest ascent procedure, is then used to estimate the whole parameter vector (including the global and local non-affine deformations parameters).

Tests have shown that this optimization procedure is not very sensitive to the control parameters. In our application, these parameters are commonly used [17] and are the following : population size = 100, crossover rate = 0.8, mutation rate = 0.008, maximum number of generations = 30. Parameters value are quantified on $q = 8$ bits. At each generation, we select 5 % of the best individuals (i.e., five best parameter vectors) for the hybridation with the local optimization technique. The prototype template is a connected 12-points model ($n = 12$). The weighting factor penalizing the prior term with respect to the likelihood term is set to 0.1 and the size of the image is 256×256 pixels. All these parameters keep constant for the detection and the tracking step. Using this procedure, a reliable detection of the endocardial contour is obtained for all images of the echographic sequence. Our GA takes about 5-20 generations to converge to the true solution. In fact, the convergence rate can vary depending on the complexity of the objective function $\epsilon(\theta, y)$ to be minimized (or the complexity of the input image and/or the shape to be extracted). Tests have shown that, after a learning step (i.e., typically 3-6 generations or iterations of the algorithm), the genetic exploration of the search space parameter provides good initializations for the local exploration technique. In our application, the optimization procedure for the detection process takes about three minutes (average CPU time) on a standard Sun/Sparc2 workstation.

Figures 2.10 and 2.11 show two real echograms extracted from an echographic sequence and illustrate the best deformed template and the best 5 % set of templates before the gradient ascent technique, and thus before the estimation of parameters associated to global and local non-affine

transformations, for successive iterations or generations of the genetic search. In spite of the speckle noise and a random initial population for the GA, an accurate and reliable detection of the endocardial border is obtained.

Figures 2.12 and 2.13 show two synthetic images with synthetic Rayleigh noise and the resulting detection/segmentation obtained by the proposed deformable template-based unsupervised segmentation method. Real parameters of the distribution mixture and resulting segmentations can be compared to estimated parameters by the ICE procedure (see Table 2.2) and to the ground truth segmentations (cf. Figure 2.14). We can notice that faithful noise model estimations and accurate segmentation are obtained. These experiments demonstrate that the proposed detection and segmentation scheme is reliable, robust and avoid a manual initialization of the model.

We can compare the result of a Markovian segmentation of the ultrasound image in two classes (*blood*, *muscle*) based on the parameters estimation given by the ICE procedure. In this framework, the segmentation issue can be viewed as a statistical labelling problem according to a global Bayesian formulation in which the posterior distribution $P_{X/Y}(x/y) \propto \exp -U(x,y)$ has to be maximized [4]. In this case, the corresponding posterior energy is :

$$U(x,y) = \underbrace{\sum_{s \in S} -\ln P_{Y_s/X_s}(y_s/x_s)}_{U_1(x,y)} + \underbrace{\sum_{<s,t>} \beta_{s,t} \left[1 - \delta(x_s, x_t)\right]}_{U_2(x)}$$

where U_1 expresses the adequacy between observations and labels, and U_2 represents the energy of the *a priori* model. $\beta_{st} = \beta_1 = \beta_2 = \beta_3 = \beta_4 = 1$ according to the type of the clique $<s,t>$ horizontal, vertical, right and left diagonal respectively (see Figure 2.6). We use the deterministic algorithm ICM [4] to minimize this global energy function. For the initialization of this algorithm, we exploit the segmentation map obtained by a ML segmentation. We can notice (cf. Figure 2.15) that the resulting map exhibits unproper *blood* or *muscle* areas due to strong speckle noise. The boundary of the endocardial contour cannot be efficiently extracted by this method due to the unproper local prior model.

2.7.3 Tracking step

The tracking strategy used in our application is the following : the final estimate of the previous time frame is used as an initialization for the steepest ascent procedure for the current time frame. If the resulting value of energy ϵ at convergence is higher than a given threshold, we can assume that the inter-frame motion is small and this strategy allows to provide a proper initialization of the template for the local exploration technique used on the next frame. In this case, the result of the gradient ascent technique gives the final result for the current time frame. Otherwise, (i.e., if ϵ is lower than a given threshold), we decide to use the genetic algorithm combined with the steepest ascent procedure to re-estimate the whole parameter vector θ. To this end, each of the L ($L = 35$) parameters θ_l is quantified on 8 bits in order to take any value within the range $[\theta_l - \delta\theta_l, \theta_l + \delta\theta_l]$ with θ_l the estimated parameter value given at the previous time. Tests have shown that the tracking procedure provides often good initializations from one frame to the next, avoiding resorting to the GA optimization. Nevertheless, this GA-based stochastic minimization procedure remains necessary to recover the good shape if the inter-frame motion is important. In this tracking process, gradient ascent technique takes about ten seconds and GA-based optimization takes about one minute on a standard Sun/Sparc2 workstation.

	Initialization		
$\Phi^{[0]}_{y_{(e_0)}}$	$0.50_{(\pi)}$	$00_{(min)}$	$150_{(\sigma^2)}$
$\Phi^{[0]}_{y_{(e_1)}}$	$0.50_{(\pi)}$	$00_{(min)}$	$10000_{(\alpha^2)}$
	ICE procedure		
$\Phi^{\text{final}}_{y_{(e_0)}}$	$0.09_{(\pi)}$	$19_{(min)}$	$672_{(\alpha^2)}$
$\Phi^{\text{final}}_{y_{(e_1)}}$	$0.91_{(\pi)}$	$19_{(min)}$	$2037_{(\alpha^2)}$
	Real parameters		
$\Phi^{\text{real}}_{y_{(e_0)}}$	$0.09_{(\pi)}$	$19_{(min)}$	$700_{(\alpha^2)}$
$\Phi^{\text{real}}_{y_{(e_1)}}$	$0.91_{(\pi)}$	$19_{(min)}$	$2000_{(\alpha^2)}$

TAB. **2.2. Estimated parameters for the picture reported in Figure 2.12. π stands for the proportion of the two classes within the synthetic image. min and α are the Rayleigh law parameters. From top to bottom (a) Initialization of the ICE procedure. (b) Estimated parameters by the ICE procedure. (c) Real parameters.**

Figure 2.16 shows the tracking of the endocardial contour in a medical echographic image (each frame size is 256×256) at different time frames during the cardiac cycle. Figure 2.17 shows two other detection/segmentation obtained with our procedure on real ultrasound images. The best resulting template is drawn on a rectangular grid to visualize the global non-affine deformation estimated by the hybrid GA. The global prior model seems to be flexible enough for representing accurately the inherent natural variability of the endocardial contour during the cardiac cycle.

Figure 2.18.a shows the best resulting templates obtained on the twenty first frames of the image sequence reported in Figure 2.16. The mean shape is computed from this set of deformed templates (see Figure 2.18.a). We can notice that this mean shape is not too different from the proposed circular original template γ_0.

2.8 Conclusion

In this paper, we have developed a robust algorithm to detect and track anatomical deformable structures like the endocardial border in an ultrasound image. We have stated the segmentation and tracking issues in the Bayesian framework and take into account all the available *a priori* knowledge of this problem. First, the proposed global prior model, integrating an original prototype template along with predefined global and local deformations, has shown itself to be very flexible and well suited to model the high variability of the endocardial contour over long image sequence. Another important source of *a priori* knowledge is information about the intensity and texture of the tissue of different anatomical structures. These factors are highly dependent on the imaging process and are taken into consideration by modeling the speckle distribution of each class of the ultrasound image by a Rayleigh law. Parameters of each PDF are given by a preliminary Markovian estimation step and are then exploited in the data likelihood model in order to statistically segment the image. The proposed method can be easily generalized with multidimensional pixel value and/or regions parameterized with a distribution mixture and presents several attractive features compared to other related approaches. In particular, it seems to be well suited to handle ultrasound images with strong speckle noise on which edge information or some gradient measures cannot be exploited. Finally, we have shown that this problem can be handled as an equivalent energy minimization problem for each image of the echographic sequence. To this end, the considered optimization problem is tackled using a genetic exploration combined with a steepest ascent procedure. This combined local and

global optimization procedure is fast, robust, simple and well suited for our application compared to other optimization techniques such as gradient-based method or the simulated annealing algorithm [16]. Besides, this method do not require initialization of the template close to the desired solution. Initialization may be defined at random, leading to segmentation procedure that are completely data driven. This method has been applied to a long ultrasound image sequence; the obtained results demonstrate its efficiency and robustness.

Acknowledgments

The author thanks **INRIA** (Institut National de la Recherche en Informatique et Automatique, France) for financial support of this work (postdoctoral grant).

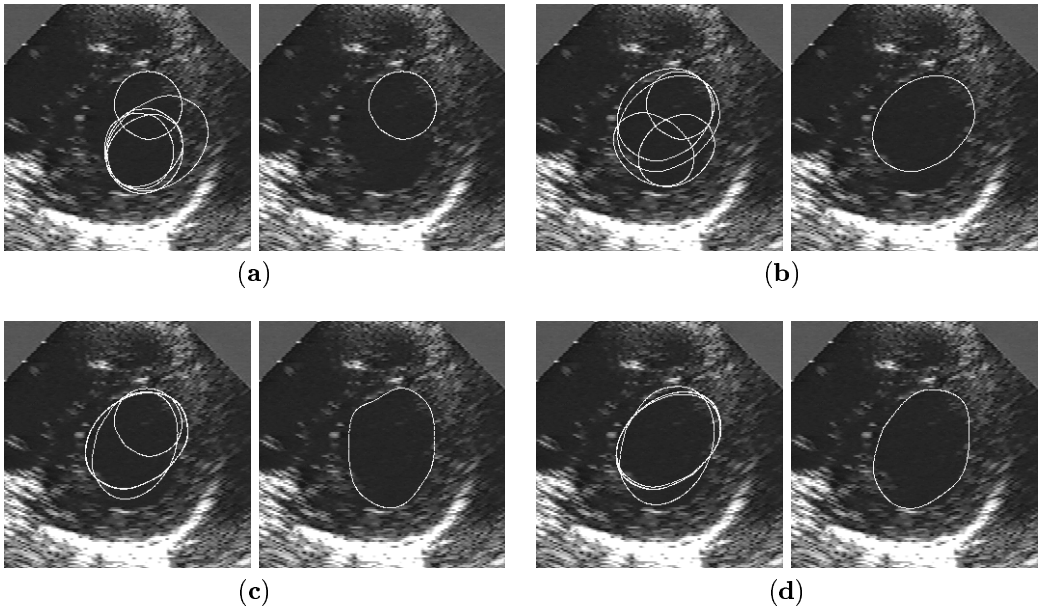

FIG. **2.10. Successive generations of the genetic search on an ultrasound image showing the endocardium (first frame of the sequence). Best 5 % deformed templates before the gradient ascent procedure (on the left) and the best resulting template (on the right). Hybrid GA optimization after : (a) 2 generations** $(\mathcal{F}(\epsilon(\theta, y)) = 0.091)$. **(b) 3 generations** $(\mathcal{F}(\epsilon(\theta, y)) = 0.119)$. **(c) 4 generations** $(\mathcal{F}(\epsilon(\theta, y)) = 0.173)$. **(d) 8 generations** $(\mathcal{F}(\epsilon(\theta, y)) = 0.186)$. **An accurate and reliable detection of the endocardial border is obtained.**

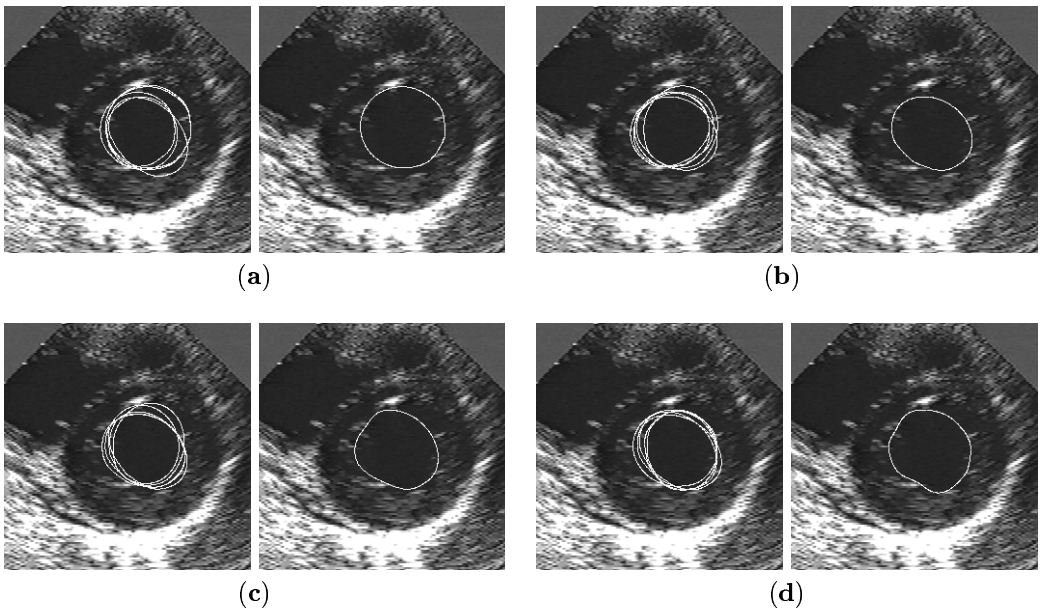

FIG. **2.11. Successive generations of the genetic search on an ultrasound image showing the endocardium (frame** 38**). Best** 5 **% deformed templates before the gradient ascent procedure (on the left) and the best resulting template (on the right). Hybrid GA optimization after : (a) 0 generation (initial population of the GA)** $(\mathcal{F}(\epsilon(\theta, y)) = 0.100)$**. (b) 2 generations** $(\mathcal{F}(\epsilon(\theta, y)) = 0.123)$**. (c) 4 generations** $(\mathcal{F}(\epsilon(\theta, y)) = 0.155)$**. (d) 8 generations** $(\mathcal{F}(\epsilon(\theta, y)) = 0.157)$**. An accurate and reliable detection of the endocardial border is obtained.**

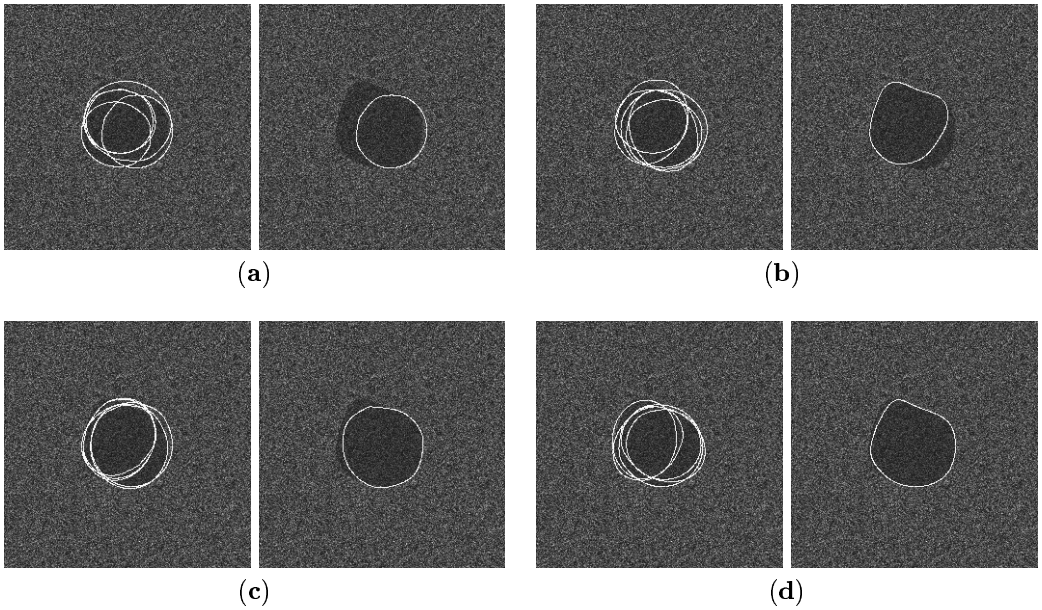

FIG. 2.12. **Successive generations of the genetic search on an synthetic image with synthetic Rayleigh noise. Best 5 % deformed templates before the gradient ascent procedure (on the left) and the best resulting template (on the right). Hybrid GA optimization after : (a) 2 generations** $(\mathcal{F}(\epsilon(\theta, y)) = 0.149)$. **(b) 4 generations** $(\mathcal{F}(\epsilon(\theta, y)) = 0.166)$. **(c) 6 generations** $(\mathcal{F}(\epsilon(\theta, y)) = 0.167)$. **(d) 10 generations** $(\mathcal{F}(\epsilon(\theta, y)) = 0.174)$. **An accurate and reliable detection and segmentation is obtained and can be compared to the ground truth segmentation reported in Figure 2.14.**

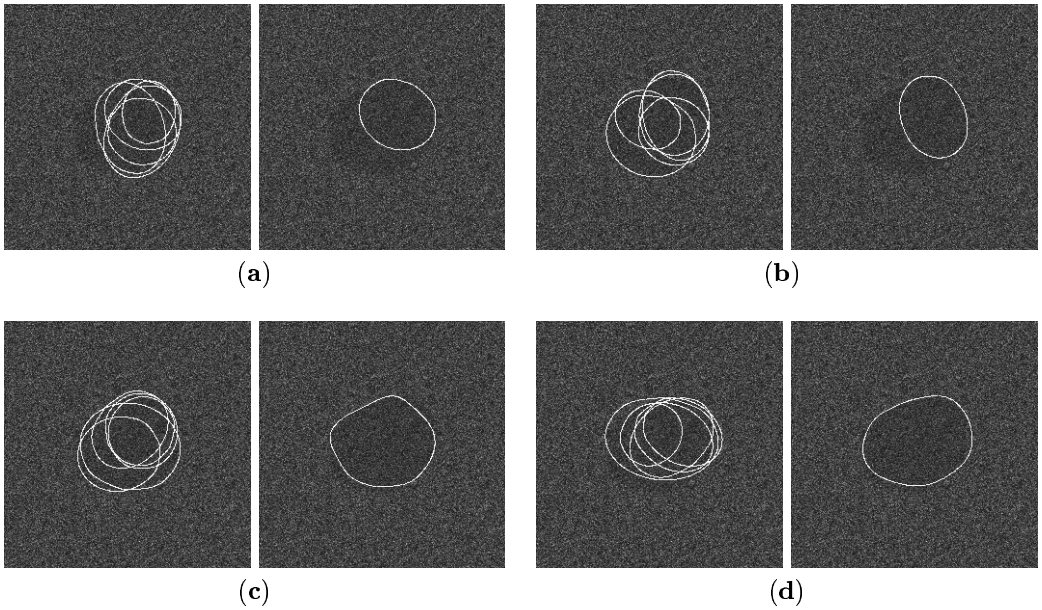

FIG. **2.13. Successive generations of the genetic search on an synthetic image with synthetic Rayleigh noise. Best** 5 **% deformed templates before the gradient ascent (on the left) and the best resulting template (on the right). hybrid GA optimization after : (a) 2 generation** $(\mathcal{F}(\epsilon(\theta, y)) = 0.116)$**. (b) 4 generations** $(\mathcal{F}(\epsilon(\theta, y)) = 0.118)$**. (c) 10 generations** $(\mathcal{F}(\epsilon(\theta, y)) = 0.119)$**. (d) 24 generations** $(\mathcal{F}(\epsilon(\theta, y)) = 0.120)$**. An accurate and reliable detection and segmentation is obtained and can be compared to the ground truth segmentation reported in Figure 2.14.**

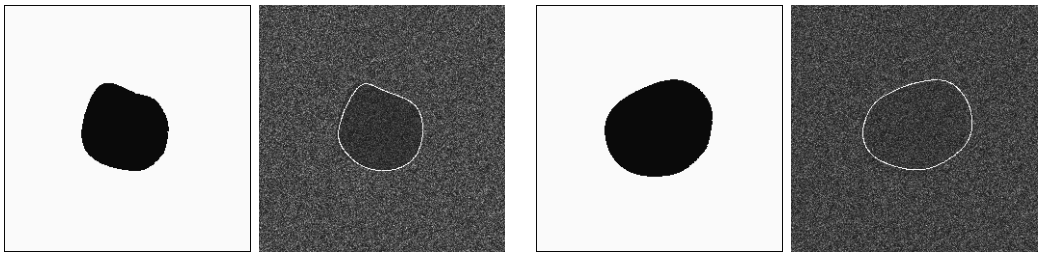

(a) (b)

FIG. 2.14. **Ground truth segmentation (on the left) and segmentation results obtained with our segmentation method (on the right). (a) Synthetic image presented in Figure 2.12. (b) Synthetic image presented in Figure 2.13.**

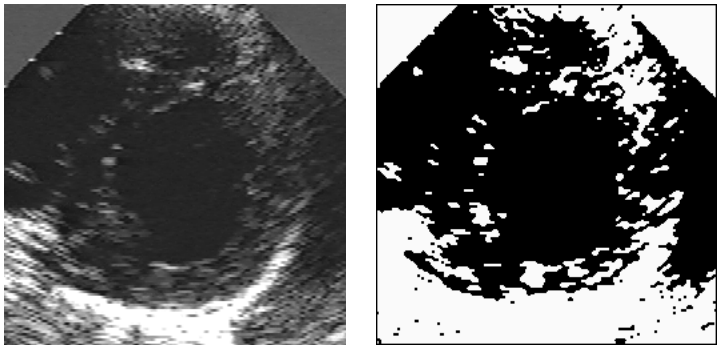

(a) (b)

FIG. 2.15. **Unsupervised Markovian segmentation of an ultrasound image using the single scale determinstc relaxation technique called ICM and based on the parameters estimated by the ICE procedure. (a) Real ultrasound image. (b) Two-class Markovian segmentation. The resulting semented map exhibits unproper *blood* or *muscle* areas due to the strong speckle noise present on this image.**

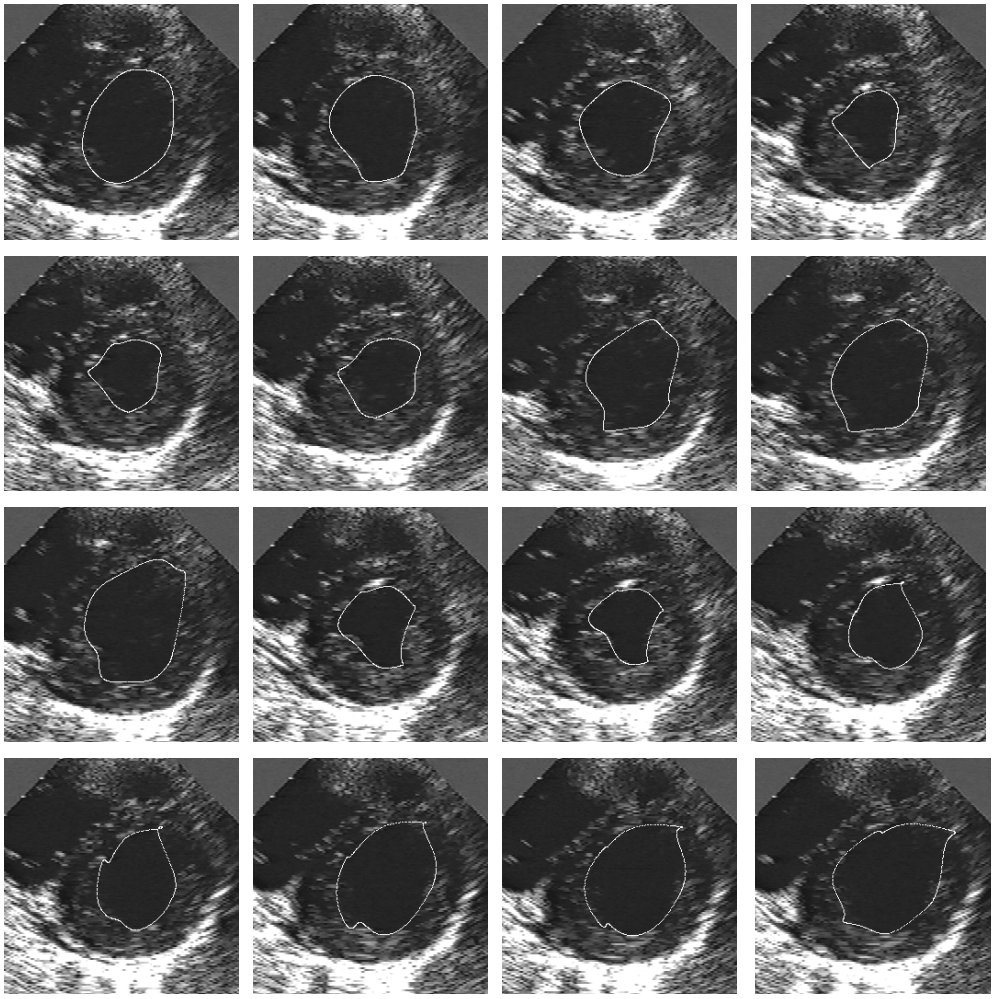

FIG. **2.16. Tracking of the endocardial contour in a medical echographic sequence at different time frames during the cardiac cycle. From top left to bottom right : frame 1, 4, 6, 9, 12, 13, 18, 20, 27, 34, 35, 40, 41, 44, 46, 48.**

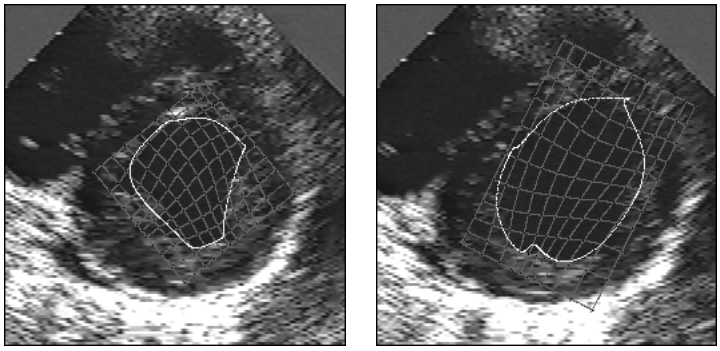

(a) (b)

FIG. 2.17. **Detection/Segmentation obtained with our procedure on real ultrasound images. The best resulting template is drawn on a rectangular grid to visualize the global non-affine transformation estimated by the GA. (a) frame 33. (b) frame 45.**

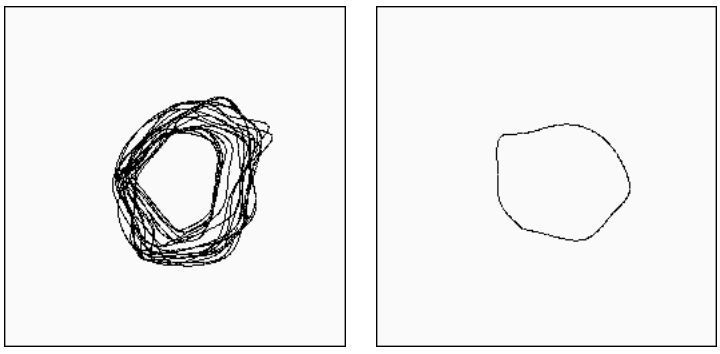

(a) (b)

FIG. 2.18. **Set of deformed templates and mean shape. (a) Best resulting templates obtained on the 20 first frames of the image sequence reported in Figure 2.16. (b) Mean shape computed from this set of deformed templates.**

Chapter 3

AN UNSUPERVISED MULTISCALE APPROACH FOR THE DYNAMIC CONTOUR-BASED BOUNDARY DETECTION ISSUE IN ULTRASOUND IMAGERY

This work has been submitted to the International Conference *IEEE Conputer Vision, Pattern Recognition and Image Processing*, Atlantic city, USA, march 2000 [C3] in a shorter version than the one presented in this chapter.

3.1 Abstract

We present a new multiscale approach for deformable contour optimization. The method relies on a multigrid minimization method and a coarse-to-fine relaxation algorithm. This approach consists in minimizing a cascade of optimization problems of reduced complexity. Contrary to classical multi-resolution algorithms, no reduction of image is applied. The family of defined energy functions are derived from the original (full resolution) objective function, ensuring that the same function is handled at each scale and that the energy decreases at each step of the minimization process. The efficiency and the speed of this multiscale approach is demonstrated in the difficult context of the boundary detection of anatomical structures in ultrasound imagery.

3.2 Introduction

Segmentation remains a necessary step in medical imaging to obtain qualitative measurements such as the location of objects of interest as well as for quantitative measurements such as area, volume or the analysis of dynamic behavior of anatomical structures over time. Among these images, ultrasound images play a crucial role, because they can be produced at video-rate and therefore allow a dynamic analysis of moving structures. Moreover, the acquisition of these images is non-invasive, cheap, and does not require radiations compared to other medical imaging techniques. On the other hand, the automatic segmentation of anatomical structures in ultrasound imagery is a real challenge due to speckle noise and artifacts which are inherent in these images. These artifacts create open contour and/or ill defined boundaries, making ineffective algorithms such as Markov Random Field-based classical segmentation technique [4].

Among the existing segmentation techniques, the active contour models, or so-called *snakes* [24], are an effective way to overcome these artifacts and to rightly model the fact that the object to be detected is assumed to be connected. Besides, their ability to efficiently combine both the available *a priori* knowledge about the structure of interest (generally a smoothness constraint) and local correspondances with the image features (such as the grey level statistical distribution inside and outside the object), makes them very attractive for the segmentation tasks in ultrasound imagery. Nevertheless, this modeling finally requires to solve an intricate energy function minimization problem. The configuration space of this optimization problem is generally *very large* and the resulting energy function may exhibit many local *minima*, especially when the image contains strong noise,

which is frequently the case in ultrasound imagery. In order to cope with this optimization problem, gradient-based methods have originally been proposed [24]. The main drawback of these techniques is to require a proper initialization of the initial contour not *too far* from the expected boundary, otherwise they will converge towards bad local *minima*. Dynamic Programming [1] solves the optimality problem, although at the expense of a very high computational load. In order to shorten execution times, researchers have recently suggested to combine gradient or DP-based methods with a multi-resolution framework. Nevertheless, the optimal solution is no more guaranteed. Besides, the construction of the "multi-resolution pyramid" results in losing some important information that our energy function is sensitive to.

In order to overcome this problem, we propose herein to extend to our optimization problem, the multiscale strategy combined with the multi-resolution framework introduced in [20] for the estimation of the optical flow in an image sequence. The key idea of this strategy consists in minimizing the global energy function through an appropriate hierarchy of subspaces of the whole configuration space. These subspaces contain constrained configurations describing the expected solution at different scales. In our application, these solutions are modeled as being the optimal positions of a sequence of dynamic contour models, of decreasing thickness, whose energy function is derived from the original energy function. This constrained optimization is implemented using a coarse-to-fine procedure on a pyramidal structure. This method has shown to be very robust for optimizing a highly non-linear objective function and has turned out to provide quickly a good estimate very close to the global *minima* [20].

This paper is organized as follows : Section 3.3 presents the dynamic contour model used in our application and the resulting energy function to be optimized. The multiscale minimization strategy adapted to our problem is described in Section 3.4. In Section 3.5, we report some experimental results on synthetic and real ultrasound images. Finally, Section 3.6 contains concluding remarks.

3.3 The active contour model

The active contour model (or *snake*), introduced by Kass *et al.* in [24], formulates the boundary detection issue as an energy function minimization problem. Formally, an active contour V is simply defined by an ordered set of n nodes, $V = [v_1, v_2, \ldots, v_n]$, giving coordinates of points on the contour in a circular manner. A cubic B-spline curve involving these n control points (or a simple straight line between each node) allows to completely define this model. Given an input image y, its energy function is generally given by :

$$E_{\text{snake}}(V) = \sum_{i=1}^{n} \big(E_{\text{int}}(v_i) + \beta E_{\text{ext}}(v_i, y) \big) \tag{3.1}$$

where β is a weighting parameter. E_{int} and E_{ext} are the internal and external energy terms respectively, also called the constraint forces, of the contour element v_i. These two energy terms play different roles in the energy minimization process. The internal energy allows to express the available *a priori* knowledge about the contour shape to be detected whereas the external energy allows to pull the snake towards the desired image features [24] (such as edges, regions, textures, etc.). The definition of these energy terms have to be carefully defined according to the application and the input image. Let us finally add that the use of such global energy-based models fall into the Bayesian framework [48].

In order to model our *a priori* knowledge on the smoothness of the anatomical shape boundary to be detected, a commonly used solution consists in measuring the curvature at each node of the contour [50] and then in using this measure as the internal energy term :

$$E_{\text{int}}(v_i) = \arccos\left(\frac{\overrightarrow{v_{i-1}v_i} \cdot \overrightarrow{v_iv_{i+1}}}{\|\overrightarrow{v_{i-1}v_i}\| \cdot \|\overrightarrow{v_iv_{i+1}}\|}\right) \tag{3.2}$$

that is the angle between the two vectors $\overrightarrow{v_{i-1}v_i}$ and $\overrightarrow{v_iv_{i+1}}$. $\|\overrightarrow{v}\|$ is the norm of the vector $\overrightarrow{v}$ and " $\cdot$ " represents the dot product between two vectors. In the minimization process, this *a priori* energy term penalizes high curvature on the contour.

In a commonly used active contour model-based segmentation approach, spatial gradient measures derived from the input image, are generally exploited in the external energy term [48]. In our application, due to the speckle noise and artifacts which are inherent to ultrasound images, our external energy term cannot rely efficiently on this type of measure. An alternative model consist in exploiting the statistical distribution of the grey levels inside and outside the boundary of the object to be detected [39]. Let $y = \{y_s \in S\}$, the set of pixels of the image located on a lattice S of M sites s. Assuming one Probability Density Function (PDF), $P_{\text{in}}(.)$, for the pixels inside the object and another PDF, $P_{\text{out}}(.)$, for the pixels outside the object, we can then define the following external energy term by :

$$E_{\text{ext}}(v_i, y) = -\frac{1}{N_{\text{in}}} \sum_{s \in v_i^{\text{in}}} \ln P_{\text{in}}(y_s) - \frac{1}{N_{\text{out}}} \sum_{s \in v_i^{\text{out}}} \ln P_{\text{out}}(y_s) \tag{3.3}$$

where y_s designates the grey level of the pixel at site s. The summation of the first and second term of E_{ext} is over all the N_{in} and N_{out} selected points belonging to the straight segment perpendicular to the contour at node v_i, passing through this point, and respectively located inside and outside the contour, as shown in Fig. 3.1. This likelihood term is minimal when the snake delineates two homogeneous regions, at node v_i, distributed according to the grey level statistical distribution corresponding to each region.

Using these two energy terms, the optimal contour, V_{opt}, can then be obtained by finding the one that minimizes the energy $E_{\text{snake}}(V)$:

$$V_{\text{opt}} = \arg\min_{v} E_{\text{snake}}(V) \tag{3.4}$$

Unfortunately, minimizing such a global energy function is often an intricate problem : the space of possible contours Ω is generally *very large* and the energy function may exhibit many local *minima*, especially when the image contains strong noise, which is our case in ultrasound imagery (see Section 3.5).

In [24] and in many other works, gradient-based methods are used for the energy minimization of this energy function type. These methods are simple but have the disadvantage to require a proper initialization of the dynamic contour not *too far* from the expected boundary, otherwise they will converge toward bad local *minima*. In order to overcome this problem, stochastic methods based on Simulated Annealing (SA) [48] have then been proposed. These ones have the capability of avoiding local *minima* and consequently no human interaction is required to initialize the contour model. However, one of the major drawbacks of these procedures is their very high computational load.

Various deterministic algorithms based on Dynamic Programming (DP) or variational methods [1] have then been constructed for finding the optimal (minimum energy) contour in a neighborhood of the initial contour. If this neighborhood, also called the search window, is too small and an unproper initialization of the initial contour is given, a local sub-optimal solution is then found. Nevertheless, if this search window is large enough, the optimal contour is then guaranteed, although at the expense of a significant increase of the computational complexity.

In order to shorten execution times for practical applications, researchers have recently suggested to combine DP algorithm with a multi-resolution framework [15]. The main idea in using a multi-resolution method is to allow to reduce the number of candidates in the search window, so that the research process gets faster. Deformable contour optimization algorithm is applied to the coarser resolution level and the obtained solution is used as the initial snake position for the next lower level. The process continues until the contour is optimized at the original image level. This procedure noticeably shorten the computational time. Nevertheless, the optimal solution is no more guaranteed. Besides, the construction of different resolution levels, usually obtained by low-pass filtering the data, results in losing some important information that our external energy term is sensitive to. In our case, this low pass-filter would change the nature and the parameter of the different PDFs exploited in the external energy term (Eq. (3.3)). It is even more true if the PDFs are not Gaussian, which is our case (see Section 3.5). At coarser levels, the optimization algorithm will converge towards a biased solution. The same problem remains valid for external energies using edges or textures. In these cases, the information used by the external energy can be altered or simply destroyed.

In order to overcome this problem, we propose to extend the discrete multi-scale relaxation strategy combined with the multi-resolution framework introduced by Heitz *et al* in [20] for the minimization of our global energy function and also for all type of energy function associated to a dynamic contour. We consider this in the next Section.

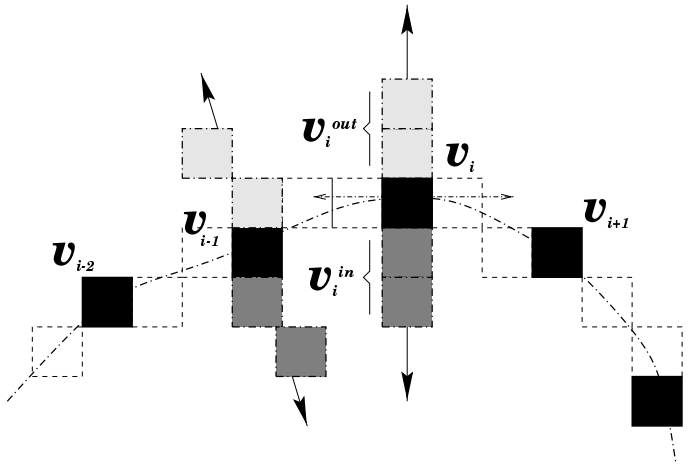

FIG. **3.1. Portion of a contour model showing five connected nodes and the set of points v_i^{in} and v_i^{out} used in the external energy term. $N_{\text{in}} = N_{\text{out}} = 2$ in this example.**

3.4 Multiscale minimization strategy

Instead of minimizing our global energy function directly on the full configuration space Ω, i.e., the space of possible contours, the optimization is led through a sequence of constrained configuration subspaces of increasing sizes :

$$\dim(\Omega^L) < \dim(\Omega^{L-1}) < \ldots < \dim(\Omega^0)$$

with $\Omega^0 \equiv \Omega$ and where Ω^l, $l = 0, \ldots, L$, designates the constrained configuration space at level l. At this resolution level, we define V^l as a rough estimate of the contour model, defined by a ordered set of n_l nodes, $V^l = [v_{b_1^l}, v_{b_2^l}, \ldots, v_{b_{n_l}^l}]$ (with $V^0 \equiv V$ and $v_{b_i^0} \equiv v_i$), giving coordinates of points of this crude contour. Each point (or node) of this contour is indexed on a grid S^l which results from the reduction of S ($\equiv S^0$) by 2^l in each direction and is associated to the block of pixels $b_s^l \subset S$ of size $2^l \times 2^l$, "descendant" of node $v_{b_s^l}$ (see Fig. 3.2).

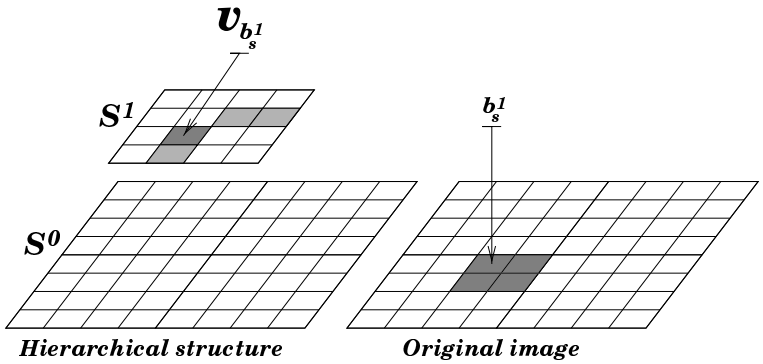

FIG. **3.2. Hierarchical structure ($L=1$ in this example) involved in the multiscale minimization strategy and block of pixels b_s^l associated to the node $v_{b_s^l}$.**

The constrained optimization in Ω^l of our original boundary detection problem is then equivalent to the minimization of the new energy function :

$$E_{\text{snake}}(V^l) = \sum_{i=1}^{n_l} \Big(E_{\text{int}}(v_{b_i^l}) + \beta_l \, E_{\text{ext}}(v_{b_i^l}, y) \Big)$$

Using a multigrid approach [20], we can easily defined $E_{\text{ext}}(v_{b_i^l}, y)$:

$$E_{\text{ext}}(v_{b_i^l}, y) = -\frac{1}{N_{\text{in}}} \sum_{s \in v_{b_i^l}^{\text{in}}} \sum_{p \in b_s^l} \ln P_{\text{in}}(y_p) - \frac{1}{N_{\text{out}}} \sum_{s \in v_{b_i^l}^{\text{out}}} \sum_{p \in b_s^l} \ln P_{\text{out}}(y_p)$$

The definition of $E_{\text{int}}(v_{b_i^l})$ remains similar to the one given in Eq. (3.2). However, one has to keep in mind that the angle between the two vectors has to be estimated on the reduced grid S^l. In addition, due to the size of each node at level l, we have $\beta = 4^l \beta_l$. From this family of energy

functions, we are now able to define our minimization scheme as a cascade (from $l = L$ to $l = 0$) of optimization problems of reduced complexity :

$$V^l_{\text{opt}} = \arg\min E_{\text{snake}}(V^l), \qquad l = L, \ldots, 0.$$

These optimization problems are solved using a standard "coarse-to-fine" multigrid strategy. Starting from a coarse scale L, the optimization problem is first solved in Ω^L. This defines a first (crude) solution to the original problem and the obtained solution, a rough contour, is then used as the initial snake position for the next lower level. This process continues until the contour is optimized at the original image level (see Fig. 3.3). Contrary to standard multi-resolution approaches, no reduction of image data is applied. The family of defined energy functions uses the original image, ensuring that the same energy function (or more precisely, different smoothed versions of this energy function) is handled at each scale, and that the energy decreases at each step of the minimization process. This method has shown to exhibit fast convergence property and robustness against local *minima* for highly non-linear combinational problem [20].

Each of the associated energy minimization problems can be efficiently solved with a standard deterministic optimization algorithm, such as a classical gradient-based method or a DP algorithm requiring a small search window. In our application, we use simply the following iterative technique : for each node $v_{b^l_i}$ of the contour, we compute $E_{\text{snake}}(V^l)$ for the current position of the node and for the two consecutive points belonging to the perpendicular of the contour at the current node, respectively located inside and outside the contour. At a given iteration, and for each node, we accept the position of the contour that minimizes $E_{\text{snake}}(V^l)$ and this process is iterated until there is no change in the shape of the contour between two iterations.

In our case, once the optimization problem at level l is solved, the initial snake position for the next lower level (level $l-1$) is then obtained by keeping the descendant (among four) of each node ensuring the minimal external energy (see Fig. 3.3).

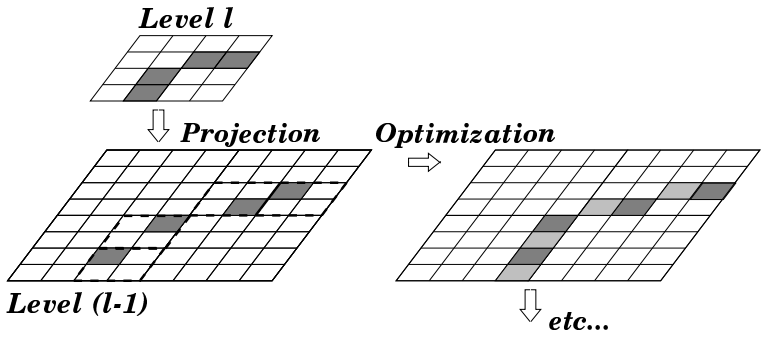

FIG. **3.3. "Coarse-to-fine" minimization strategy.**

Finally, in order to initialize the model at the coarsest level $l = L$, we exploit the result of a two-class segmentation result achieved in a Maximum Likelihood (ML) sense on the coarsest grid S^L. To this end, let $x^L = \{x^L_s, s \in S^L\}$, the set of labels associated to each block of pixels b^L_s. Each x^L_s can take two labels $\{e_{\text{in}}, e_{\text{out}}\}$, associated to the two homogeneous regions and distributed according to the conditional distribution $P_{\text{in}}(y_s)$ and $P_{\text{out}}(y_s)$. This ML blocky segmentation is given by :

	ECI Procedure		
Φ_{in}	$0.48_{(\pi)}$	$24_{(min)}$	$207_{(\alpha^2)}$
Φ_{out}	$0.52_{(\pi)}$	$24_{(min)}$	$9436_{(\alpha^2)}$

TAB. **3.1. Estimated parameters for the ultrasound image reported in Fig.3.5 π stands for the proportion of the two classes within the image. min and α are the shifted Rayleigh law parameters.**

$$\forall\, s \in S^L,\ \hat{x}_s^L = e_{\text{in}} \quad \text{if} \quad \sum_{p \in b_s^l} \ln P_{\text{in}}(y_p) > \sum_{p \in b_s^l} \ln P_{\text{out}}(y_p)$$
$$\text{else} \quad \hat{x}_s^L = e_{\text{out}}$$

This blocky segmentation is then high-pass filtered in order to extract the initial crude contour that will be used for the initialization of the optimization procedure at the coarsest level (see Section 3.5 and upper left of the Fig. 3.5a).

3.5 Experimental results

In order to take into account the speckle noise phenomenon [18] in the reverberation areas, we model the conditional PDFs $P_{\text{in}}(.)$ and $P_{\text{out}}(.)$ of each homogeneous region of the input ultrasound image by a shifted Rayleigh law with different parameters $\Phi = (min, \alpha)$:

$$\mathcal{R}_Y(y; min, \alpha) = \frac{y_s - min}{\alpha^2} \exp\left(-\frac{(y_s - min)^2}{2\alpha^2}\right)$$

with $y > min$ and $\alpha > 0$. The first region arises from the low acoustic wave reverberation in the different cavity of anatomical structures, generally filled with blood. The second region is due to the acoustic signal reverberation on the different organs (cardiac muscles for an echographic image, or wall of arteries for an echobrachial image). In our application, the parameter of these distribution laws are given by a preliminary statistical estimation method called Iterative Conditional Estimation (ICE) [39]. Fig. 3.4 represents the distribution mixture estimated on the echogram shown in Fig. 3.5 and the histogram of this ultrasound image : the two site-wise likelihoods are superimposed to the image histogram. Corresponding estimates obtained by the ICE procedure are given in Table 3.1.

We have validated our multiscale detection method on real echographic and echobrachial images, in order to detect the endocardial contour or the inner wall of an artery respectively. For the experiments, we have chosen $\beta = 1$ for the weighting factor penalizing the internal energy with respect to the external energy and $L = 4$ for the number of resolution levels. The size of these acoustic pictures is 256×256 pixels (256 grey levels).

Fig. 3.5a (at upper left) shows the ML blocky segmentation at the coarsest resolution level $l = L$ that is used to extract the initial crude endocardial contour. Figs. 3.5[b-f] show the resulting estimated snakes at different resolution levels. Fig. 3.6 and 3.7 present the segmentation results obtained on other echographic images and on three echobrachial images respectively. Finally, Fig.

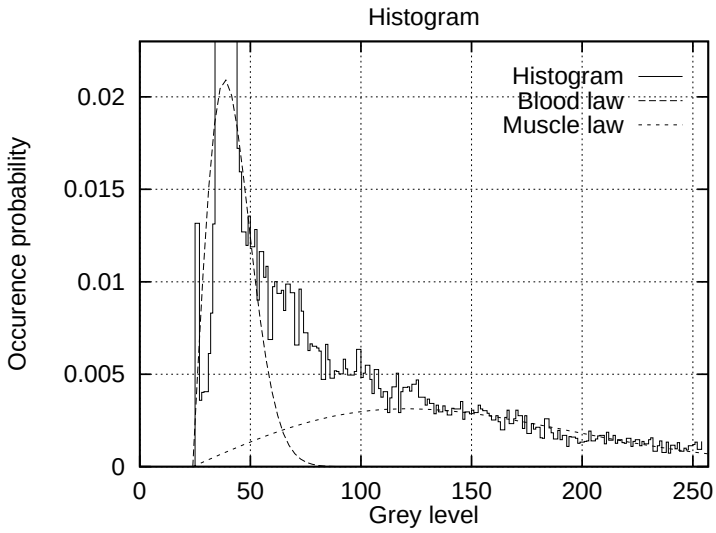

FIG. **3.4. Image histogram of the ultrasound image reported in Fig. 3.5 (solid curve) and estimated PDF mixture obtained with the ICE procedure (dashed and dotted curves).**

3.8 shows a synthetic image presenting an object on a background with a strong synthetic speckle noise and the resulting segmentation obtained by our method.

We can notice (cf. Figure 3.5a) that the ML blocky segmentation maps exhibits unproper *blood* or *muscle* areas at lower levels (higher resolution levels) of the pyramidal structure due to artifacts created by the ultrasound imagery process. The boundary of the endocardial contour cannot be efficiently extracted on these lower levels. Nevertheless, a closed (but crude) contour can be efficiently extracted at the highest level of the pyramidal structure. We can notice (see Figs. 3.5[a-f]) that the proposed multiscale strategy allows efficiently to obtain a good initial guess at each level that is refined at the finer scales. A reliable detection of the endocardial contour or of the inner wall of an artery is obtained. The proposed boundary segmentation procedure is very fast and takes about 3–4 seconds (average CPU time) on a standard Sun/Sparc 2 workstation that makes this procedure compatible with a practical application.

3.6 Conclusion

In this paper, we have developed a robust algorithm to detect the boundaries of anatomical structures, like the endocardial contour or the inner wall of arteries, in ultrasound images. We have stated this detection problem in the active contour model framework and we have taken into account the inherent smoothness of these structures and the grey level statistical distribution inside and outside the boundary of the object to be detected. We have finally presented a multiscale framework for the minimization of the global energy function resulting of this modeling. The minimization is efficiently performed through a multigrid algorithm which consists in imposing successively weaker and weaker constraints on the searched estimate. In our application, this procedure results in estimating successively the optimal position of contour models of decreasing thickness. This framework can be

easily generalized to edge or texture-based energy-minimizing contour model as well as for three-dimensional boundary detection. This scheme is fast, exhibits good convergence properties, and is well suited to automatic extraction of anatomical structure boundaries in ultrasound imagery.

Acknowledgments

The author thanks **INRIA** (Institut National de la Recherche en Informatique et Automatique, France) for financial support of this work (postdoctoral grant).

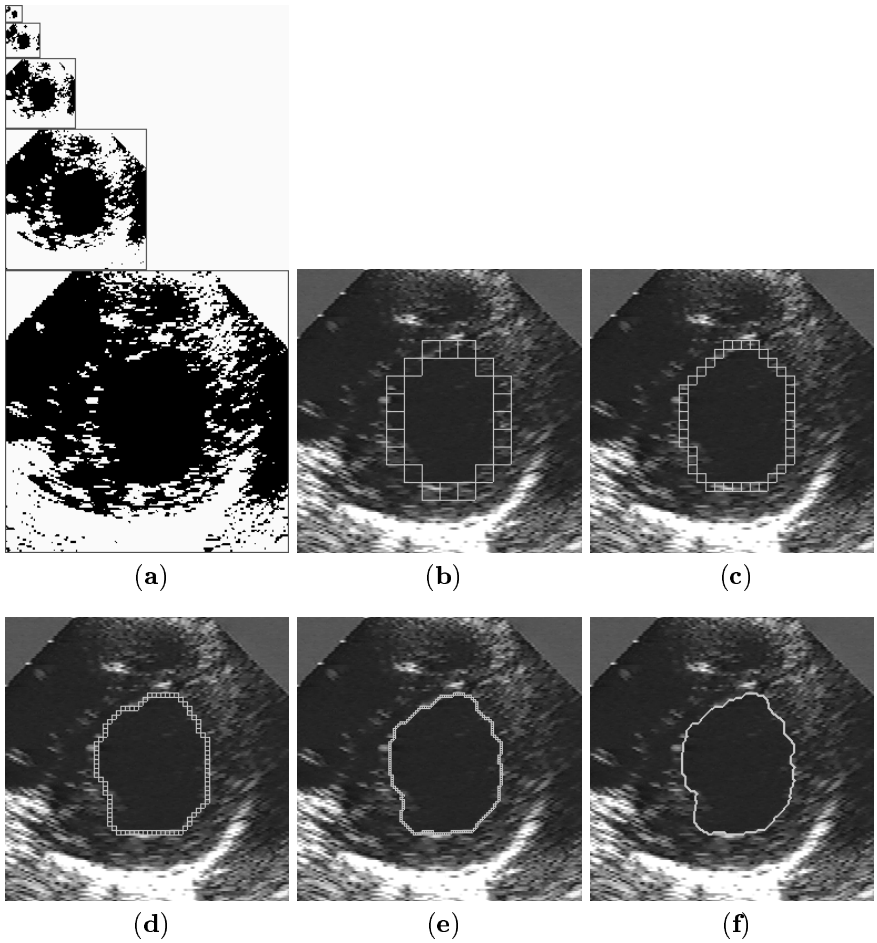

FIG. **3.5. (a) ML blocky segmentation at different resolution levels and estimated snakes at different resolution levels (b-f).**

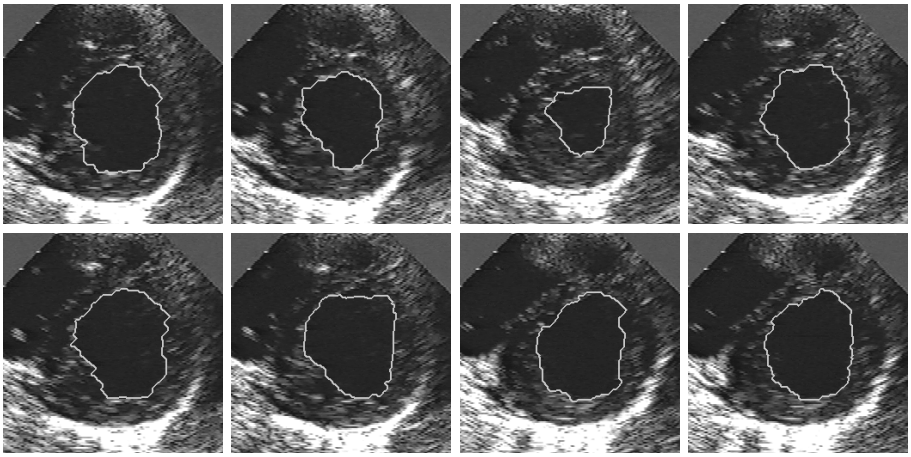

FIG. 3.6. **Detection of the endocardial contour at different time frames during the cardiac cycle.**

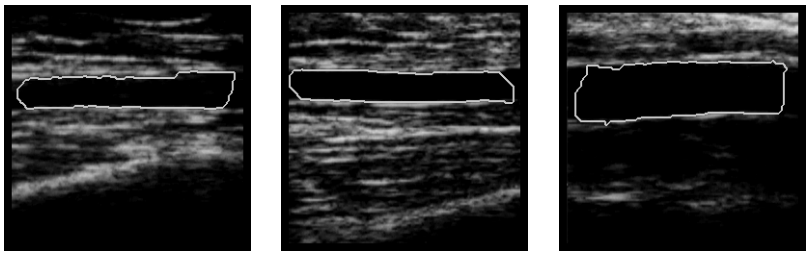

FIG. 3.7. **Detection of the inner wall of an artery on echobrachial images.**

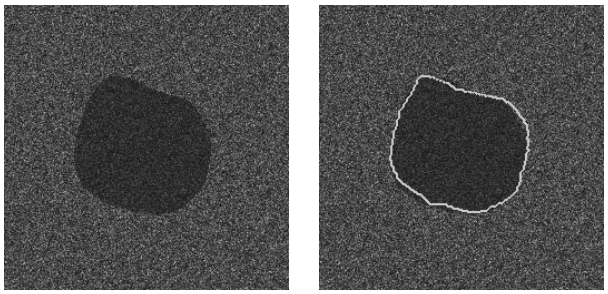

FIG. 3.8. **Synthetic ultrasound image showing an object lying on a background with strong speckle noise and the resulting segmentation obtained by our method.**

Chapter 4

A COMPARISON OF SUPERVISED AND BLIND DECONVOLUTION TECHNIQUES APPLIED IN SPECT IMAGERY

This work has been submitted to the workshop SPIE Conference on Medical Imaging, San Diego, California, USA, Feb. 00, in a shorter version [C2].

4.1 Abstract

Thanks to its ability to yield functionally rather than anatomically-based information, the SPECT imagery technique has become a great help in the diagnostic of cerebrovascular diseases which are the third most common cause of death in the USA and Europe. Nevertheless, SPECT images are very blurred and consequently their interpretation is difficult. In order to improve the spatial resolution of these images and then to facilitate their interpretation by the clinician, we propose to implement and to compare the effectiveness of different existing "blind" or "supervised" deconvolution methods. To this end, we present an accurate distribution mixture parameter estimation procedure which takes into account the diversity of the laws in the distribution mixture of a SPECT image. In our application, parameters of this distribution mixture are efficiently exploited in order to prevent overfitting of the noisy data for the iterative deconvolution techniques without regularization term, or to determine the exact support of the object to be restored when this one is needed. Recent blind deconvolution techniques such as the NAS-RIF algorithm [28], combined with this estimation procedure, can be efficiently applied in SPECT imagery and yield promising results.

Keywords : *SPECT imagery, blind deconvolution, distribution mixture estimation, Markov Random Field model, image restoration.*

4.2 Introduction

SPECT (Single Photon Emission Computed Tomography) images are obtained by the measure of radiations (gamma rays) coming from radioactive isotopes injected in the human body. Contrary to other medical imaging techniques, such as X-ray, CT (Computer Tomography), MRI (Magnetic Resonance Imaging), etc., this imagery process is able to give functionally rather than anatomically-based information, such as the metabolic behavior of organs (like the human brain), by measuring and visualizing the level of blood flow. This study of regional Cerebral Blood Flow (rCBF) can aid in the diagnostic of cerebrovascular diseases and brain disorders (e.g., Alzheimer's disease, Parkinson's disease, etc.) by indicating lower, or abnormal higher, metabolic activity in some brain regions.

Due to the peculiar imaging process, SPECT suffers from poor statistics and poor spatial resolution. Poor statistics result from the small number of photons that can be acquired for each image; principally owing to the low sensitivity of the collimator and the low dose of the injected radiopharmaceutical. Factors influencing the spatial resolution are mainly the scattering of the emitted photons and, to a lesser degree, the intrinsic resolution of the camera. Consequently, resulting

cross-sectional SPECT images are very blurred and their interpretation by the nuclear physician is often difficult, labor-intensive and subjective. If the object to be visualized is small compared to the source-to-collimator distance, this degradation phenomenon may be considered to be shift-invariant and, neglecting noise, this one can be modeled by a convolution process between the true undistorted image and the transfer function of the imaging system [6]. A body of theoretical and experimental work has led to approximate this transfer function (also called the Point Spread Function or PSF) by a two-dimensional symmetric Gaussian function [32], [11]. In order to improve the spatial resolution of SPECT images, some authors have thus investigated the SPECT image deblurring problem with this class of Gaussian transfer function and by using classical Wiener filter techniques [6], [32] or supervised maximum entropy filter-based deconvolution technique [49]. This restoration procedure, also called a deconvolution procedure, is an important consideration in SPECT medical imaging where there may be localized singularities or cold/hot spots in the true image, associated with lesions or tumors. These localized singularities may not be visible in the blurred image, owing to the diffusive effects associated with the convolution process, which averages out differences in neighboring values. A deconvolution scheme could then be very useful in order to detect such singularities by improving the spatial resolution of SPECT images.

Under the assumption that the blur operation is exactly known, many iterative methods have been proposed by the image processing community for tackling this deconvolution procedure and for facing the usual difficulties related to this ill-posed problem. Amongst the existing methods, some of them are structured in the context of regularization problem to make the inversion well behaved [25], [41], [2], [51]. Others are unregularized and require a termination criteria in order to stop the iterative procedure at the point where there is a balance between the fit to the image data and the amplification of the noise, inherent to this ill-posed inverse problem [30], [31], [21], [8], [5]. Nevertheless, let us note that these supervised deconvolution methods remain limited and sensitive to the assumption made on the nature of the blurring function. Theoretically, the PSF can be measured directly from the SPECT camera by visualizing the blurred result of a point source against a uniform background, but such experiment is generally difficult to obtain in practice and does not necessarily yield a reliable PSF. In applications such as medical imaging, when little is known about the PSF, it can turn out often more relevant to estimate directly the PSF from the observed input image. This problem of simultaneously estimating the PSF (or its inverse) and restoring an unknown image is called "blind deconvolution" or "deconvolution with blur identification". Recent techniques exist and can be used in the SPECT imagery context.

In this paper, we propose a comparative study of existing blind or supervised deconvolution methods. We discuss and compare their respective effectiveness for improving the spatial resolution of real brain SPECT images. We first briefly review classical supervised deconvolution methods which assumes the blur is exactly known *a priori* and, in this context, we exploit the two-dimensional Gaussian assumption for the PSF proposed by some authors [6], [32], [11]. For the class of supervised deconvolution technique without regularization term, we present an accurate distribution mixture parameter estimation which takes into account the diversity of the laws in the distribution mixture of a SPECT image. In our application, parameters of this distribution mixture are efficiently exploited in order to find a reliable stopping rule for these iterative methods and then to prevent the amplification of the noise. Then, recent blind deconvolution techniques are briefly presented and tested. We will show that the joint estimation of the image and PSF can lead, for some of them, to better restoration results and also that the Gaussian assumption, proposed by some authors, is only a rough approximation. Finally, for the class of blind deconvolution technique in which the exact support of the object to be recovered is needed, we propose a novel support-finding algorithm exploiting also the parameters of the aforementioned distribution mixture estimation procedure.

This paper is organized as follows. Section 4.3 briefly describes supervised deconvolution methods and recent blind deconvolution techniques that we will compare. In Section 4.4, we detail the distribution mixture parameter estimation procedure. Deconvolution experimental results on phantoms, synthetic and real brain SPECT images are given in Sections 4.5. Finally, conclusion and perspectives are given in Section 4.6.

4.3 Deconvolution

4.3.1 Introduction

In our application, the degradation of a SPECT image can be represented as the result of a convolution of the true image with a blurring function (the PSF) plus an additive term to model the noise from the physical system. If the imaging system is assumed to be linear and shift invariant, the degradation process can then be expressed by the following linear model :

$$g(x,y) = f(x,y) * h(x,y) + n(x,y)$$

where $g(x,y)$ is the degraded or blurred image, $f(x,y)$ is the undistorted true image, $h(x,y)$ is the PSF of the imaging system and $n(x,y)$ is the additive corrupting noise. In this notation, the coordinates (x,y) represent the discrete pixel locations and $*$ is the discrete linear convolution operator.

4.3.2 Supervised deconvolution methods

Assuming that the blurring function $h(x,y)$ is known, the problem is then to determine $f(x,y)$ given the observation $g(x,y)$. This one is generally ill-posed owing to the existence of the additive noise. This means that there is no unique least square solution of minimal norm $\| g(x,y) - f(x,y) * h(x,y) \|^2$. Besides, a small perturbation of the given data produces large deviations in the resulting solution. An appropriate solution may be chosen through proper initialization of the algorithm or by using deterministic prior information about the original image (*via* a regularization term) to make the inversion well behaved. In this way, iterative approaches have been proposed. Their main advantages are there is no need to explicitly implement the inverse of an operator and the process may be monitored as it progresses. Some of them are briefly presented in this Section and are optimal; in the Least Square (LS) sense, under constraints [25] or not [30], in the Maximum Likelihood (ML) sense [31] or in the Maximum A Posteriori (MAP) sense [41], [21].

Van-Cittert's algorithm

Van Cittert [8] proposed the following iterative algorithm :

$$\hat{f}_{k+1}(x,y) = \hat{f}_k(x,y) + \alpha\Big(g(x,y) - h(x,y) * \hat{f}_k(x,y)\Big)$$

where α is a convergence parameter generally set to 1. In this iterative scheme, the estimated image $\hat{f}(x,y)$ is modified at each iteration by adding a term proportional to the residual $r(x,y) = g(x,y) - h(x,y) * \hat{f}_k(x,y)$.

Landweber's algorithm

Another iterative algorithm, proposed by Landweber *et al.* [30], is provided by the minimization of the norm $\| g(x,y) - h(x,y) * \hat{f}_k(x,y) \|^2$ and leads to the following iteration :

$$\hat{f}_{k+1}(x,y) = \hat{f}_k(x,y) + \alpha\, h(-x,-y) * \Big(g(x,y) - h(x,y) * \hat{f}_k(x,y) \Big)$$

This algorithm, also called the one step gradient, leads to simply move the estimate $\hat{f}(x,y)$ iteratively in the negative gradient direction.

RL's algorithm

The Richardson-Lucy's (RL) algorithm [31] is an iterative technique which attempts to maximize the likelihood of the restored image by using the Expectation Maximization algorithm [12] when the image is assumed to come from a Poisson process. This iterative algorithm may be succinctly expressed as :

$$\hat{f}_{k+1}(x,y) = \hat{f}_k(x,y) \left(h(-x,-y) * \frac{g(x,y)}{h(x,y) * \hat{f}_k(x,y)} \right)$$

In this form of notation, the division and the multiplication is done point-by-point.

Tichonov-Miller's algorithm

This algorithm, also called the constrained least squares restoration, consists in choosing the estimate $\hat{f}(x,y)$ that minimizes the following cost function :

$$\hat{f}(x,y) = \arg\min_{f} \Big\{ \| g(x,y) - h(x,y) * \hat{f}(x,y) \|^2 + \alpha \, \| c(x,y) * \hat{f}(x,y) \|^2 \Big\}$$

where the term $c(x,y) * \hat{f}(x,y)$ generally represents a high pass filtered version of the image $\hat{f}(x,y)$. This is essentially a smoothness constraint which suggests that most images are relatively flat with limited high-frequency activity, and thus it is appropriate to minimize the amount of high-pass energy in the restored image. One typical choice for $c(x,y)$ is the 2D Laplacian operator. The minimization of the above equation leads, with the method of successive approximation, proposed in [25], to the following iterative estimation scheme for $\hat{f}(x,y)$:

$$\begin{aligned} \hat{f}_{k+1}(x,y) &= \hat{f}_k(x,y) + \beta \big(g(x,y) * h(-x,-y) - \big(A_h(x,y) + \alpha A_c(x,y) \big) * \hat{f}_k(x,y) \big) \\ \text{with} \qquad \hat{f}_0(x,y) &= \beta \Big(g(x,y) * h(-x,-y) \Big) \end{aligned}$$

$A_h(x,y) = h(x,y) * h(-x,-y)$ and $A_c(x,y)$ is the autocorrelation function of $h(x,y)$ and $c(x,y)$ respectively. α is called the regularization parameter which must be carrefully chosen for reliable restoration. This iteration converges if $0 < \beta < (2/|\lambda_{\max}|)$ where $\lambda_{\max}$ is the largest eigenvalue of the matrix $A_h(x,y) + \alpha A_c(x,y)$.

Super Resolution algorithm

Assuming Poisson photon distribution in the image, then a Bayesian and MAP derivation has been proposed by Hunt *et al.* [21]. This one leads to the following iterative scheme :

$$\hat{f}_{k+1}(x,y) = \hat{f}_k(x,y) \exp\left(\left[\frac{g(x,y)}{h(x,y) * \hat{f}_k(x,y)} - 1.0 \right] * h(x,y) \right)$$

Molina's algorithm

Following the Bayesian paradigm, Molina *et al.* have proposed to incorporate prior information to the RL (Maximum Likelihood) restoration method [41]. In order to model the *a priori* smoothness of the image to be recovered, this one is defined by the following conditional autoregressive model :

$$P_F(\mathbf{f}) \propto \exp\Big(-\frac{1}{2} \alpha \, \mathbf{f}^t (I - \phi N) \mathbf{f} \Big)$$

In this matrix-vector notation, $\mathbf{f}$ is the true image ordered lexicographically by stacking the rows into a vector. α is the unknown regularization parameter, matrix N is such that $N_{ij} = 1$ if cells i and j are spatial neighbors (pixels at distance one) and zero otherwise, and scalar ϕ is just less than 0.25. The term $\mathbf{f}^t(I - \phi N)\mathbf{f}$ represents, in matrix notation, the sum of squares of the values $\mathbf{f}_i$ minus ϕ times the sum of $\mathbf{f}_i \mathbf{f}_j$ for neighboring pixels i and j. Following the RL method, which corresponds to MAP estimation with an uniform image prior, Molina *et al.* obtain the following iterative scheme :

$$\hat{f}_{k+1}(x,y) = \mu_k(x,y) \overline{f}_k(x,y) + \Big(1 - \mu_k(x,y) \Big) \hat{f}_k(x,y) \left(h(-x,-y) * \frac{g(x,y)}{h(x,y) * \hat{f}_k(x,y)} \right)$$

$\mu_k(x,y) = 0$ corresponds to the classical RL restoration method (we recall that, in this form of notation, the division and the multiplication are done point-by-point). $\overline{f}_k(x,y)$ is a filtered version of $f_k(x,y)$ in which each pixel is the average of its four neighbors pixels (pixels at distance one).

4.3.3 Blind deconvolution methods

When little is known about the PSF, a solution for the deblurring problem consists in achieving a blind deconvolution technique. Blind image deconvolution is the simultaneous estimation of the true image and the PSF from the blurred observation. A commonly used method for blind deconvolution is by minimization of an error metric that optimizes the form of the restored image and the PSF (or its inverse) to fit the various constraints on the form of the solution; typically positivity and known support of the object to be recovered. Steepest descent or conjugate gradient method are generally used to achieve optimization [28], [51]. A second method, usually called "grouped coordinate descent", restores the image and the PSF separately in an iterative form. During each cycle either the image or the PSF is held static while the other is updated, generally using one of the standard deconvolution technique [2], [5]. In these methods, that alternate between restoration of the image and PSF, iterations do not necessarily have to use the same restoration algorithm. In this section, we describe briefly four recent blind deconvolution techniques stemming from these two different approaches.

The IBD method

The Iterative Blind Deconvolution (IBD) method, proposed by Ayers and Dainty [2], requires that the image and the PSF be non-negative with known finite support (the support is defined as the smallest rectangle containing the entire object). After a initial guess is made for the true image, the algorithm alternates between the image and Fourier domains, enforcing known constraints in each. The constraints are based upon information available about the image and the PSF. The image domain constraints can be imposed by replacing negative valued pixels within the region of support with zero and non-zero pixels outside the region of support with the background pixel value. The Fourier domain constraint involves a Wiener-like filter for the image and the PSF. This filter allows to efficiently suppress noise amplification resulting from the ill-posed nature of the restoration problem :

$$\begin{aligned} \hat{H}_k(u,v) &= \frac{G(u,v)\,\hat{F}^*_{k-1}(u,v)}{|\,\hat{F}_{k-1}(u,v)\,|^2 + \alpha / |\,\hat{H}_{k-1}(u,v)\,|^2} \\ \hat{F}_k(u,v) &= \frac{G(u,v)\,\hat{H}^*_{k-1}(u,v)}{|\,\hat{H}_{k-1}(u,v)\,|^2 + \alpha / |\,\hat{F}_{k-1}(u,v)\,|^2} \end{aligned}$$

where $H_k(u,v)$, $G(u,v)$ and $F(u,v)$ represent the 2D FFT of the PSF, the original image and the true image respectively. Subscripts denote the iteration number of the algorithm and $(.)^*$ is the complex conjugate of $(.)$. The real constant α represents the energy of the additive noise and must be carefully chosen for reliable restoration. Figure 4.1 gives an overview of this scheme. The algorithm is run for a specified number of iteration, or until the estimates begin to converge. The major drawback of this method is its lack of reliability ; the uniqueness and convergence properties are uncertain and the algorithm is sensitive to the initial image estimate and can exhibit instability.

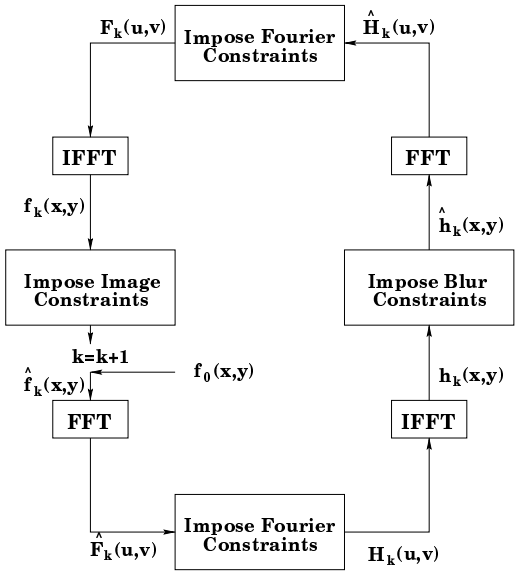

FIG. **4.1. IBD algorithm.**

The Biggs-Lucy's algorithm

This method [5] alternates between restoring the image and the PSF using the RL algorithm (by simply swapping variables $h(x,y)$ and $f(x,y)$ in the RL iteration). The image and the PSF estimates are given by :

$$\begin{aligned}\hat{h}_{k+1}(x,y) &= \frac{1}{\sum \hat{f}_k(x,y)}\,\hat{h}_k(x,y)\left(f_k(-x,-y) * \frac{g(x,y)}{h_k(x,y) * \hat{f}_k(x,y)}\right)\\ \hat{f}_{k+1}(x,y) &= \frac{1}{\sum \hat{h}_{k+1}(x,y)}\,\hat{f}_k(x,y)\left(h_{k+1}(-x,-y) * \frac{g(x,y)}{h_{k+1}(x,y) * \hat{f}_k(x,y)}\right)\end{aligned}$$

This method requires a good initial guess for the PSF and a different number of iterations for the image and the PSF, expressed by an asymmetric factor which is necessary because image and PSF estimates converge at different rates. Depending on the type of the image and the nature of the PSF, this factor is generally different and must be carefully chosen for reliable restoration.

The NAS-RIF algorithm

The Non-negativity and Support constraints Recursive Inverse Filtering (NAS-RIF) technique [28] is applicable to situations in which an object of finite support is imaged against a uniform or noisy background which is our case. It comprises a 2D variable finite impulse response filter $u(x,y)$ of dimension $N_{xu} \times N_{yu}$ with the blurred image pixels $g(x,y)$ as input. The output of this filter represents an estimate of the true image $\hat{f}(x,y)$. This estimate is passed through a nonlinear filter which uses a non-expansive mapping to project the estimated image into the space representing the known characteristics of the true image. The difference between this projected image $\hat{f}_{\text{NL}}(x,y)$ and $\hat{f}(x,y)$ is used as the error signal to update the variable filter $u(x,y)$. Figure 4.2 gives an overview of this scheme. The image is assumed to be non-negative with known support. The cost function used in this restoration procedure is defined as :

$$\begin{aligned}J(\mathbf{u}) &= \sum_{(x,y)\in\mathcal{D}_{\text{sup}}} \hat{f}^2(x,y)\left(\frac{1-\text{sgn}(\hat{f}(x,y))}{2}\right)\\ &+ \sum_{(x,y)\in\overline{\mathcal{D}}_{\text{sup}}}\left(\hat{f}(x,y)-L_{\text{B}}\right)^2 + \gamma\left(\sum_{\forall(x,y)} u(x,y)-1\right)^2\end{aligned}$$

where $\hat{f}(x,y) = g(x,y) * u(x,y)$, and $\text{sgn}(f) = -1$ if $f < 0$ and $\text{sgn}(f) = 1$ if $f \geq 0$. $\mathcal{D}_{\text{sup}}$ is the set of all pixels inside the region of support, and $\overline{\mathcal{D}}_{\text{sup}}$ is the set of all pixels outside the region of support. The variable γ in the third term is nonzero only when L_{B} is zero, i.e., the background color is black. The third term is used to constrain the parameter away from the trivial all-zero global minimum for this situation. Authors have shown that the above equation is convex with respect to $u(x,y)$, so that convergence of the algorithm to the global minimum is ensured using the conjugate gradient minimization routine [28].

The You-Kaveh's algorithm

This method [51] attempts to minimize a cost function consisting of a restoration error measure and two regularization terms, one for the image and the other for the blur :

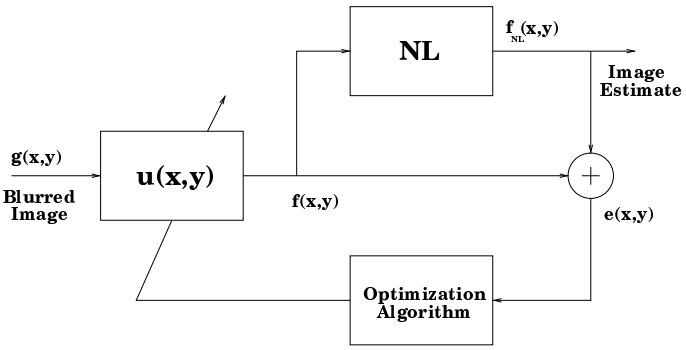

FIG. **4.2. NAS-RIF algorithm.**

$$
\begin{aligned}
C(\hat{f},\hat{h}) &= \arg\min_{f,h}\Big(\frac{1}{2}\parallel g(x,y)-h(x,y)*\hat{f}(x,y)\parallel^2 \\
&+ \frac{1}{2}\lambda\parallel c(x,y)*\hat{f}(x,y)\parallel^2+\frac{1}{2}\gamma\parallel a(x,y)*\hat{h}(x,y)\parallel^2\Big)
\end{aligned}
$$

where $a(x,y)$ and $c(x,y)$ are regularization operator (e.g., a high-pass filter such as the Laplacian). λ and γ are the regularization parameters that control the tradeoff between fidelity to the observation and smoothness of the estimated image and the estimated PSF. In order to take into account the scale problem, inherent to this cost function, an alternating minimization using steepest descent or conjugate gradient method is proposed. Note that, using steepest descent method, resulting iterative procedures are close to the iteration scheme proposed by Landweber (with a regularization term for the blur) for the alternate restoration of the image and the PSF.

4.4 Distribution mixture parameter estimation

4.4.1 Introduction

In this Section, we present an estimation procedure allowing to estimate the grey level statistical distribution associated to each class (also called the noise model) of a SPECT image. We will show also how this information can be exploited in the aforementioned supervised or blind deconvolution methods.

To this end, we consider a couple of random fields $Z=(X,G)$, where $G=\{G_s, s\in S\}$ represents the field of observations located on a lattice S of N sites s (associated to the N pixels of the SPECT image), and $X=\{X_s, s\in S\}$ the label field (related to the N class labels X_s of a segmented SPECT image). Each aforementioned label is associated to a specific brain anatomical tissue; the "CSF" area designates the region that is normally due to the lack of radiations. In this distribution mixture parameter estimation, this region designates the brain region filled with Cerebrospinal Fluid (without blood flow and thus without radiation) and also the area outside the brain region. The "white matter" and "grey matter" (brightest region) are associated to a low and a higher level of blood flow respectively [10]. Each G_s takes its value in $\{0,\ldots,255\}$ (256 grey levels), and each X_s in $\{e_1=\text{"CSF"}, e_2=\text{"white matter"}, e_3=\text{"grey matter"}\}$.

In the following, the parameters in upper case letter designate the random variables whereas the lower case letters represent the realizations of these concerned random variables. In this estimation step, the distribution of (X, G) is defined, firstly, by prior distribution $P_X(x)$, supposed to be Markovian and secondly, by the site-wise conditional likelihoods $P_{G_s/X_s}(g_s/x_s)$ whose shape and parameter $\Phi_{(x_s)}$ depends on the concerned class label x_s (g_s designates the grey level intensity associated to site s). Finally, we assume independence between each random variable G_s given X_s. The observable G is called the "incomplete data", and Z the "complete data".

4.4.2 Estimation of the distribution mixture parameters for the "complete data"

Assuming the segmentation result x is known, the parameters of the grey level statistical distribution associated to each class, can then be easily computed with the ML estimator of the "complete data".

• Experimentations have shown that we can rightly model the statistical grey level distribution in the background or in the CSF area by a exponential law (see [11] and also the left part of the histogram reported in Figure 4.3). This led us to think that the noise in this region is approximately Poissonian with the following statistical grey level distribution :

$$\mathcal{E}_G(g;\alpha) = \frac{1}{\alpha}\exp\left(-\frac{g}{\alpha}\right)$$

with $g > 0$. Let now $G = (G_1, \ldots, G_M)$ be M random variables, independent and identically distributed according to a "single" exponential law $\mathcal{E}_G(g;\alpha)$, and $g = (g_1, \ldots, g_M)$ a realization of G. The ML estimator of α_{ML} for the "complete data" is simply the mean of the sample g [3].

• In order to describe the luminance within the "white matter" and the "grey matter" regions, we model the conditional density function for these regions by two Gaussian laws. This assumption of normality is a reasonable approximation due to the reconstruction physical process used in SPECT imagery in which the grey level of a given pixel, herein considered as a random variable, are sums of many variables and the "central limit theorem" can be applied [3]. The corresponding ML estimator of the "complete data", for a sample g distributed according to a normal law, is defined simply by the empirical mean and the empirical variance.

4.4.3 Estimation of the distribution mixture parameters for the "incomplete data"

When the segmentation result is unknown (i.e, the class label of each pixel is not supposed to be known), the considered problem is more complex. In order to determine $\Phi = (\Phi_{(e_1)}, \Phi_{(e_2)}, \Phi_{(e_3)})$, we use the ICE (Iterative Conditional Estimation) algorithm. This procedure, described in detail in [46] relies on an estimator $\hat{\Phi}(X, G)$ with good asymptotic properties, like the ML estimator, for completely observed data case. When X is unobservable, this procedure starts from an initial parameter vector $\Phi^{[0]}$ (not too far from the optimal one) and generates a sequence of parameter vectors leading to the optimal parameters, in the least square sense, with the following iterative scheme :

$$\Phi^{[p+1]} = \frac{1}{n}\left[\hat{\Phi}(x_{(1)}, g) + \cdots + \hat{\Phi}(x_{(n)}, g)\right]$$

where $x_{(i)}$, with $i = 1, 2, \ldots, n$, , are realizations of X drawn according to the posterior distribution $P_{X/G}(x/g, \Phi^{[p]})$. In order to decrease the computational load, we can take $n = 1$ without altering

the quality of the estimation [7]. Finally, we can use the Gibbs sampler algorithm [16] to simulate realizations of X according to the posterior distribution. For the local *a priori* model of the Gibbs sampler, we adopt an isotropic Potts model with a first order neighborhood [4]. In this model, there are two parameters, called "the clique parameters" denoted β_1, β_2 and associated to the horizontal and vertical binary cliques respectively [1]. Given this *a priori* model, the prior distribution $P_X(x)$ can be written as :

$$P_X(x) = \exp\Big(-\sum_{<s,t>} \beta_{st}(1 - \delta(x_s, x_t))\Big)$$

where summation is taken over all pairs of neighboring sites and $\delta(.)$ is the Kronecker delta function. In order to favor homogeneous regions with no privileged orientation in the Gibbs sampler simulation process, we choose $\beta_{st} = \beta_1 = \beta_2 = 1$. Finally, $\Phi^{[p+1]}$ is computed from $\Phi^{[p]}$ in the following way :

- **Stochastic Step** : using the Gibbs sampler, one realization x is simulated according to the posterior distribution $P_{X/G}(x/g)$, with parameter vector $\Phi^{[p]}$.
- **Estimation Step** : the parameter vector $\Phi^{[p+1]}$ is estimated with the ML estimator of the "complete data" corresponding to each class.
  - If $N_1 = \#\{s \in S : x_s = e_1\}$ is the number of pixels of the "CSF" area, the ML estimator $\hat{\Phi}_{(e_1)}$ of α is given by [3] : $\hat{\alpha}(x, g) = (1/N_1) \sum_{s \in S : x_s = e_1} g_s$.
  - If $N_2 = \#\{s \in S : x_s = e_2\}$ and $N_3 = \#\{s \in S : x_s = e_3\}$ pixels are located in the "white matter" and "grey matter" regions respectively, the corresponding ML estimator of each class is given by the empirical mean and the empirical variance. For instance, for the "white matter" class, we have for $\hat{\Phi}_{(e_2)}$:

$$\hat{\mu}(x, g) = \frac{1}{N_2} \sum_{s \in S : x_s = e_2} g_s \qquad \hat{\sigma}^2(x, g) = \frac{1}{(N_2 - 1)} \sum_{s \in S : x_s = e_2} (g_s - \hat{\mu})^2$$

- Repeat until convergence is achieved; i.e., if $\hat{\Phi}^{[p+1]} \not\approx \hat{\Phi}^{[p]}$, we return to Stochastic Step.

Figure 4.3 represents the estimated distribution mixture of the SPECT image shown in Figure 4.4b The three site-wise likelihoods $P_{G_s/X_s}(g_s/e_k)$, $k = 1, 2, 3$, (weighted by the estimated proportion π_k of each class e_k) are superimposed to the image histogram. Corresponding estimates obtained by the estimation procedure, requiring about ten iterations, are given in Table 4.1.

	ICE Procedure		
$\Phi^{\text{final}}_{(e_1)}$	$0.52_{(\pi)}$	$11_{(\alpha)}$	
$\Phi^{\text{final}}_{(e_2)}$	$0.26_{(\pi)}$	$100_{(\mu)}$	$648_{(\sigma^2)}$
$\Phi^{\text{final}}_{(e_3)}$	$0.22_{(\pi)}$	$172_{(\mu)}$	$383_{(\sigma^2)}$

TAB. **4.1. Estimated parameters for the picture reported in Figure 4.4b. π stands for the proportion of the three classes within the SPECT image. α are the exponential law parameter. μ and σ^2 are the Gaussian law parameters.**

[1] Cliques are subsets of sites which are mutual neighbors [4].

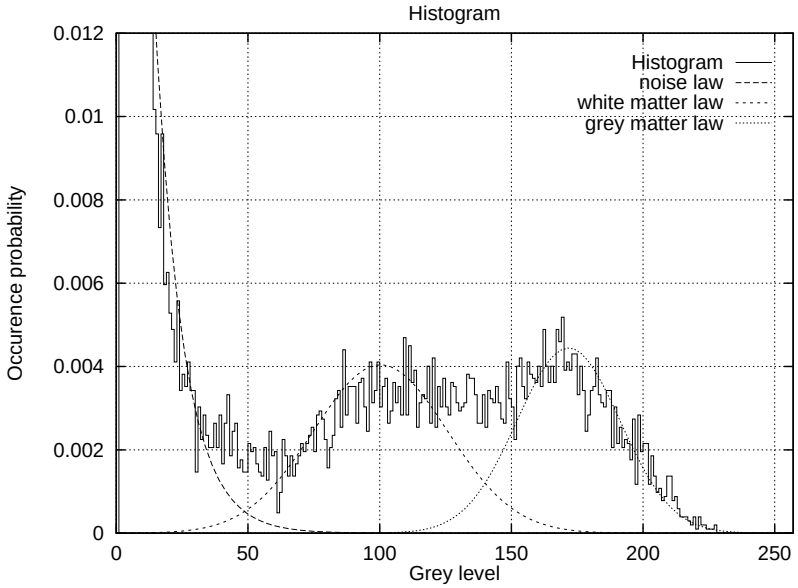

FIG. **4.3. Image histogram of the picture reported in Figure 4.4b (solid curve) and estimated probability density mixture obtained with the ICE procedure (dotted and dashed curves).**

4.4.4 Determination of the support and stopping rule

• In the case of supervised deconvolution techniques without regularization term, such as the Van-Cittert, the Landweber, the RL, and the Super Resolution algorithms, the iterative deconvolution procedure is generally monitored as it progresses and stopped after some iterations, generally by visual inspection. This iteration number may be very different for each SPECT image and is generally related to the behavior of each iterative method near the convergence. In fact, at some point of the iteration procedure, the solution fit more to the noise than the image data. Therefore, for these methods, the process has to be stopped at the point where there is a balance between the fit to the image data and the amplification of noise. To this end, in order to stop automatically these algorithms before the amplification of the noise, we propose to compute the parameters of the distribution mixture of $\hat{f}_k$ regularly, namely every k iterations (k depends on the speed of convergence of the considered deconvolution method). If the parameter associated to the background noise (i.e., α) is above a fixed threshold, we decide to stop the procedure. Of course, this threshold has to be fixed empirically like the iteration number. Nevertheless, contrary to the iteration number, this threshold does not depend of the adopted unregularized method or the speed of convergence of each method as well as the used SPECT images. Besides, it does not require a visual inspection, for each iteration of the deconvolution procedure, that can be cumbersome and unreliable for an automatic deconvolution of a set of SPECT images.

For the supervised deconvolution methods using a regularization term (e.g., the Tichonov-Miller's algorithm), or prior information (e.g., the Molina's algorithm), the termination criteria consists simply in stopping the algorithm when the solution is stable. Nevertheless these methods require a regularization parameter which must be chosen carefully for reliable restoration. This parameter can be also derived efficiently from the proposed noise model estimation procedure.

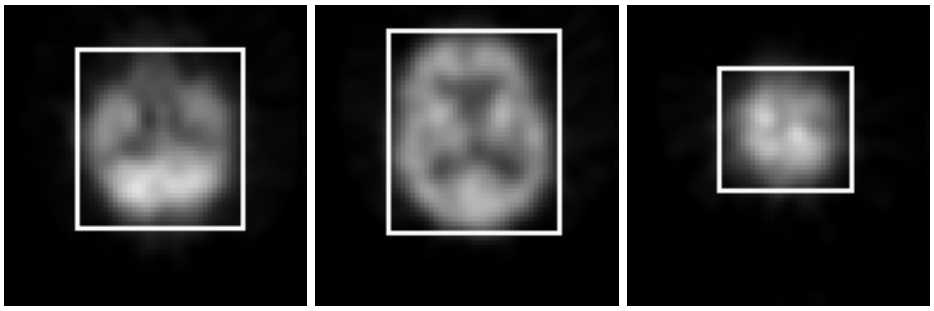

FIG. **4.4. Examples of support determination for some cross-sectional brain SPECT slices.**

• In the case of blind deconvolution techniques, in which the rectangular support of the object to be restored is needed and unknown, we can also efficiently exploit the parameters of the distribution mixture of the input image g by adopting the following strategy ; we assume that the row $\mathcal{R}_i \in S$ contains the object $\mathcal{O}$ to be restored if we can find two consecutive sites $\in \mathcal{R}_i$ for which :

$$P(g_{ij}/''\text{CSF}'') \leq P(g_{ij}/''\text{white matter}'')$$

where the subscripts i, j refer to the pixel located at the i^{th} row and the j^{th} column and g to the luminance. We adopt an identical reasoning for the column and the object support is then accurately determined by the set of pixels g_{ij} which belong to a row $\mathcal{R}_i$ and a column $\mathcal{C}_j$ containing the object $\mathcal{O}$. Figure 4.4 displays examples of rectangular support determination for some cross-sectional brain SPECT images. A more accurate support could be given by an unsupervised Markovian segmentation based on parameters given by the ICE procedure. Finally, let us recall also that for these blind deconvolution techniques, there is no need to implement a stopping rule and convergence is reached when the estimated PSF and image are stable.

4.5 Experimental results

The effectiveness of each deconvolution method was tested on several cross-sectional phantoms, synthetic and real human brain SPECT images of 64×64 pixels size with 256 grey levels. Those presented in this Section are only a few examples.

Except for the Tichonov-Miller's algorithm, the initial estimated image of these iterative schemes is the original input image (i.e., $\hat{f}_0(x,y) = g(x,y)$). Besides, except for the NAS-RIF blind deconvolution technique, the original PSF estimate, *a priori* fixed for the supervised deconvolution methods, is approximated for the real SPECT images by a two-dimensional Gaussian distribution (i.e., $\hat{h}_0(x,y) = \mathcal{G}_{x,y}(\sigma^2)$) with variance $\sigma^2 = 1.5$ (i.e., about 3 pixels of width at half maximum as shown in Figure 4.5). This variance value has been chosen empirically, for each set of deconvolution experiments presented in this Section, in order to obtain the best supervised restoration results. The initial inverse FIR filter required by the NAS-RIF algorithm is simply the Kronecker delta function [28] and we have used $\gamma = 0$ because the background of SPECT images is not completely black. Finally, parameters λ and γ, used in the You & Kaveh's algorithm, are given by the estimation

method proposed by the authors in [51]. In order to objectively compare the spatial resolution improvements and the contrast enhancement between the original and estimated image as well as the resolution improvement of these different restoration approaches, we have stretched the histogram of the estimated image at convergence (i.e., $\hat{f}_{\text{final}}(x,y)$) in order to get the same mean value as the original input image $g(x,y)$.

For the unregularized supervised deconvolution methods, the termination criteria is given by the stopping strategy presented in Section 4.4.4 (see Table 4.2). For the blind deconvolution methods requiring the exact support of the object to be restored, deconvolution results are based on the support-finding algorithm presented in this same Section.

The computational cost for a SPECT image and for each supervised or blind deconvolution procedure is indicated in Table 4.3.

• Figures 4.7 presents examples of brain SPECT image deconvolutions obtained by these different methods. Figure 4.6 displays the PSF estimated by the You-Kaveh's algorithm.

Amongst the supervised deconvolution schemes, the Van-Cittert's method seems to improve slightly the resolution of the original SPECT image. The Landweber's algorithm seems to give quite good results relatively to its implementation simplicity and its low computational complexity. The Tichonov Miller and the Molina's algorithms, which impose *a priori* smoothness of the true image in an effort to control noise, seem to fail to detect all details and singularities of the true undistorted image. In fact, the used prior model seems to be to much simple to model accurately all the property of the true unblurred image. The RL and the Super Resolution algorithms give similar results and allow to improve slightly the spatial resolution of these SPECT images.

Amongst the blind deconvolution techniques, the IBD is unable to converge for 200 iterations and more. The algorithm fails to produce a reliable estimate of the true image for all the presented SPECT images. Deconvolution experiments with the exact rectangular support of the object to be restored, various initial conditions and different noise parameter values α produced poor results as well. The Biggs-Lucy and the You-Kaveh's algorithms seem to give quite good contrast enhancement results but also show undesirable artifacts all around (and maybe inside) the object to be restored. In addition, these techniques remain sensitive to the initial PSF given to the deconvolution procedure. A random initial guess for the PSF or an initial Kroenecker delta function lead to poor results. Let us note that these methods are not ensured to converge to the global *minima* and remain highly sensitive to the initial conditions. Finally, the NAS-RIF technique seems to converge to a good estimate of the solution without *a priori* information or good initial guess about the PSF. Figure 4.8 gives examples of five cross-sectional SPECT image deconvolutions of human brain given by the NAS-RIF algorithm.

• The effectiveness of these deconvolution techniques is also tested on a real SPECT phantom (i.e., a physical plexiglas head phantom filled with radioactive material and measured by a SPECT system) for which the ground truth of this segmented phantom is exactly known and thus for which the performance of each deconvolution method can then be objectively judged. Figure 4.9 presents an example of deconvolution results, on this SPECT phantom, obtained by the different aforementioned deconvolution methods. We can easily notice that this SPECT volume is less noisy and less blurred than the real human brain SPECT slice previously presented and processed (due to several factors such as a different dose of radioactive isotopes contained in each uniform region of this SPECT phantom, a longer acquisition time, the stillness of this simulated brain during the SPECT process, a reduced attenuation, etc.). In order to fully assess the success of this restoration procedure, we use the specific evaluation criteria proposed in [49], based on the estimation of the three following measures :

(i) Firstly, the average contrast of the image, defined by $C = (1 - m_2/m_3)$, where m_2 and m_3 are the mean of the pixel value in the "white matter" and "grey matter" area respectively.

(ii) Secondly, the image mottle M_2 in the "white matter" region, characterized by taking the ratio of the standard deviation σ_2 of pixel values in this area to the mean m_2.

(iii) Thirdly, the image mottle M_3 in the "grey matter" area.

These two last parameters allow to measure the amplification of the noise and/or measure the presence of undesirable artifacts that can be created by the deconvolution procedure in a uniform region of the real SPECT phantom (thus with ideally uniform radioactive activity). Due to the difference of proportion of pixels belonging to each brain anatomical tissue, we consider the total mottle measure given by $M = \rho_2 M_2 + \rho_3 M_3$, with ρ_2 and ρ_3 designates the proportion of pixel belonging to the "white matter" and "gray matter" area respectively. A reliable SPECT image restoration technique will then allow to enhance the contrast of the image with little increase in mottle, i.e., without amplifying too much the noise and/or without creating false artificial features (technically, an increase by a factor of $10\% - 15\%$ of the original mottle of the image remains acceptable if the contrast enhancement is significantly increased [49]). Due to the difference of thickness between the cross-sectional slices of the real and segmented phantom, these abovementioned measures are estimated on the whole 3D phantom after this one has been registered [14] on the ground truth of the segmented phantom volume (see Figure 4.10 where some consecutive slices of the segmented phantom are shown). Table 4.4 gives the contrast and image mottle for each deconvolution technique applied on this SPECT phantom.

Amongst the supervised deconvolution schemes, the Landweber's algorithm allows to increase significantly the contrast of the image but at cost of an unacceptable increase of the mottle of the image (+33.0% of mottle). Deconvolution results, obtained on this SPECT phantom, by the Van-Cittert, the RL, the Tichonov-Miller and the super resolution algorithm are nearly similar; they allow to obtain a good contrast enhancement but also present some artifacts, visible all around the object to be restored. Molina's algorithm gives the best results for this SPECT volume; i.e., a good contrast enhancement with only a little increase of the mottle. Experiments have shown that this method is well suited for cross-sectional SPECT images not too blurred.

Amongst the blind deconvolution techniques, the IBD algorithm fails to produce a reliable estimate of the true image. the You-Kaveh's algorithm allows to increase the contrast of the image but this technique also creates undesirable artifacts and/or an unacceptable amplification of the noise (+30.2% of mottle). Deconvolution result given by the Biggs-Lucy's algorithm is very poor. Finally, the NAS-RIF blind deconvolution technique produce contrast enhancement result as good as the best supervised deconvolution technique (i.e., the Molina's algorithm) along with the slightest increase of the mottle amongst the considered supervised and blind deconvolution techniques. Experiments have shown that this method is well suited both for very blurred SPECT slices and also in the case of less blurred SPECT images.

• Finally, we have also tested the effectiveness of these deconvolution techniques on a cross-sectional slice of a synthetic SPECT volume. In order to simulate at best the typical characteristics of real human brain SPECT images, we have re-created three homogeneous regions and added the corresponding noise for each ones, according to the grey level statistical distribution already estimated on a real human brain SPECT slice (see the distribution mixture presented in Figure 4.3 and parameters given in Table 4.1). We have also added a 3D Gaussian blur in order to simulate the 3D scattering of the emitted photons. Figure 4.11 shows the ground truth of a segmented synthetic slice, the synthetic SPECT slice and finally the deconvolution results obtained by our different restoration methods.

Amongst the supervised deconvolution schemes, the Van-Cittert and the Landweber's algorithm give quite good results although at cost of a slight amplification of the noise in each uniform region of the synthetic SPECT slice. The RL, the Tichonov-Miller and the super resolution algorithm show clearly some artifacts all around the object to be restored. Deconvolution result given by the Molina's algorithm is very poor for this synthetic image; experiments have shown that this method is not well suited for highly blurred image.

Amongst the blind deconvolution techniques, the IBD does not converge. The You-Kaveh and the Biggs-Lucy's algorithm shows clearly false and undesirable artificial features created by the iterative blind deconvolution procedure. Once again, the NAS-RIF technique produces a relative good restoration result.

4.6 Conclusion

In this paper we have shown that a deconvolution procedure noticeably improves the spatial resolution of human brain SPECT images and can be a great help to facilitate their interpretation by the nuclear physician. The proposed distribution mixture estimation procedure allows efficiently to give a reliable termination criteria for the unregularized iterative deconvolution techniques or to accurately determine the exact support of the object to be restored when this one is needed by some blind deconvolution techniques. This estimation procedure is quite general and can be used for other applications such as an unsupervised Markovian segmentation of brain SPECT images into different anatomical tissues, or to give relevant information in order to classify these brain images into different pathology classes. Amongst existing deconvolution techniques, the NAS-RIF algorithm performs better than other deconvolution schemes for SPECT image restoration. This technique can be efficiently combined with our estimation procedure to find the support of the object to be restored and yield very promising results without *a priori* assumption on the nature of the blurring function or for all type of SPECT images (more or less blurred). Finally, let us note also that this method can efficiently be extended in order to take into account the inter-slice blur inherent to this 3D imaging process. This can be done by simply considering a 3D variable FIR filter with a blurred SPECT volume pixels as input. This 3D blind deconvolution NAS-RIF procedure combined with a 3D unsupervised Markovian segmentation procedure, allowing to find accurately the object support to be restored, will be the topic of our next research.

Acknowledgments

The authors thank **INRIA** (Institut National de la Recherche en Informatique et Automatique, France) for financial support of this work (postdoctoral grant). The authors are also grateful to Jean-Paul Soucy and Christian Janicki (CHUM, University of Montréal) for having provided the SPECT images.

Iteration Number					
VC	LW	RL	TM	SR	MO
10	4	200	50	100	10

TAB. **4.2. Iteration number for each supervised deconvolution method as chosen by the proposed stopping rule. Respectively; the Van-Cittert (VC), the Landweber (LW), the Richardson-Lucy (RL), the Super Resolution (SR) and the Molina's (MO) algorithms.**

Computational Cost									
Supervised Methods						Blind Methods			
VC	LW	RL	TM	SR	MO	IBD	BL	NAS-RIF	YK
3	1	18	8	18	2	30	120	129	345

TAB. **4.3. Computational cost for each deconvolution method. Respectively; the Van-Cittert (VC), the Landweber (LW), the Richardson-Lucy (RL), the Super Resolution (SR), the Molina (MO), the IBD, the Biggs-Lucy (BL), the NAS-RIF and finally, the You-Kaveh's (YK) algorithm. Results are obtained on a standard SunSparc 2 workstation and are expressed in seconds.**

	Supervised						Blind			
	VC	LW	RL	TM	SR	MO	IBD	BL	NAS-RIF	YK
ΔC	34.5%	62.0%	35.1%	28.7%	35.1%	28.0%	-6.1%	12.2%	24.7%	29.0%
ΔM	15.3%	33.0%	14.9%	13.5%	14.9%	12.6%	3.8%	13.8%	11.5%	30.2%

TAB. **4.4. Contrast and Image mottle enhancement from the original input image and for each deconvolution method (enhancement expressed in percentage). Respectively; the Van-Cittert (VC), the Landweber (LW), the Richardson-Lucy (RL), the Super Resolution (SR), the Molina (MO), the IBD, the Biggs-Lucy (BL), the NAS-RIF and finally, the You-Kaveh's (YK) algorithm.**

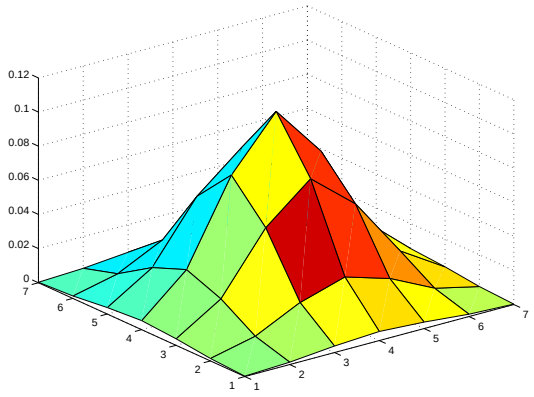

FIG. **4.5. Original PSF defined as a two-dimensional Gaussian distribution with variance $\sigma^2 = 1.5$ in a 7×7 support.**

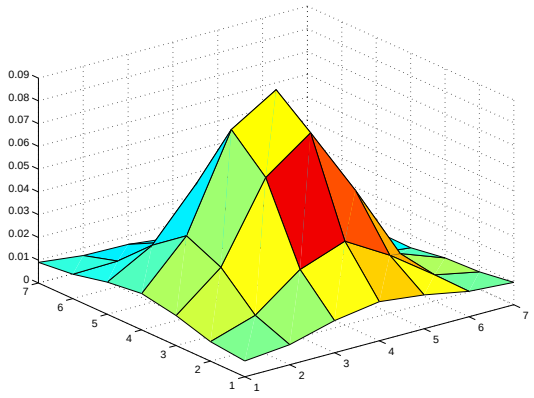

FIG. **4.6. Estimated PSF by the You-Kaveh's algorithm in a 7×7 support.**

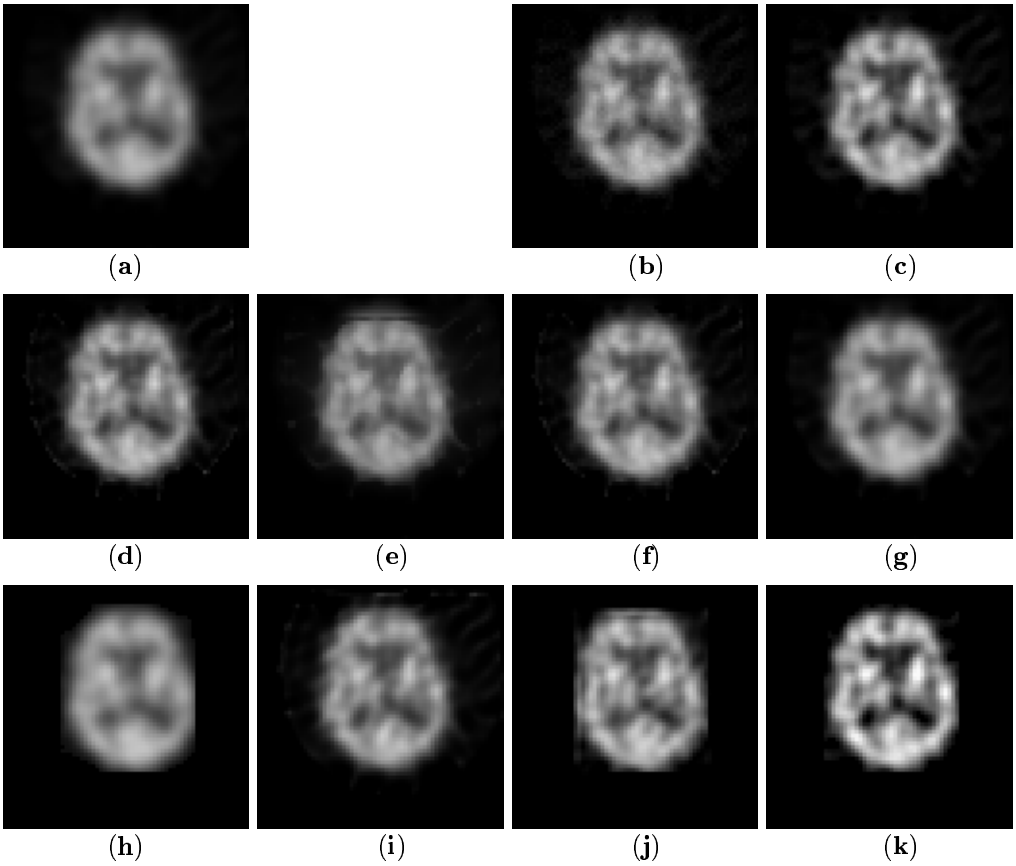

FIG. 4.7. **Examples of brain SPECT image deconvolutions. (a) Original image. (b-g) Supervised deconvolution methods, respectively; (b) Van-Cittert, (c) Landweber, (d) RL, (e) Tichonov-Miller, (f) Super Resolution, (g) Molina's algorithm. (h-k) Blind deconvolution methods, respectively; (h) IBD, (i) Biggs-Lucy, (j) You-Kaveh, (k) NAS-RIF algorithm.**

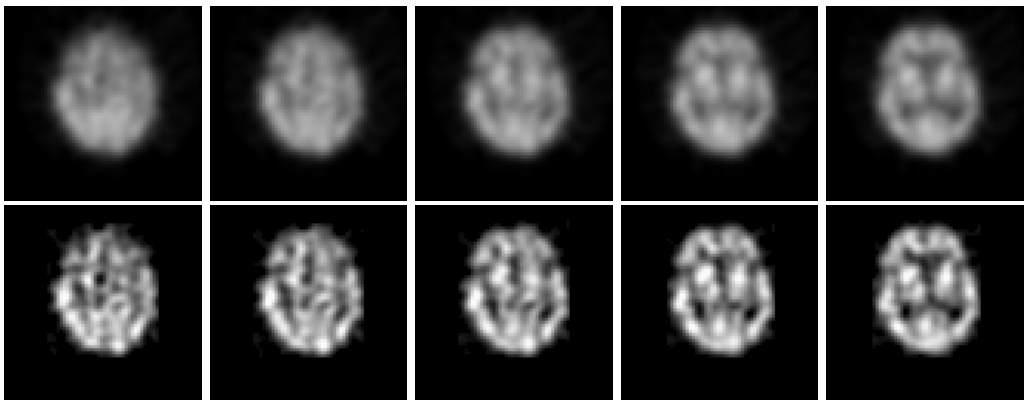

FIG. 4.8. **Examples of human brain cross-sectional SPECT image deconvolutions given by the NAS-RIF algorithm. Top : five consecutive real cross-sectional SPECT slices. Bottom : deconvolution results.**

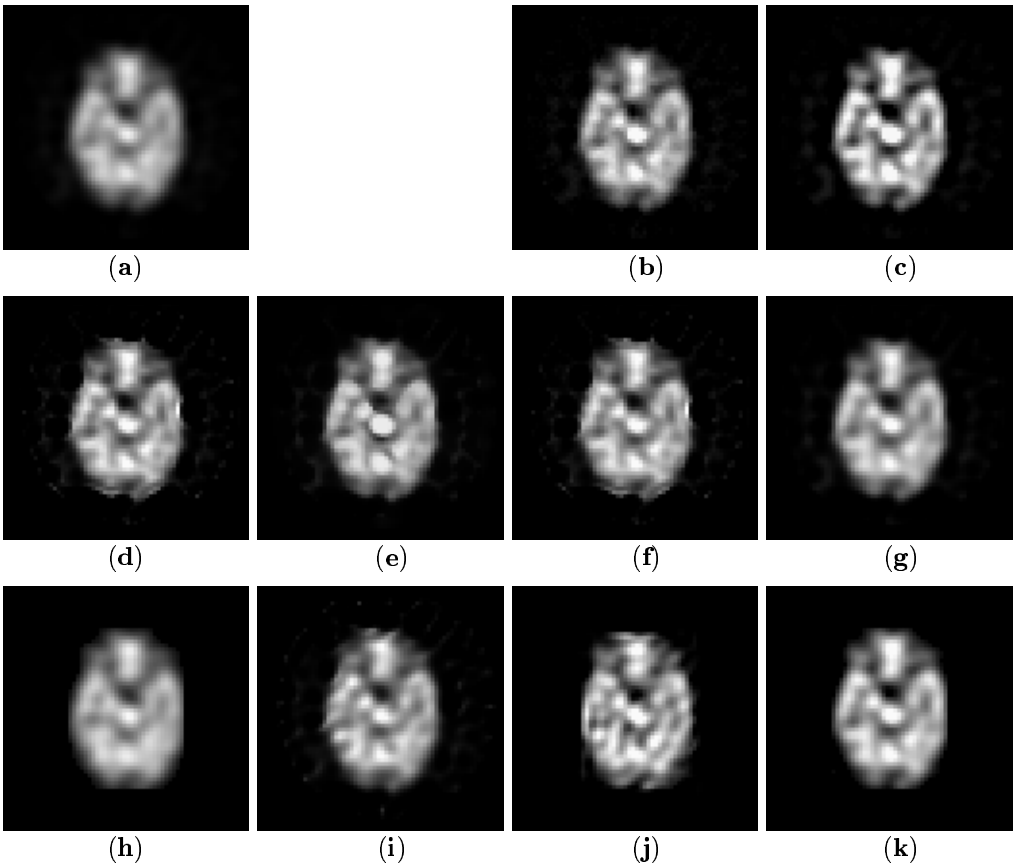

FIG. 4.9. **Examples of phantom SPECT image deconvolutions. (a) Original image. (b-g) Supervised deconvolution methods, respectively; (b) Van-Cittert, (c) Landweber, (d) RL, (e) Tichonov-Miller, (f) Super Resolution, (g) Molina's algorithm. (h-k) Blind deconvolution methods, respectively; (h) IBD, (i) Biggs-Lucy, (j) You-Kaveh, (k) NAS-RIF algorithm.**

FIG. 4.10. **Examples of some consecutive cross-sectional slices of the segmented phantom (ground truth).**

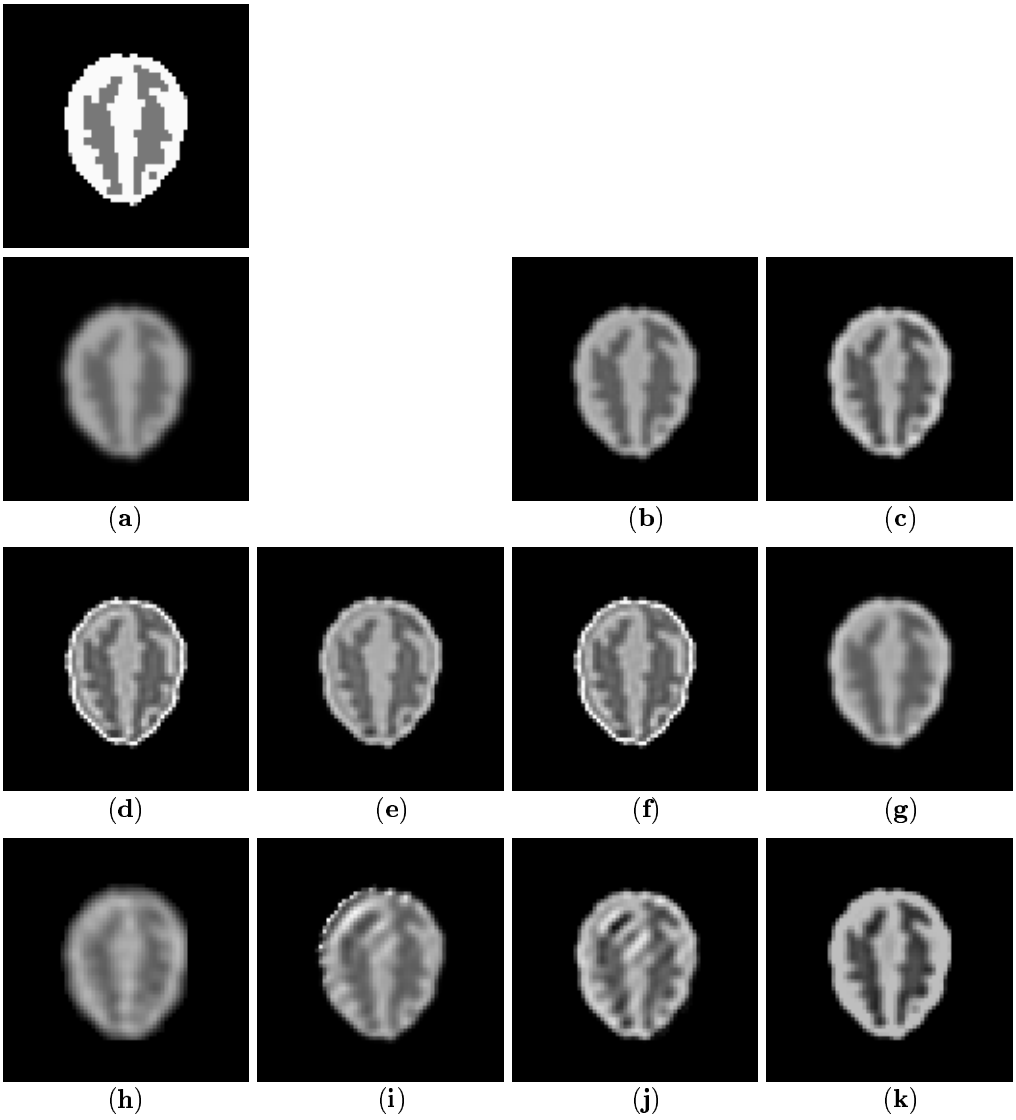

FIG. 4.11. **Examples of phantom SPECT image deconvolutions. (a) Top : ground truth of the segmented synthetic slice. Bottom : synthetic SPECT slice. (b-g) Supervised deconvolution methods, respectively ; (b) Van-Cittert, (c) Landweber, (d) RL, (e) Tichonov-Miller, (f) Super Resolution, (g) Molina's algorithm. (h-k) Blind deconvolution methods, respectively ; (h) IBD, (i) Biggs-Lucy, (j) You-Kaveh, (k) NAS-RIF algorithm.**

Chapter 5

THREE-DIMENSIONAL BLIND DECONVOLUTION OF SPECT IMAGES

This work has been accepted in the original version (presented here) to the review *IEEE. trans on Biomedical Engineering* as a short length paper [R2].

5.1 Abstract

Thanks to its ability to yield functionally rather than anatomically-based information, the three-dimensional (3D) SPECT imagery technique has become a great help in the diagnostic of cerebro-vascular diseases. Nevertheless, due to the imaging process, the 3D SPECT images are very blurred and consequently their interpretation by the clinician is often difficult and subjective. In order to improve the resolution of these 3D images and then to facilitate their interpretation, we propose herein, to extend a recent image blind deconvolution technique (called the NAS-RIF deconvolution method) in order to improve both the spatial and the inter-slice resolution of SPECT volumes. This technique requires a preliminary step in order to find the support of the object to be restored. In this paper, we propose to solve this problem with an unsupervised 3D Markovian segmentation technique. This method has been successfully tested on numerous real and simulated brain SPECT volumes, yielding very promising restoration results.

Keywords : SPECT imagery, 3D blind deconvolution, unsupervised segmentation, Markov Random Field model, image restoration.

5.2 Introduction

3D SPECT (Single Photon Emission Computed Tomography) images are obtained by the detection of radiations (gamma rays) coming from radioactive isotopes injected in the human body. Contrary to other medical imaging techniques, such as X-ray, CT (Computer Tomography), MRI (Magnetic Resonance Imaging), etc., this imagery process is able to give functionally rather than anatomically-based information, such as the 3D metabolic behavior of human brain, by visualizing the level of blood flow of a set of cross-sectional images. This study of regional Cerebral Blood Flow (rCBF) can aid in the diagnostic of cerebrovascular diseases (e.g., Alzheimer's disease, Parkinson's disease, etc.) by indicating lower, or abnormal higher, 3D metabolic activity in some brain regions.

Due to the imaging process, SPECT suffers from poor spatial resolution mainly owing to the 3D scattering of the emitted photons. Consequently, resulting 3D SPECT images are blurred and their interpretation by the nuclear physician is often difficult and subjective. If the object to be visualized is small compared to the source-to-collimator distance, this degradation phenomenon may be considered to be shift-invariant [6] and, neglecting noise, this one can be modeled by a 3D convolution process between the true undistorted 3D image and the transfer function of the imaging system (also called the Point Spread Function or PSF).

In order to improve the spatial resolution of SPECT volumes, some authors have thus investigated the SPECT image deblurring problem by neglecting the inter-slice blur and by approximating this transfer function with a 2D symmetric Gaussian function [32], [11] or by considering an a priori known PSF [49]. In this context, classical Wiener filter techniques [32], [6] or maximum entropy filter-based deconvolution technique [49] have then been proposed to achieve this deconvolution procedure and significant resolution improvements have been noticed [32], [49], [6]. Nevertheless, let us note that these methods don't take into account the inter-slice blur inherent to this 3D SPECT imagery process and are sensitive to the assumption made on the nature of the blurring function. In our applications where little is known about the PSF, it can turn out to be more relevant to estimate directly the PSF from the observed input image. This problem of simultaneously estimating the PSF (or its inverse) and restoring an unknown image is called a "blind deconvolution" problem. Recent 2D deconvolution techniques exist, such as the NAS-RIF algorithm, and can also be efficiently extended in the 3D SPECT imagery context. These techniques require to find, in a preliminary step, the support of the object to be restored. In this paper, we propose to solve this problem thanks to an unsupervised 3D Markovian segmentation technique.

This paper is organized as follows. Section 5.3 briefly describes the proposed 3D extension of the NAS-RIF deconvolution technique. In Section 5.4, we detail the 3D unsupervised Markovian segmentation algorithm allowing to find the exact support of the object to be restored. Deconvolution experimental results on phantoms, synthetic and real brain SPECT volumes and conclusion are given in Section 5.5. Finally, we conclude Section 5.6.

5.3 3D Deconvolution Method

5.3.1 Introduction

In our application, the degradation of a 3D SPECT image (i.e., a SPECT volume) can be represented as the result of a convolution of the true SPECT volume with a 3D blurring function (the PSF), plus an additive term to model the noise from the physical system. If the imaging system is assumed to be linear and shift invariant, this degradation process can then be expressed by the following linear model :

$$g(x,y,z) = f(x,y,z) * h(x,y,z) + n(x,y,z)$$

where $g(x,y,z)$ is the degraded or blurred 3D image, $f(x,y,z)$ is the undistorted true 3D image, $h(x,y,z)$ is the PSF of the imaging system and $n(x,y,z)$ is the corrupting noise (assumed additive in our model). In this notation, the coordinates (x,y) represent the discrete pixel spatial locations, z the slice location and $*$ designates the 3D discrete linear convolution operator. The 3D blind deconvolution problem consists then in determining $f(x,y,z)$ and $h(x,y,z)$ (or its inverse) given the blurred observation $g(x,y,z)$.

When the object to be recovered is imaged against a uniform or a noisy background, a commonly used method for solving the 2D blind deconvolution problem consists in minimizing an error metric that optimizes the form of the restored image and the PSF (or its inverse) to fit the various constraints, *a priori* known, on the form of the solution ; typically positivity and known support of the object. The steepest descent or conjugate gradient method are then generally used to achieve optimization [28], [51] [2]. In our application, the true undistorted rCBF map of a human brain consists of a finite support imaged against a noisy background due to the Poisson noise phenomenon. In this

Section, we propose to find accurately this support thanks to an unsupervised 3D Markovian segmentation technique and then to use a 3D extension of such deconvolution technique for improving both spatial and inter-slice resolution of the SPECT volumes.

5.3.2 3D extension of the NAS-RIF algorithm

In the 3D SPECT imagery context, the recent Non-negativity and Support constraints Recursive Inverse Filtering (NAS-RIF) algorithm [28] can be easily extended in order to take into account both the 2D spatial and the inter-slice blur. We can derive a 3D extension of this technique by simply considering a 3D variable FIR filter $u(x,y,z)$ of dimension $N_{xu} \times N_{yu} \times N_{zu}$ with the blurred SPECT volume pixels $g(x,y,z)$ as input (see Figure 5.1). The output of this filter gives an estimate of each cross-sectional 2D true image $\hat{f}(x,y,z=k)$ (with $k \in [1,K]$ and K representing the number of transversal slices in the considered SPECT volume). Each resulting estimation is passed through a nonlinear filter which uses a non-expansive mapping to project the estimated 2D image into the space representing the known characteristics of the true image. The difference between this projected image $\hat{f}_{\text{NL}}(x,y,z=k)$ and $\hat{f}(x,y,z=k)$ is used as the error signal to update the variable filter $u(x,y,z)$. Figure 5.1 gives an overview of the proposed 3D-extended NAS-RIF deconvolution algorithm. Each cross-sectional 2D image is assumed to be non-negative with known support. The cost function used in the deconvolution procedure of the k^{th} transversal 2D image is defined as :

$$
\begin{aligned}
J_k \;=\; & \sum_{(x,y)\in\mathcal{D}_{[k]}} \hat{f}^2(x,y,z=k)\left(\frac{1-\operatorname{sgn}(\hat{f}(x,y,z=k))}{2}\right) \\
& + \sum_{(x,y)\in\overline{\mathcal{D}}_{[k]}} \left(\hat{f}(x,y) - L_{\text{B}}\right)^2 + \gamma\left(\sum_{\forall(x,y,z)} u(x,y,z) - 1\right)^2
\end{aligned}
$$

where $\hat{f}(x,y,z) = g(x,y,z) * u(x,y,z)$, and $\operatorname{sgn}(f) = -1$ if $f < 0$ and $\operatorname{sgn}(f) = 1$ if $f \geq 0$. $\mathcal{D}_{[k]}$ is the set of all pixels of $g(x,y,z=k)$ inside the region of support, and $\overline{\mathcal{D}}_{[k]}$ is the set of all pixels outside the region of support. The variable γ in the third term is nonzero only when L_{B} is zero, i.e., the background color is black. The third term is used to constrain the parameter away from the trivial all-zero global minimum for this situation. The authors have shown in [28] that the above equation is convex in the 2D case with respect to u. This property remains true in the 3D case so that convergence of the algorithm to the global minimum is ensured using the conjugate gradient minimization routine [28]. Let us note that a fully 3D deconvolution scheme would consist in minimizing directly the cost function $J = \sum_{k=1}^{K} J_k$. Nevertheless let us also notice that J_k and J being convex and the global minimum being ensured in both cases by the conjugate gradient optimization routine, the estimated solution (i.e., the SPECT volume given by minimizing J and the set of SPECT images given by minimizing each cost function J_k) are thus identical.

---

[2] This class of methods has appeared more reliable in the SPECT image 2D deconvolution context than the one called "grouped coordinate descent" that alternates between restoration of the image and PSF (see chapter 4).

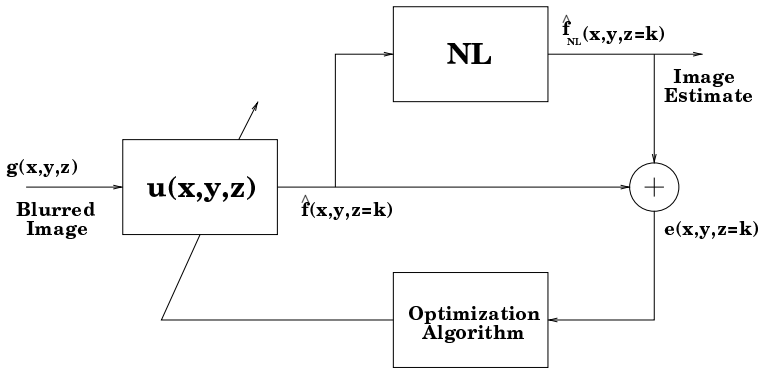

FIG. **5.1. 3D extension of the NAS-RIF deconvolution algorithm.**

5.4 Support determination method

5.4.1 Introduction

In the 2D case, the support can be roughly approximated by the smallest rectangle containing the entire object [28]. In order to automatically determine this rectangular frame, some of the proposed methods are based on hold-out methods [28], or inspired by the constraint assessment algorithm proposed in [44]. These methods are reliable for assessing the optimal 2D rectangular support but cannot be easily extended in order to define a more accurate segmentation.

To this end, an alternative approach consists in exploiting the result of a 3D unsupervised Markovian segmentation. Nevertheless, the problem of "unsupervised" Markovian segmentation is quite complex ; the main difficulty is that the estimation of model parameters is required for the segmentation, while the segmentation result is needed for model parameter estimation. In order to solve this problem, a simple and reliable approach consists in having a two-step process. First, a parameter estimation step in which we have to estimate the MRF model parameter (i.e., the parameters of the grey level statistical distribution associated to each class of the SPECT volume). Then, a second step devoted to the segmentation itself based on the values of the estimated parameters.

5.4.2 3D Unsupervised Markovian segmentation

We consider a couple of random fields $Z = (X, G)$, where $G = \{G_s, s \in S\}$ represents the field of observations located on the 3D lattice S consisting of K lattices S_k of N sites s (associated to the N pixels of each transversal slice of the SPECT volume), and $X = \{X_s, s \in S\}$ the label field (related to the $K \times N$ class labels X_s of a segmented SPECT volume). Each aforementioned label is associated to a specific brain anatomical tissue or region of the SPECT volume ; the "CSF" area designates the region that is normally due to the lack of radiations. In this distribution mixture parameter estimation and segmentation problems, this region designates the brain region filled with Cerebrospinal Fluid (without blood flow and thus without radiation) and also the area outside the brain region. The "white matter" and "grey matter" (brightest region) are associated to a low and a higher level of blood flow respectively [10]. Each G_s takes its value in $\{0, \ldots, 255\}$ (256 grey levels), and each X_s in $\{e_1 =$"CSF", $e_2 =$"white matter", $e_3 =$"grey matter"$\}$.

In the following, the parameters in upper case letter designate the random variables whereas the lower case letters represent the realizations of these concerned random variables. The distribution

of (X, G) is defined, firstly, by prior distribution $P_X(x)$, supposed to be Markovian and secondly, by the site-wise conditional data likelihoods $P_{G_s/X_s}(g_s/x_s)$ whose shape and parameter vector $\Phi_{(x_s)}$ depends on the concerned class label x_s (g_s designates the grey level intensity associated to the site s). In order to take into account the Poisson noise phenomenon inherent to the SPECT imaging process in the "CSF" area, we model $P_{G_s/X_s}(g_s/e_1)$, by a exponential law [11] with parameter α, namely ; $(1/\alpha)\exp[-(g_s/\alpha)]$. To describe the brightness within the "white matter" and the "grey matter" regions, we model the conditional density function for these two regions by two different Gaussian laws [11]. Finally, we assume independence between each random variable G_s given X_s. The observable G is called the "incomplete data" whereas Z constitutes the "complete data".

Estimation Step

In order to determine $\Phi = (\Phi_{(e_1)}, \Phi_{(e_2)}, \Phi_{(e_3)})$, we use the Iterative Conditional Estimation (ICE) algorithm. This estimation procedure [46] relies on an estimator $\hat{\Phi}(X, G)$ for completely observed data case. This iterative method starts from an initial parameter vector $\Phi^{[0]}$ (not too far from the optimal one) and generates a sequence of parameter vectors leading to the optimal parameters (in the least squares sense) with the following iterative scheme :

$$\Phi^{[p+1]} = \frac{1}{n}\left[\hat{\Phi}(x_{(1)}, g) + \cdots + \hat{\Phi}(x_{(n)}, g)\right]$$

where $x_{(i)}, i = 1, \ldots, n$ are realizations of X drawn according to the posterior distribution $P_{X/G}(x/g, \Phi^{[p]})$. In order to decrease the computational load, we can take $n = 1$ without altering the quality of the estimation [7]. Finally, we can use the Gibbs sampler algorithm [16] to simulate realizations of X according to the posterior distribution. For the local *a priori* model of the Gibbs sampler, we adopt a three-dimensional isotropic Potts model with a first order neighborhood [4]. In this model, there are three parameters denoted $\beta_1, \beta_2, \beta_3$, called "the clique parameters" [4], and associated to the horizontal, vertical, and transverse binary cliques respectively [3]. Given this *a priori* model, the prior distribution $P_X(x)$ can be written as :

$$P_X(x) = \exp\left(-\sum_{<s,t>} \beta_{st}(1 - \delta(x_s, x_t))\right)$$

where summation is taken over all pairs of spatial and inter-level neighboring sites and δ is the Kronecker delta function. In order to favor homogeneous regions with no privileged orientation in the Gibbs sampler simulation process, we choose $\beta_{st} = \beta_1 = \beta_2 = \beta_3 = 1$. Finally, $\Phi^{[p+1]}$ is computed from $\Phi^{[p]}$ in the following way :

- **Stochastic Step** : using the Gibbs sampler, one realization x is simulated according to the posterior distribution $P_{X/G}(x/g)$, with parameter vector $\Phi^{[p]}$.
- **Estimation Step** : the parameter vector $\Phi^{[p+1]}$ is estimated with the Maximum Likelihood (ML) estimator of the "complete data" corresponding to each class :
  - If $N_1 = \#\{s \in S : x_s = e_1\}$ is the number of pixels of the "CSF" area, the ML estimator $\hat{\Phi}_{(e_1)}$ of α is given by [3] : $\hat{\alpha}(x, g) = (1/N_1)\sum_{s \in S : x_s = e_1} g_s$.
  - If $N_2 = \#\{s \in S : x_s = e_2\}$ and $N_3 = \#\{s \in S : x_s = e_3\}$ pixels are located in the "white matter" and "grey matter" regions respectively, the corresponding ML estimator of each

[3] Cliques are subsets of sites which are mutual neighbors [4].

class is given by the empirical mean and the empirical variance. For instance, for the "white matter" class, we have for $\hat{\Phi}_{(e_2)}$:

$$\hat{\mu}(x,g) = \frac{1}{N_2} \sum_{s \in S: x_s = e_2} g_s \qquad \hat{\sigma}^2(x,g) = \frac{1}{(N_2 - 1)} \sum_{s \in S: x_s = e_2} (g_s - \hat{\mu})^2$$

- Repeat until convergence is achieved ; i.e., if $\hat{\Phi}^{[p+1]} \not\approx \hat{\Phi}^{[p]}$, we return to Stochastic Step.

Figure 5.2 represents the estimated distribution mixture of the SPECT volume shown in Figure 5.4. The three site-wise conditional data likelihoods $P_{G_s/X_s}(g_s/e_k)$, $k = 1, 2, 3$ (weighted by the estimated proportion π_k of each class) are superimposed to the image histogram. Corresponding estimates obtained by the estimation procedure (requiring about ten iterations) are given in Table 5.3.

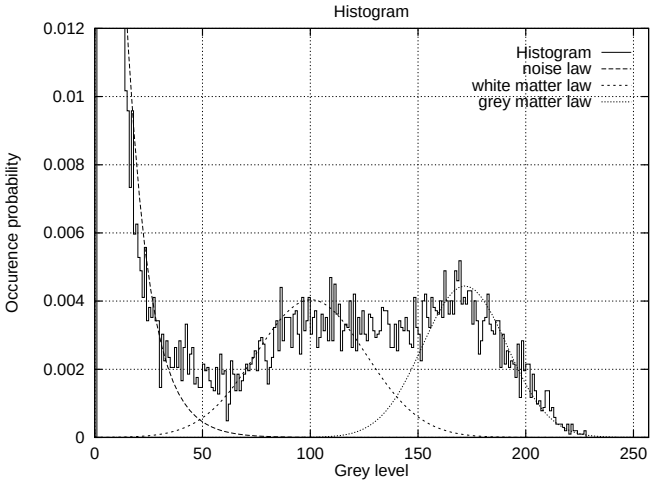

FIG. **5.2. Image histogram of the picture reported in Figure 5.4 (solid curve) and estimated probability density mixture obtained with the ICE procedure (dotted and dashed curves).**

	ICE Procedure		
$\Phi^{\text{final}}_{(e_1)}$	$0.52_{(\pi)}$	$11_{(\alpha)}$	
$\Phi^{\text{final}}_{(e_2)}$	$0.26_{(\pi)}$	$100_{(\mu)}$	$648_{(\sigma^2)}$
$\Phi^{\text{final}}_{(e_3)}$	$0.22_{(\pi)}$	$172_{(\mu)}$	$383_{(\sigma^2)}$

FIG. **5.3. Estimated parameters for the SPECT volume reported in Figure 5.4. π stands for the proportion of the three classes within the SPECT image. α are the exponential law parameter. μ and σ^2 are the Gaussian law parameters.**

Segmentation Step

Based on the estimates given by the ICE procedure, we can compute an unsupervised 3D Markovian segmentation of SPECT volumes. In this framework, the Markovian segmentation can be viewed as a statistical labeling problem according to a global Bayesian formulation in which the posterior distribution $P_{X/G}(x/g) \propto \exp -U(x,g)$ has to be maximized [4]. The corresponding posterior energy is given by :

$$U(x,g) = \underbrace{\sum_{s \in S} -\ln P_{G_s/X_s}(g_s/x_s)}_{U_1(x,g)} + \underbrace{\sum_{<s,t>} \beta_{st} \left(1 - \delta(x_s, x_t)\right)}_{U_2(x)}$$

where U_1 expresses the adequacy between observations and labels, and U_2 represents the energy of the *a priori* model. We use the deterministic Iterated Conditional Modes (ICM) algorithm [4] to minimize this global energy function. For the initialization of this algorithm, we exploit the segmentation map obtained by a ML segmentation. Figure 5.4 displays examples of unsupervised three-class segmentation, exploiting parameters estimated with the ICE procedure. In this segmentation, the "CSF", the "white matter" and the "grey matter" are represented by a dark, a grey, and a white region respectively, in order to visually express the activity level of the blood flow. The support $\mathcal{D}$ is then determined simply by the set of pixels belonging to the white and grey matter classes.

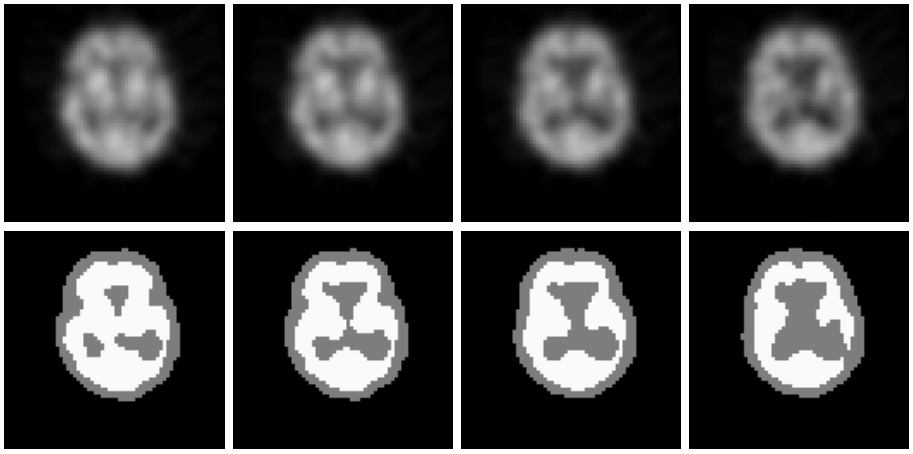

FIG. **5.4. Example of an unsupervised three-dimensional Markovian segmentation of a brain SPECT volume using the ICM deterministic relaxation technique and based on the parameters estimated by the ICE procedure. Top : real brain SPECT volume (four central transversal slices). Bottom : three-class Markovian segmentations.**

5.5 *Experimental results*

The effectiveness of this 3D blind deconvolution method was tested on several SPECT volumes composed of 64 transversal slices of 64×64 pixels with 256 grey levels. Those presented in this Section are only a few examples.

The initial inverse FIR filter required by the NAS-RIF algorithm is the Kronecker delta function [28] and the size of this inverse filter is $3 \times 3 \times 3$ pixels. Besides, we have used $\gamma = 0$ because the background of SPECT images is not completely black. We recall that the object support determination is based on the result of the 3D unsupervised Markovian segmentation (see Section 5.4). Finally, in order to objectively compare the resolution improvements between the original and deconvolved SPECT volumes, we have decided to stretch the histogram of the estimated 3D volume at convergence (i.e., $\hat{f}_{\text{final}}(x, y, z)$) in order to get the same mean value as the original input SPECT volume $g(x, y, z)$. The computational cost for a blind deconvolution cross-sectional image is about 50 seconds on a standard SunSparc 2 workstation (20 seconds for the support determination of the whole volume and 30 seconds for the blind deconvolution of each cross-sectional image).

Figures 5.5 and 5.6 present examples of brain SPECT volume deconvolutions obtained by this 3D blind deconvolution approach. The algorithm (requiring about 250 iterations) converges to a very good estimate of the solution without *a priori* information on the PSF and allows to noticeably improve the resolution of the original SPECT volume. For instance, this restoration procedure allows efficiently to detect small localized singularities associated with lesion or tumors that may not be clearly visible in the original blurred image. Figures 5.7c and 5.7d show the resolution improvement obtained by the 3D-extended version of the NAS-RIF algorithm over its 2D version for a given cross-sectional image (both methods are combined with the proposed unsupervised Markovian segmentation-based support-finding algorithm). The resolution improvement is visible (although difficult to appreciate due to the diffusive effect of the printer) and can be clearly noticed on a computer screen. Figure 5.8 shows examples of sagittal and coronal sections of the original and deconvolved human brain SPECT volumes whose cross-sectional slices have been presented in Figures 5.5 and 5.6. The improvement of the inter-slice resolution is also clearly visible.

The effectiveness of this deconvolution technique is also tested on a real SPECT phantom (i.e., a physical plexiglas head phantom filled with radioactive material and measured by a SPECT system) for which the ground truth of this segmented phantom is exactly known and thus for which the performance of our proposed method can then be objectively judged. Figure 5.9 presents examples of brain SPECT volume deconvolutions obtained by our 3D blind deconvolution approach on this SPECT phantom. We can easily notice that this SPECT volume is less noisy and less blurred than the real human brain SPECT volumes previously presented and processed (due to several factors such as a different dose of radioactive isotopes contained in each uniform region of this SPECT phantom, a longer acquisition time, the stillness of this simulated brain during the SPECT process, reduced attenuation, etc.) Nevertheless, once again, the resolution improvement remains visible.

In order to fully assess the success of this restoration procedure, we use the specific evaluation criteria proposed in [49], based on the estimation of the three following measures :

(i) Firstly, the average contrast of the image, defined by $C = (1 - m_2/m_3)$, where m_2 and m_3 are the mean of the pixel value in the "white matter" and "grey matter" area respectively.

(ii) Secondly, the image mottle M_2 in the "white matter" region, characterized by taking the ratio of the standard deviation σ_2 of pixel values in this area to the mean m_2.

(iii) Thirdly, the image mottle M_3 in the "grey matter" area.

These two last parameters allow to measure the amplification of the noise and/or measure the presence of undesirable artifacts that can be created by the deconvolution procedure in a uniform region of the real SPECT phantom (thus with ideally uniform radioactive activity). Due to the

difference of proportion of pixels belonging to each brain anatomical tissue, we consider the total mottle measure given by $M = \rho_2 M_2 + \rho_3 M_3$, with ρ_2 and ρ_3 designates the proportion of pixel belonging to the "white matter" and "gray matter" area respectively. A reliable SPECT image restoration technique will then allow to enhance the contrast of the image with little increase in mottle, i.e., without amplifying too much the noise and/or without creating false artificial features (technically, an increase by a factor of of 1.1–1.2 of the original mottle of the image remains acceptable if the contrast enhancement is significantly increased [49]). Due to the difference of thickness between the cross-sectional slices of the real and segmented phantom, these abovementioned measures are estimated on the whole 3D phantom after this one has been registered [14] on the ground truth of the segmented phantom volume (see Figure 5.10 where some consecutive slices of the segmented phantom are shown). Our proposed restoration technique allows a contrast enhancement from 9% to 21% between the original and deconvolved SPECT phantom along with an acceptable amplification of the mottle of this 3D image by a factor of 1.18 (from 17% to 20%). This represents a significant improvement in image quality with a very small penalty and attest the validity of our restoration method. Let us add that the registration process [14] induces most probably artificial features and our real restoration results are most likely better.

Finally, we have also tested our 3D deconvolution technique on some cross-sectional slices of a synthetic SPECT volume. In order to simulate at best the typical characteristics of real human brain SPECT images, we have re-created three homogeneous regions and added the corresponding noise for each ones, according to the grey level statistical distribution already estimated on a real human brain SPECT volume (see the distribution mixture presented in Figure 5.2 and parameters given in Figure 5.3). We have also added a 3D Gaussian blur in order to simulate the 3D scattering of the emitted photons. Figure 5.11 shows the ground truth of the segmented synthetic slices, the synthetic SPECT slices and finally the deconvolution results obtained by our restoration method. The resolution improvement is visible and the proposed procedure allow efficiently to recover high frequencies of the undistorted (non-convolved) image.

5.6 Conclusion

In this paper we have shown that a 3D extension of the NAS-RIF deconvolution procedure noticeably improves the resolution of human brain 3D SPECT images and can be a great help to facilitate their interpretation by the nuclear physician. We have also shown that this 3D blind deconvolution technique gives superior performance than its 2D version and can efficiently exploit the result of a 3D unsupervised Markovian segmentation in order to find the exact support of the object to be restored. This segmentation allows to accurately fit the finite-support constraint of this optimization strategy-based deconvolution technique. Finally, this 3D blind deconvolution technique combined with the unsupervised segmentation leads to a restoration procedure that is completely data driven and really compatible with an automatic processing of massive amounts of 3D SPECT data.

Acknowledgments

The author thanks **INRIA** (Institut National de la Recherche en Informatique et Automatique, France) for financial support of this work (postdoctoral grant). The authors are also grateful to Jean-Paul Soucy and Christian Janicki (CHUM, University of Montréal) for having provided the SPECT images.

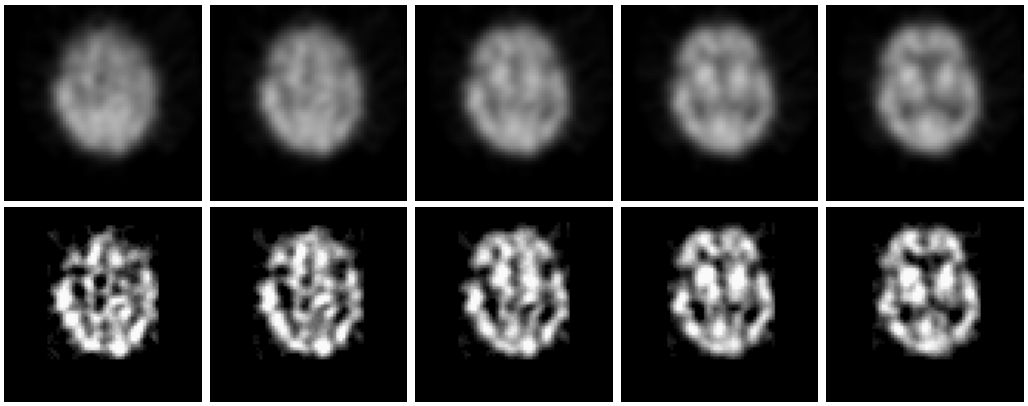

FIG. **5.5. Examples of human brain SPECT volume deconvolution given by the 3D-extended version of the NAS-RIF algorithm combined with the Markovian segmentation-based support finding algorithm. Top : five consecutive real cross-sectional SPECT slices. Bottom : deconvolution results.**

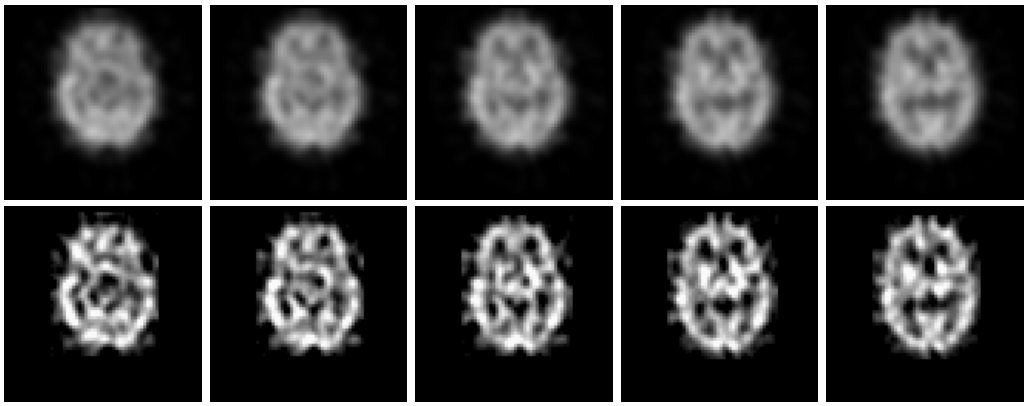

FIG. **5.6. Examples of human brain SPECT volume deconvolution given by the 3D-extended version of the NAS-RIF algorithm combined with the Markovian segmentation-based support finding algorithm. Top : five consecutive real cross-sectional SPECT slices. Bottom : deconvolution results.**

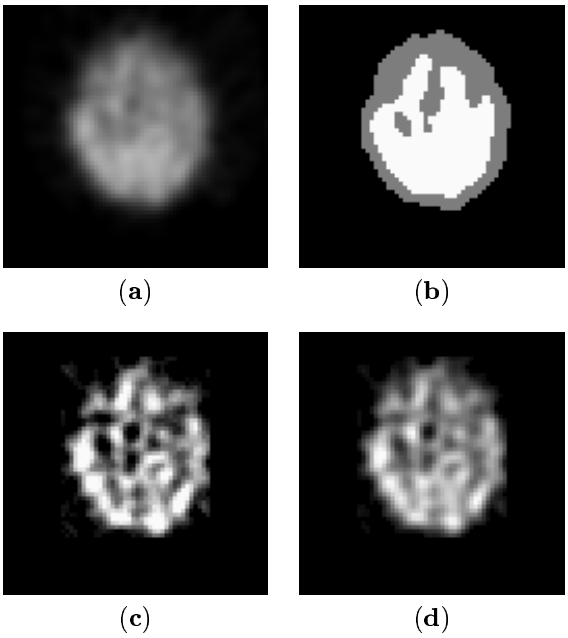

FIG. **5.7. Examples of human brain SPECT cross-sectional image segmentation and deconvolutions. (a) : Original SPECT cross-sectional human brain image. (b) : Unsupervised three-dimensional Markovian segmentation. (c) : Deconvolution result given by the 3D-extended version of the NAS-RIF algorithm (inverse filter size is $3\times3\times3$). (d) : Deconvolution result given by its 2D version (inverse filter size is 5×5) (both deconvolution methods require the same computational load and are combined with the proposed Markovian segmentation-based support-finding algorithm (Figure b)).**

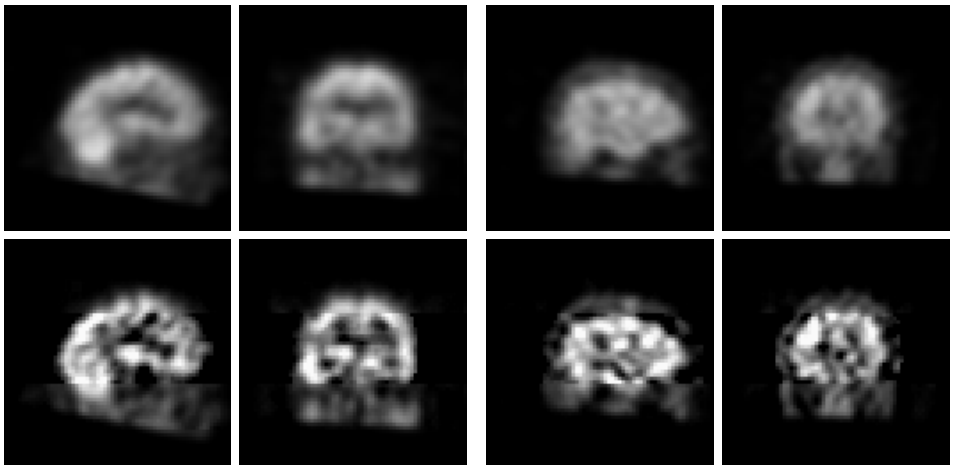

FIG. 5.8. **Examples of sagittal (a)(c) and coronal (b)(d) sections of the original (top) and deconvolved (bottom) human brain SPECT volumes whose cross-sectional slices have been presented in Figure 5.5 for (a)(b) and in Figure 5.6 for (c)(d).**

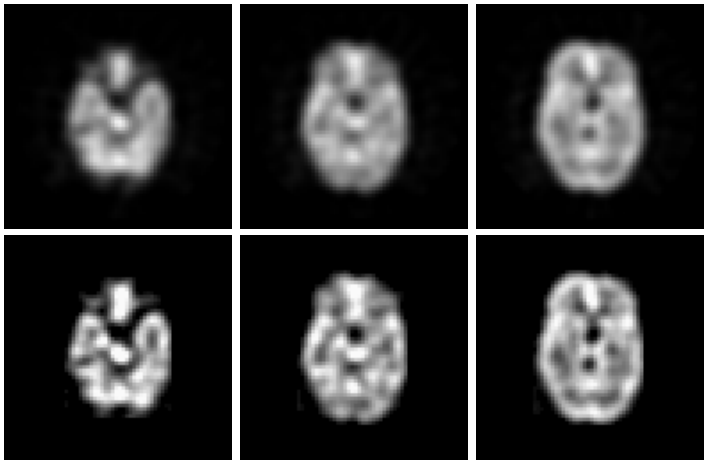

FIG. 5.9. **Examples of deconvolution obtained by our 3D blind deconvolution approach on some cross-sectional slices of a SPECT phantom. Top : real cross-sectional SPECT phantom slices. Bottom : deconvolution results.**

FIG. 5.10. **Examples of some consecutive cross-sectional slices of the segmented phantom (ground truth).**

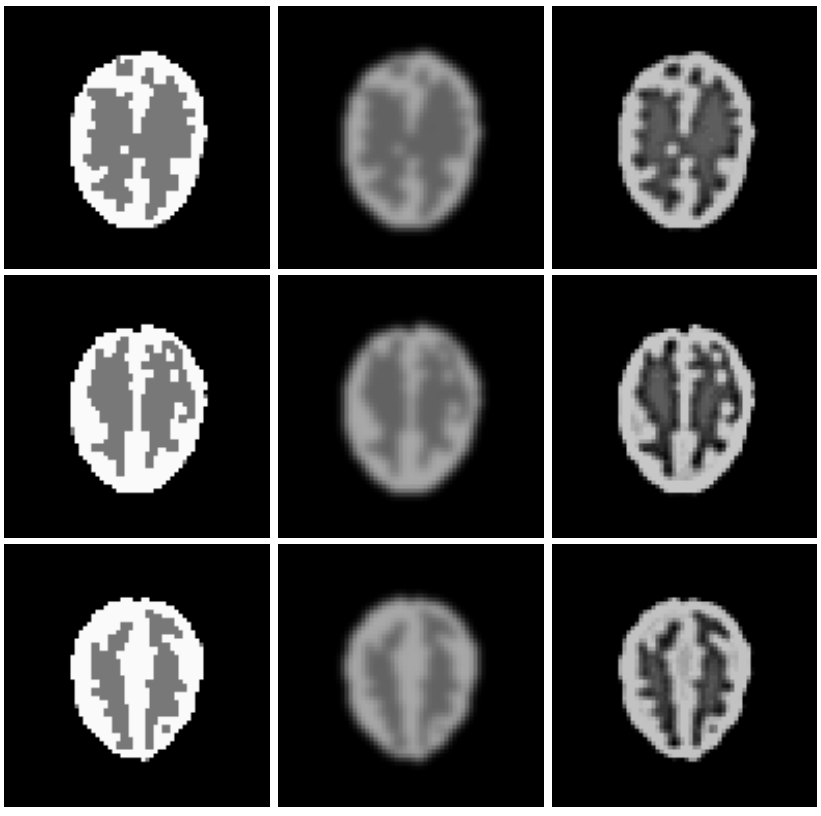

(a) (b) (c)

FIG. 5.11. **Example of deconvolution results on some cross-sectional slices of a synthetic SPECT volume. (a) Ground truth of the segmented synthetic slices. (b) synthetic SPECT slices. (c) Deconvolution results.**

REFERENCES

[1] A. Amini, T. Weymouth, and R. Jain. Using Dynamic Programming for solving variational problems in vision. *IEEE Trans. on PAMI*, 12(9) :855–867, 1990.

[2] G.R. Ayers and J.C. Dainty. Iterative blind deconvolution method and its application. *Optics Letters*, 13(7) :547–549, 1988.

[3] S. Banks. *Signal processing, image processing and pattern recognition.* Prentice Hall, 1990.

[4] J. Besag. On the statistical analysis of dirty pictures. *Journal of the Royal Statistical Society*, B-48 :259–302, 1986.

[5] D.S.C. Biggs and M. Andrews. Asymmetric iterative blind deconvolution of multiframe images. In *Proceedings of SPIE*, volume 3461-33, 1998.

[6] D. Boulfelfel, R.M. Rangayyan, L.J. Han, and R. Kloiber. Prereconstruction restoration of myocardial single photon emission computed tomography images. *IEEE Trans. on Medical Imaging*, 11(3) :336–341, 1992.

[7] B. Braathen, P. Masson, and W. Pieczynski. Global and local methods of unsupervised Bayesian segmentation of images. *GRAPHICS and VISION*, (1) :39–52, 1993.

[8] P.H. Van Cittert. *Z. Physik*, 69 :298, 1931.

[9] T.F. Cootes, C.J. Taylor, D.H. Cooper, and J. Graham. Active shape models -their training and application. *CVGIP : Inage Understanding*, 61 :38–59, 1994.

[10] D.C. Costa and P.J. Ell. *Brain Blood Flow in Neurology and Psychiatry.* Series Editor : P.J. Ell, 1991.

[11] T.S. Curry, J.E. Dowdey, and R.C. Murry. *Christensen's Physics of Diagnostic Radiology.* Lea and Febiger, 1990.

[12] A.P. Dempster, N.M. Laird, and D.B. Rubin. Maximum likelihood from incomplete data via the EM algorithm. *Royal Statistical Society*, pages 1–38, 1976.

[13] S.D. Fenster and J.R. Kender. Sectored snakes : evaluating learned-energy segmentations. In *Proc. International Conference on Computer Vision*, pages 420–426, Jan. 1998.

[14] K.J. Friston, J. Ashburner, C.D. Frith, J.B. Poline, J.D. Heather, and R.S.J. Frackowiak. Spatial registration and normalization of images. *Human Brain Mapping*, 3(3) :165–189, 1995.

[15] D. Geiger, A. Gupta, L.A. Costa, and J. Vlontzos. Dynamic Programming for detecting, tracking and matching deformable contours. *IEEE Trans. on PAMI*, 17(3) :294–302, 1995.

[16] S. Geman and D. Geman. Stochastic relaxation, Gibbs distributions and the Bayesian restoration of images. *IEEE Trans. on Pattern Analysis and Machine Intelligence*, 6(6) :721–741, 1984.

[17] D.E Goldberg. *Genetic Algorithm.* Addison Wesley, 1989.

[18] J. W. Goodman. Some fundamental properties of speckle. *Journal of Optical Society of America*, 66(11) :1145–1150, 1976.

[19] U. Grenander and M. Keenan. Towards automated image understanding. *Advances in Applied Statistics*, 16 :89–103, 1993.

[20] F. Heitz, P. Pérez, and P. Bouthemy. Multiscale minimisation of global energy functions in some visual recovery problems. *CVGIP : Image Understanding*, 59(1) :125–134, 1994.

[21] B.R. Hunt and P.J. Sementilli. Description of a poisson imagery super-resolution algorithm. *Astronomical Data Analysis Software and Systems I*, 52 :196–199, 1992.

[22] A.K. Jain, Y. Zhong, and S. Lakshmanan. Object matching using deformable templates. *IEEE Trans. on Pattern Analysis and Machine Intelligence*, 18(3) :267–278, 1996.

[23] M.P. Dubuisson Jolly, S. Lakshmanan, and A.K Jain. Vehicle segmentation and classification using deformable templates. *IEEE Trans. on Pattern Analysis and Machine Intelligence*, 18(3) :293–308, 1996.

[24] M. Kass, A. Witkin, and D. Terzopoulos. Snakes : active contour models. *IJCV*, 1(4) :321–331, 1988.

[25] A.K. Katsaggelos, J. Biemond, R.W. Shafer, and R.M. Mersereau. A regularized iterative image restoration algorithm. *IEEE trans. on Acoustic Speech and Signal Processing*, 39 :914–929, 1991.

[26] C. Kervrann and F. Heitz. Statistical model-based segmentation of deformable motion. In *Proc. International Conference on Image Processing*, pages 937–940, Lausanne, 1996.

[27] K. Kluge and S. Lakshmanan. Lane boundary detection using deformable templates : effects of image subsampling on detected lane edges. In *Proc. Asian Conference on Computer Vision*, pages 141–145, Singapore, Dec. 1995.

[28] D. Kundur and D. Hatzinakos. Blind image restoration via recursive filtering using deterministic constraints. In *Proc. International Conference on Acoustics, Speech, and Signal Processing*, volume 4, pages 547–549, 1996.

[29] S. Lakshmanan and D. Grimmer. A deformable template approach to detecting straight edges in radar images. *IEEE Trans. on Pattern Analysis and Machine Intelligence*, 18(4) :438–443, 1996.

[30] L. Landweber. *American Journal of Mathematic*, 73 :615, 1951.

[31] L.B. Lucy. An iterative technique for the rectification of observed images. *The Astronomical Journal*, 79(6) :8–37, 1974.

[32] M.T. Madsen and C.H. Park. Enhancement of SPECT images by Fourier filtering the projection set. *Journal of Nuclear Science*, 26 :2687–2690, 1979.

[33] P. Masson and W. Pieczynski. SEM algorithm and unsupervised statistical segmentation of satellite images. *IEEE Trans. on Geoscience and Remote Sensing*, 31(3) :618–633, 1993.

[34] M. Mignotte, C. Collet, P. Pérez, and P. Bouthemy. Unsupervised hierarchical Markovian segmentation of sonar images. In *Proc. International Conference on Image Processing*, Santa Barbara, Californie, USA, Oct. 1997.

[35] M. Mignotte, C. Collet, P. Pérez, and P. Bouthemy. Unsupervised Markovian segmentation of sonar images. In *Proc. International Conference on Acoustics, Speech, and Signal Processing*, volume 4, pages 2781–2785, Munchen, May 1997.

[36] M. Mignotte, C. Collet, P. Pérez, and P. Bouthemy. Unsupervised segmentation applied on sonar images. In *Proc. International Workshop EMMCVPR'97 : Energy Minimisation Methods in Computer Vision and Pattern Recognition*, volume LNCS 1223, pages 491–506, Venice, Italy, May 1997. Springer-verlag.

[37] M. Mignotte, C. Collet, P. Pérez, and P. Bouthemy. Statistical model and genetic optimization : application to pattern detection in sonar images. In *Proc. International Conference on Acoustics, Speech, and Signal Processing*, Seattle, April 1998.

[38] M. Mignotte and J. Meunier. A comparison of supervised and blind deconvolution techniques applied in SPECT imagery. *Physics in Medecine and Biology, submitted.*

[39] M. Mignotte and J. Meunier. Deformable template and distribution mixture-based data modeling for the endocardial contour tracking in an echographic sequence. In *Proc. CVPR*, volume 1, pages 225–230, Fort Collins, Colorado, June 1999.

[40] M. Mignotte and J. Meunier. Deformable template and distribution mixture-based data modeling for the endocardial contour tracking in an echographic sequence. In *Conf. Computer Vision and Pattern Recognition*, Colorado (acepted), Juin 1999.

[41] R. Molina, J. Mateos, and J. Abad. Prior models and the Richardson-Lucy restoration method. *The Restoration of HST Images and Spectra II*, 52 :118, 1994.

[42] Y. Nakazawa, T. Komatsu, and T. Saito. A robust object-specified active contour model for tracking smoothly deformable line-features and its application to outdoor moving image processing. In *Proc. International Conference on Image Processing*, pages 689–692, Lausanne, Sept. 1996.

[43] W. Pieczynski. Champs de Markov cachés et estimation conditionnelle itérative. *Revue Traitement Du Signal*, 11(2) :141–153, 1994.

[44] S. J. Reeves and M. Mersereau. Automatic assessment of constraint sets in image restoration. *IEEE Trans. on Image Processing*, 1(1) :119–123, 1992.

[45] D. Rueckert and P. Burger. Geometrically deformed templates for shape-based segmentation and tracking in cardiac MR images. In *Proc. International Workshop EMMCVPR'97 : Energy Minimisation Methods in Computer Vision and Pattern Recognition*, volume LNCS 1223, pages 83–98, Venice, Italy, May 1997. Springer-verlag.

[46] F. Salzenstein and W. Pieczinsky. Unsupervised Bayesian segmentation using hidden markovian fields. *In proc. International Conference on Acoustics, Speech, and Signal Processing*, pages 2411–2414, May 1995.

[47] F. Schmitt, M. Mignotte, C. Collet, and P. Thourel. Estimation of noise parameters on sonar images. In *Signal and Image Processing*, volume SPIE 2823, pages 1–12, Denver, Colorado, USA, Aug. 1996.

[48] Geir Storvik. A Bayesian approach to dynamic contours through stochastic sampling and Simulated Annealing. *IEEE Trans. on PAMI*, 16(10) :976–986, 1994.

[49] S. Webb, A.P. Long, R.J. Ott, M.O. Leach, and M.A. Flower. Constrained deconvolution of SPECT liver tomograms by direct digital image restoration. *Med. Phys.*, 12(1) :53–58, 1985.

[50] D.J. Williams and M. Shah. A fast algorithm for active contours and curvature estimation. *CVGIP : Image understanding*, 55(1) :14–26, 1992.

[51] Y.L. You and M. Kaveh. A regularization approach to joint blur identification and image restoration. *IEEE trans. on Image Processing*, 5(3) :416–428, 1996.

[52] Y. Zhang, A.K. Jain, and M.P. Dubuisson-Jolly. Object tracking using deformable templates. In *Proc. International Conference on Computer Vision*, pages 440–45, Jan. 1998.

PUBLICATIONS RELATED TO THIS WORK

REVIEWS

[R1] M. Mignotte, J. Meunier. "Shape-based Segmentation and tracking of anatomical structures using Deformable templates and a noise model estimation in an echographic sequence". *IEEE Trans. on Medical Imaging*, second revision.

[R2] M. Mignotte, J. Meunier. "Three-dimensional blind deconvolution of SPECT images". *IEEE Trans. on Biomedical Engineering*, accepted, 99.

CONFERENCES

[C1] M. Mignotte, J. Meunier. "Deformable template and distribution mixture-based data modeling for the endocardial contour tracking in an echographic sequence". In : Conf. *Computer Vision and Pattern Recognition*, volume 1, page 225-230, Fort Collins, Colorado, June 99.

[C2] M. Mignotte, J. Meunier. "Blind deconvolution of SPECT images using a noise model estimation". In : *Proceedings SPIE Conference on Medical Imaging*, San Diego, California, USA, Feb. 00, submitted.

[C3] M. Mignotte, J. Meunier. "An unsupervised multiscale approach for the dynamic contour-based boundary detection issue in ultrasound imagery". In : Conf *Computer Vision, Pattern Recognition and Image Processing*, Atlantic city, USA, March 00, submitted.

ABOUT THE AUTHOR

Max Mignotte received the DEA (Postgraduate degree) in Digital Signal, Image and Speech processing from the INPG University, France (Grenoble), in 1993 and the Ph.D. degree in electronics and computer engineering from the University of Bretagne Occidentale (UBO) and the digital signal laboratory (GTS) of the French Naval academy, France, in 1998. He was an INRIA post-doctoral fellow at University of Montreal (DIRO), Canada (Québec), from 1998 to 1999. His current research interests include statistical methods and Bayesian inference for image segmentation (with hierarchical Markovian, statistical templates or active contour models), parameters estimation, tracking, classification, deconvolution and restoration issues in medical or sonar imagery.

Professional address :
Dr. Max Mignotte
DIRO, C.P. 6128, Succ. Centre-ville,
2920 Chemin de la Tour, H3C 3J7 Montreal (Quebec),
Phone : (514) 343-6111 (ext. 1657)
Phone : (514) 343-7107
Fax : (514) 343-5834
mail : mignotte@iro.umontreal.ca

Personal address :
38 avenue de Limburg, 69110 Sainte-Foy les lyon, FRANCE.
Phone : (33) 04 78 59 60 16
mail : mignotte@wanadoo.fr

Weib page on my postdoctoral work :
http ://www.iro.umontreal.ca/∼mignotte/

Max Mignotte

Septembre 1999